Underwater Acoustic Field Extrapolation: Theory and Sensitivity Analysis

by Warren L. J. Fox

DTIC
SELECTED
JUN 1 4 1995
F

DTIC QUALITY INSPECTED 3
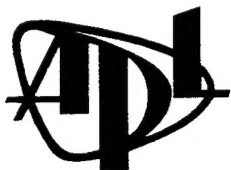
19950612 149

Underwater Acoustic Field Extrapolation: Theory and Sensitivity Analysis

by Warren L. J. Fox

Accesion For		
NTIS CRA&I	☑	
DTIC TAB	☐	
Unannounced	☐	
Justification		
By		
Distribution /		
Availability Codes		
Dist	Avail and / or Special	
A-1		

FOREWORD

ABSTRACT

In some underwater acoustic applications, it is desirable to predict what an acoustic field will be at some distance away from a source. Numerical modeling based on environmental parameters (e.g., sound speed, bathymetry, sediment properties) is one possibility, but the amount of environmental information necessary for accurate long-range modeling is often beyond what is realistically measurable. Actual acoustic measurements are another possibility, but our knowledge of the fields is then limited to the points in the ocean where the sources and receivers are located. We present a hybrid method for predicting acoustic fields that takes limited acoustic measurements and extrapolates them over short ranges using modeled fields. The measured and modeled fields are combined in an integral formulation via a specialization of Huygens' principle. The basic theoretical formulation is stated and analyzed using the theory of normal modes. The formulation leads directly to modal-dependent (grazing angle dependent) "obliquity" factors, which are canceled to first order by averaging with a range derivative-based extrapolation. Sensitivity of the algorithm to the higher order components of the obliquity factors is studied. As with other model-based algorithms, environmental mismatch can degrade the results. The algorithm's sensitivity to mismatch in water column sound speed and sediment sound speed, attenuation, and density are studied via a perturbational approach. Since the algorithm explicitly contains an integral and the measured field is collected at discrete locations, numerical quadrature techniques are studied. It is shown how undersampling can degrade the quality of the extrapolated fields, and how the spatial sampling required for reliable extrapolation can be obtained. A modal decomposition-based integration method is then shown, where the number of reference elements required is equal to the number of modes that contribute significantly to the fields. A modified version of this formulation can exactly cancel the obliquity factors.

Table of Contents

List of Figures

List of Tables

Acknowledgments

Dedicated to

the memory of

R. J. Weiss

Chapter 1: Introduction

1.1. Introduction to the Dissertation and to Chapter 1

It is well known that electromagnetic waves do not propagate well through the ocean due to the strong attenuating effects of seawater on this kind of energy. On the other hand, under the proper conditions, acoustic waves can effectively propagate over extremely long distances (on the order of thousands of kilometers). Even over relatively short ranges, the use of acoustic energy is preferred for a variety of underwater applications such as communications, active/passive target detection and localization, imaging of submerged objects, etc.

In some underwater acoustic applications, it is necessary to predict what an acoustic field will be at some point distant from an acoustic source. This is usually accomplished by first sampling the environmental properties of the ocean that affect the propagation between the source and the distant point. Examples of these properties include (but are not limited to) the sound speed in the water column, the bathymetry in the region of interest, and the sound speed, density, and attenuation in the ocean bottom. For very simple situations, analytic solutions of the acoustic field are possible. For most scenarios the sampled environmental properties are used as input to one of several types of numerically-based methods for modeling underwater acoustic fields. Two such methods currently implemented in computer software are parabolic equation (PE) approximations [Collins and Westwood, Collins] and normal mode-based solutions [Porter and Reiss, Porter (1992)].

In practice, however, the amount of environmental information required for accurate predictions of the acoustic field over any significant range may be beyond what is realistically measurable. For example, the bathymetry and the sound speed profile in the water column may vary too rapidly with range and/or time to allow adequate sampling.

Ocean bottom parameters (which are typically difficult to measure in any case) may also vary unpredictably with range. Surface and bottom roughness can also contribute to modeling difficulties.

Another possible method for determining acoustic fields distant from a source is to actually measure them using hydrophone arrays. Although this method would provide exact results for any kind of environmental situation, its use is limited by the fact that the fields would only be known for the given source and receiver locations.

This dissertation will describe and analyze a hybrid method for predicting underwater acoustic fields that utilizes both limited acoustic measurements and modeled fields (over relatively short ranges) that are based on local environmental information. The two types of information are gathered along arrays of transmitters and/or receivers deployed vertically in the ocean, and are "combined" using a specialization of Huygens' principle. The measured acoustic data can be thought of as "calibrating" a region of ocean. The modeled fields are then used to "extrapolate" the measurements.

The remainder of Chapter 1 will contain an introduction to normal mode theory, which is used extensively throughout the remainder of this work. It will also review some previous work on a holographic array processing (HAP) algorithm for source localization whose mathematical underpinnings are related to those of the acoustic field extrapolation algorithm. A preview to the remainder of the dissertation will follow.

1.2. Normal Mode Theory

This section is intended as a brief introduction to normal mode theory for underwater acoustic propagation. While some of the "highlights" of the mathematical derivations will be presented, mathematical rigor will be eschewed in favor of physical interpretations of the resulting equations. This material will follow the treatment found in [Jensen *et al.*], although other excellent rigorous mathematical derivations can be found in

[Boyles] and [Brekhovskikh and Lysanov].

1.2.1. Range-independent Normal Modes

The inhomogeneous acoustic wave equation for pressure can be derived from basic physical laws [Jensen *et al.*] and stated as

$$\rho \nabla \bullet \left(\frac{1}{\rho} \nabla p \right) - \frac{1}{c^2} \frac{\partial^2 p}{\partial t^2} = f(\mathbf{r}, t), \tag{1.1}$$

where ρ is density, c is the speed of sound, p is pressure, and $f(\mathbf{r}, t)$ is the source term as a function of space and time. Several assumptions are now made. First we assume that we will be dealing with narrow-band sources of the type $e^{-i\omega t}$. This justifies Fourier transforming the wave equation into the frequency domain and, therefore, obtaining a time-independent solution. Secondly, we assume a cylindrically symmetric medium about the source, and, therefore, will use a cylindrical coordinate system. Lastly, we assume that ρ and c depend only on depth, i.e., the medium is range-independent. Taking these assumptions into account, we can write the so-called Helmholtz equation as

$$\frac{1}{r} \frac{\partial}{\partial r} \left[r \frac{\partial p(r, z)}{\partial r} \right] + \rho(z) \frac{\partial}{\partial z} \left[\frac{1}{\rho(z)} \frac{\partial p(r, z)}{\partial z} \right] + \frac{\omega^2}{c^2(z)} p(r, z) = -\frac{\delta(r)\delta(z - z_s)}{2\pi r}, \tag{1.2}$$

where r is the range coordinate, z is the depth coordinate, z_s is the source depth, and ω is the radian frequency of the source.

In order to solve Eq. 1.2, we use the technique of separation of variables [Boyles]. This technique assumes a solution that is a product of range-only-dependent and depth-only-dependent factors, i.e.,

$$p(r, z) = \phi(r)\psi(z). \tag{1.3}$$

By substituting this into the homogeneous Helmholtz equation, the so-called modal equation can be written as

$$\rho(z)\frac{d}{dz}\left[\frac{1}{\rho(z)}\frac{d\psi_m(z)}{dz}\right] + \left[\frac{\omega^2}{c^2(z)} - \xi_m^2\right]\psi_m(z) = 0 \qquad (1.4)$$

with boundary conditions

$$\psi_m(0) = 0 \qquad \text{and} \qquad \frac{d\psi_m(z)}{dz}\bigg|_{z=D} = 0; \qquad (1.5)$$

ξ_m^2 is called the separation constant.

The boundary condition at the surface ($z = 0$) implies what is known as a free or pressure release surface. It is also known as the Dirichlet boundary condition. It is characterized by the fact that acoustic pressure vanishes along such a surface. The lower boundary condition (at depth $z = D$) implies what is known as a rigid surface. It is also known as the Neumann boundary condition. It is characterized by the fact that the derivative of acoustic pressure (or, equivalently, particle velocity) vanishes along this type of surface. It should be noted that while the ocean surface can behave much like a Dirichlet boundary under calm conditions, the Neumann boundary condition is often a poor approximation of the ocean bottom. The Neumann condition is still used as a mathematical nicety for analytical work, however, and more realistic bottom models can easily be incorporated into numerical modeling algorithms.

The modal equation is now in the form of a proper Sturm-Liouville eigenvalue problem [Boyles]. Several properties [Jensen *et al.*] of this type of problem will aid in our understanding of material to come:

(1) the modal equation has an infinite number of solutions, similar in nature to the modes of a vibrating string,

(2) each mode is characterized by an eigenfunction, or mode shape function, $\psi_m(z)$ (where the mth mode function has m zeroes), and an eigenvalue, or what can be interpreted as a horizontal propagation constant or horizontal wavenumber, ξ_m,

(3) the eigenvalues are all distinct, are ordered such that $\xi_1 > \xi_2 > \dots$, and it can be shown that all the eigenvalues are less than ω / c_{min} where c_{min} is the lowest sound speed of the problem [Jensen *et al.*],

(4) the eigenfunctions form an orthonormal set relative to $\rho(z)$, i.e.,

$$\int_0^D \frac{\psi_m(z)\psi_n(z)}{\rho(z)} dz \equiv \{ \begin{matrix} 1, m = n \\ 0, m \neq n \end{matrix} , \tag{1.6}$$

and hence the terminology "normal modes,"

(5) the eigenfunctions form a complete set, so that the pressure can be expressed as a sum of normal modes:

$$p(r, z) = \sum_{m=1}^{\infty} \phi_m(r)\psi_m(z). \tag{1.7}$$

After some mathematical manipulation, and using the above properties, it can be shown that [Jensen *et al.*]

$$\phi_m(r) = \frac{i}{4\rho(z_s)}\psi_m(z_s)H_0^{(1)}(\xi_m r), \tag{1.8}$$

where $H_0^{(1)}(x)$ is the zero-order Hankel function of the first kind. Using the asymptotic (large argument, $x \gg 1$) approximation of the Hankel function, i.e.,

$$H_0^{(1)}(x) \approx \left[\frac{2}{\pi x}\right]^{1/2} e^{i\left(x - \frac{\pi}{4}\right)} = \left[\frac{2}{\pi x i}\right]^{1/2} e^{ix}, \tag{1.9}$$

we can finally express the pressure as

$$p(r, z) \cong \left[\frac{i}{8\pi r}\right]^{1/2} \frac{1}{\rho(z_s)} \sum_{m=1}^{\infty} \psi_m(z_s)\psi_m(z)\xi_m^{-1/2}e^{i\xi_m r}. \qquad (1.10)$$

Note that this equation can be simply thought of as a linear combination of the mode functions, i.e.,

$$p(r, z) \cong \sum_{m=1}^{\infty} W_m \psi_m(z), \qquad (1.11)$$

where the W_m's are complex-valued weights that are functions of the horizontal wavenumbers and of the mode functions at the transmit depth, density, and range.

In accordance with property (2) above, each mode can be thought of as having a wavenumber

$$k_m = \xi_m \hat{r} + \eta_m \hat{z}, \qquad (1.12)$$

where $|k_m| = k_{ref}$ for all m, ξ_m and η_m can be considered horizontal and vertical wavenumbers respectively, and $\hat{r}$ and $\hat{z}$ are unit vectors in range and depth respectively. Each mode can be thought of as describing energy that propagates at an approximate grazing angle (i.e., with respect to the horizontal)

$$\chi_m \sim \mathrm{acos}\left[\frac{\xi_m}{k_{ref}}\right], \qquad (1.13)$$

where $k_{ref} = \omega/c_{ref}$ is a reference wavenumber. For this interpretation to make physical sense, c_{ref} should be equal to c_{min} in accordance with property (3) given above. Also in accordance with property (3) is the fact that higher order modes propagate at increasingly

steeper grazing angles.

1.2.2. Weakly Range-Dependent (Adiabatic) Normal Modes

The previous section dealt with a range-independent medium. When the medium varies with range, a phenomenon called mode coupling occurs. This means that as the acoustic energy propagates in range, energy from one mode can be transferred into another mode. Variations in sound speed profiles with range, sloping bottoms, internal waves, surface and bottom roughness, and other factors can all contribute to mode coupling.

The degree of mode coupling between modes m and n at a given range r is governed by the relations (Jensen *et al.*)

$$A_{mn} = \int \frac{1}{r}\frac{\partial}{\partial r}\left[r\frac{\partial \psi_m}{\partial r}\right]\frac{\psi_n}{\rho}dz$$

$$B_{mn} = \int \frac{\partial \psi_m}{\partial r}\frac{\psi_n}{\rho}dz.$$

$$(1.14)$$

The so-called adiabatic approximation assumes that these quantities are negligible and the pressure is written

$$p(r, z) \cong \left[\frac{i}{8\pi r}\right]^{1/2}\frac{1}{\rho(z_s)}\sum_{m=1}^{\infty}\psi_m(0, z_s)\psi_m(r, z)\xi_m(r)^{-1/2}e^{i\int_0^r \xi_m(r')dr'}.$$

$$(1.15)$$

The mode functions and horizontal wavenumbers at any given range are determined by using the reference waveguide method [Brekhovskikh and Lysanov]. This method consists of taking the sound speed and density profiles and the depth at the given range and constructing a hypothetical range-independent waveguide. The method of the previous section is then used to solve for the modes and horizontal wavenumbers for that range.

Note again that the pressure can be expressed as a linear sum of complex-weighted mode functions for any given receive range.

It can be seen that there is not a great deal of difference between Eq. 1.15 and its range-independent counterpart Eq. 1.10. One difference is the accumulated phase in the exponential. The integrated phase in Eq. 1.15 averages over range the contribution of the range-dependent horizontal wavenumbers to the total phase. Another difference is the range dependence of the other arguments in the summand. Note that Eq. 1.15 reverts to Eq. 1.10 for range-independent mode functions and horizontal wavenumbers.

1.2.3. Stepwise Coupled Modes

A coupled mode solution for a stepwise range-dependent environment as pictured in Fig. 1.1 can be given as [Evans]

$$p_j(r, z) = \sum_m [A_{j, m} H1_{j, m}(r) + B_{j, m} H2_{j, m}(r)] \, \psi_{j, m}(z), \qquad (1.16)$$

where j denotes the range segment ($j = 1$ is to the left of r_1), m is the mode index, the A's and B's are complicated expressions dependent on the source condition and mode
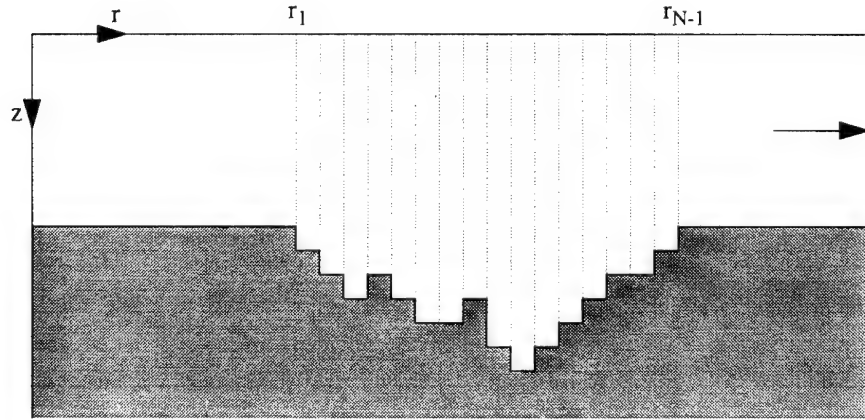
Figure 1.1. Schematic for stepwise coupled modes.

coupling matrices, and the *H1*'s and *H2*'s are ratios of Hankel functions given by

$$H1_{j,m}(r) = \frac{H_0^{(1)}(\xi_{j,m}r)}{H_0^{(1)}(\xi_{j,m}r_{j-1})} \quad , \quad H2_{j,m}(r) = \frac{H_0^{(2)}(\xi_{j,m}r)}{H_0^{(2)}(\xi_{j,m}r_{j-1})}. \tag{1.17}$$

$r_{j-1} = r_1$ for $j = 1$ is a special case. Refer to [Evans] for a more detailed explanation. Again, note that for any given range segment the pressure is a linear combination of the reference waveguide mode functions for that range.

1.3. Holographic Array Processing for Source Localization

An important research topic in recent years has been the underwater source localization problem, i.e., given a remote measurement of an acoustic signal generated by an unknown source, how can one determine the location of the source? A set of algorithms falling under the general heading of "matched-field processing" has arisen in an effort to solve this problem. The algorithms essentially consist of comparing a measured acoustic field P due to the source with simulated replica fields P_r that are numerically calculated based on available environmental information. The replica fields are calculated for a grid of hypothetical source locations, and the P_r that most closely "matches" the measured field P indicates the location of the source.

Consider a vertical receiving array at range $r = 0$ with receivers at a set of depths z_n. For a source at range r_s and depth z_s emitting a time-harmonic $e^{-i\omega t}$ signal, the measured complex pressure at receiver n is denoted $P(r_s, z_s, z_n)$. Likewise, the replica field for a hypothetical source position (r_s', z_s') is denoted $P_r(r_s', z_s', z_n)$. For a grid of hypothetical source locations, an "ambiguity function" can be computed as [Hamson and Heitmeyer]

$$A(r_s, z_s, r_s', z_s') = \frac{\left| \sum_n P(r_s, z_s, z_n) P_r^*(r_s', z_s', z_n) \right|^2}{\sum_n |P|^2 \sum_n |P_r|^2}, \tag{1.18}$$

where the * represents complex conjugate. The ambiguity function will be one for the correctly located source position, and less than one for incorrect source locations. This assumes, of course, that the modeled field corresponding to the correct source location is a perfect representation of the true field. Other algorithms [Baggeroer *et al.*] incorporate the cross-spectral matrix for the array into the algorithm, but Eq. 1.18 will suffice for material presented here.

Calculation of the replica fields $P_r(r_s', z_s', z_n)$ is often the most troublesome aspect of matched-field source localization algorithms for reasons stated in Sec. 1.1. Several studies have shown how insufficient and/or incorrect knowledge of the parameters that affect the propagation and that are used as input to the numerical codes can degrade the performance of matched-field processors (see references given in [Baggeroer *et al.*]). Typically, as the range over which one needs to model the propagation grows, so does the error that is introduced into the calculated replica fields. This is because more environmental variability is introduced into the problem as range increases, meaning that more environmental variability must be taken into account by the modeling algorithm.

It was observed [Rouseff (1989)] that one could use variable depth reference sources in the vicinity of the unknown source to partially compensate for the propagation path between the unknown source and a receiving array. Figure 1.2 shows the general geometry of the problem. This idea was then formalized [Mourad *et al.*, Porter *et al.* (1992)] into a source localization algorithm. Using adiabatic normal mode theory and the notation of [Mourad *et al.*], we can write the pressure field incident on the receiving array due to the unknown source as
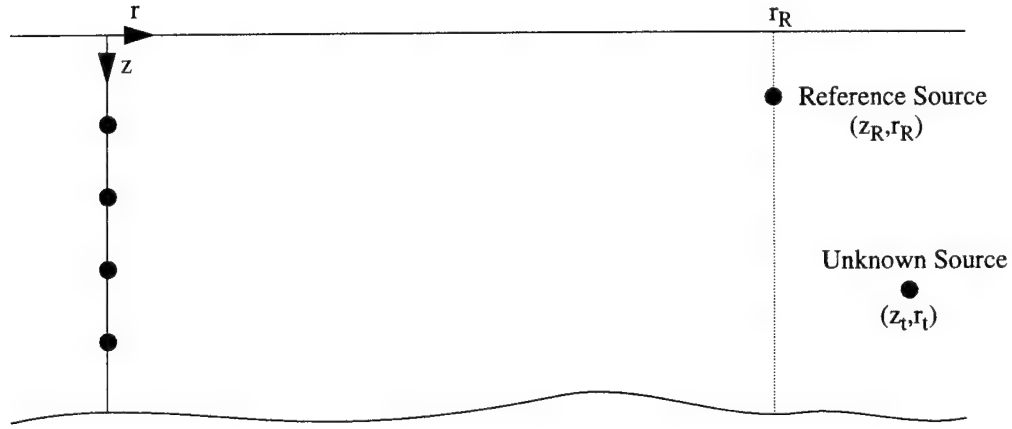
Figure 1.2. Geometry for source localization.

$$P_t(z_i, 0) \approx \left[\frac{2\pi i}{r_t}\right]^{1/2} \sum_j \psi_j(z_i, 0)\, \psi_j(z_t, r_t)\, [\xi_j(r_t)]^{-1/2} e^{-i\int_0^{r_t}\xi_j(r)\,dr} \qquad (1.19)$$

and that due to the reference source as

$$P_R(z_i, 0) \approx \left[\frac{2\pi i}{r_R}\right]^{1/2} \sum_j \psi_j(z_i, 0)\, \psi_j(z_R, r_R)\, [\xi_j(r_R)]^{-1/2} e^{-i\int_0^{r_R}\xi_j(r)\,dr}. \qquad (1.20)$$

Here a constant density of $\rho = 1$ is assumed, and a slightly different scaling factor (consistent with that found in [Brekhovskikh and Lysanov]) is used in place of the one found in Section 1.2.2.

The key to the source localization algorithm [Rouseff (1989)] is that we can form a "filtered" version of P_t by calculating

$$S(z_t, r_t; z_R, r_R) \equiv \int_0^{h(0)} P_R^*(z, 0) P_t(z, 0)\,dz, \qquad (1.21)$$

where $h(0)$ is the depth at the receiving array. Using the orthonormality of the modes

allows us to write

$$S(z_t, r_t; z_R, r_R) = \frac{2\pi}{[r_R r_t]^{1/2}} \times$$

$$\sum_j \psi_j(z_t, r_t) \psi_j(z_R, r_R) [\xi_j(r_R)\xi_j(r_t)]^{-1/2} e^{-i\int_{r_R}^{r_t} \xi_j(r)\,dr}.$$

$$(1.22)$$

Due to the form of the eigenfunctions and the accumulated phase (in the exponential) in Eq. 1.22, the function $S(z_t, r_t; z_R, r_R)$ can be interpreted as an approximation of the field due to the source at (z_t, r_t) that would be incident on an array located at the range of the reference sources. We can say that by using the depth-variable reference source we have created a "virtual" receive array at range r_R.

The holographic field S now allows us to localize the source using a matched-field approach such that the range over which the propagation must be modeled is greatly reduced. Specifically, we can calculate replica fields $K(z_R, r_R; z', r')$ at the location in range of the virtual array using local estimates of the propagation parameters for hypothetical source locations (z', r'). Then, as an analogue to Eq. 1.18, we calculate

$$Q(z', r') \equiv \int_0^{h(r_R)} K(z_R, r_R; z', r') S^*(z_t, r_t; z_R, r_R) dz_R.$$

$$(1.23)$$

It can be shown [Mourad *et al.*] that the Q function will attain a maximum value as $(z', r') \rightarrow (z_t, r_t)$.

A treatise on this "holographic array processing" (HAP) algorithm for source localization can be found in [Al-Kurd]. The contribution of this work is on several fronts. First, it contains a detailed examination of the focusing condition. Next it treats the case where one or both of the arrays (receive and/or virtual) are truncated, i.e., do not span the

13

entire water column. It can be shown that truncation of the virtual array has much more of a de-focusing effect on the algorithm than truncation of the receive array. Finally, the performance of the algorithm in ambient noise is examined, and specifically how it is affected by the SNR of the reference sources.

1.4. Preview to the Dissertation

Chapter 2 of this dissertation will outline the basic theory behind the acoustic field extrapolation algorithm. It will start by discussing a possible situation in which extrapolated acoustic fields may be desired. It will then examine some theoretical material from the field of optics, namely Huygens' principle and the Fresnel-Kirchhoff diffraction formula, which will serve as motivation for the field extrapolation algorithm. The idea of acoustically "calibrating" an underwater environment will be briefly discussed. Assuming a range-independent medium, the extrapolation algorithm will then be stated. It will be shown how combining fields that are modeled over the extrapolated distance with the calibration data via a specialization of Huygens' principle can produce an approximation to the actual field that would be incident on a receiving array. It will be seen how modal-dependent "obliquity factors" distort the extrapolated field representation. An alternate field extrapolation algorithm will be stated, which, when averaged with the results of the first algorithm, cancels the effects of the obliquity factors to first order. The two estimates will be compared to monopole and dipole secondary source contributions from Huygens' principle. It will then be shown that, for range-dependent media (both in the adiabatic approximation and for coupled mode environments), acoustic calibration takes the range-dependence into account and can provide accurate extrapolations. The idea of reciprocal calibration will be briefly mentioned.

Chapter 3 will illustrate some of the mathematical concepts from Ch. 2 through numerical simulation. Specifically, it will explore the sensitivity of the extrapolation

algorithm to one fundamental property of an underwater acoustic environment - the "steepness" of energy propagating through it. It will be shown how environments that support energy with high grazing angles are more severely impacted by the higher order terms of the obliquity factors. Several methods of comparing extrapolated and "ground truth" fields will be presented. Two qualitative comparisons are transmission loss plots and phase space representations (Argand diagrams). A quantitative measure called the matching coefficient will be introduced. A method for approximating the degradation in the matching coefficient based on approximations of the obliquity factors will be detailed.

Chapter 4 will explore the sensitivity of the extrapolation algorithm to mismatch in the modeled fields. Mismatch occurs when insufficient and/or incorrect knowledge of the parameters of the medium that govern acoustic propagation are used as input to the modeling algorithm. A perturbational approach will be used wherein errors in the environmental parameters will manifest themselves in perturbations to the normal modes (eigenfunctions and eigenvalues), and the previously developed normal mode representations of the fields will be used to analyze the errors. Mismatch due to errors in the water column sound speed profile and some sediment parameters (sound speed, attenuation, and density) will be considered. Methods for approximating the degradation in the matching coefficient based on approximations of the horizontal wavenumber perturbations (as for the obliquity factors) will be detailed.

Chapter 5 will begin by exploring the sensitivity of the extrapolation algorithm to the spacing of transmitters/receivers along the reference arrays. It will be shown how a Fourier theory approach can be used to analyze how increasing the spacing can degrade the performance of the algorithm when trapezoidal, i.e., simple summation, numerical integration (quadrature) techniques are used. It will be shown how the use of an inner product quadrature formula (I.P.Q.F.), which explicitly utilizes the mode functions of the modeled field, can be used to estimate the integral. This technique requires that the

number of transmitters/receivers along the reference arrays be greater than or equal to the number of modes that contribute significantly to the fields for that environmental scenario. It will also be shown how the I.P.Q.F. can be modified in order to cancel the obliquity factors.

Chapter 6 will then summarize the dissertation and provide suggestions for future work.

Chapter 2: Acoustic Field Extrapolation - Theory

2.1. Introduction to Chapter 2

This chapter will outline the basic theory behind the procedure for extrapolating acoustic fields in the ocean through the combined use of measured acoustic data and acoustic field modeling methods. An idealized geometry where the propagation conditions are known exactly will be described. The idea of "acoustic calibration" will then be discussed, as will Huygens' principle and its relevance to the field extrapolation algorithm. Mathematical formulations for the ideal scenario will be stated, and an expression involving a combination of field estimates with different "obliquity factors," which can be seen to approximate contributions from monopole and dipole secondary sources, will be presented. Range-dependent scenarios will then be discussed.

2.2. Problem Discussion

A situation where acoustic field prediction is required is shown in Figure 2.1. We want to predict the field at the arbitrarily placed hypothetical receiver due to the arbitrarily placed hypothetical source. It is known that for short ranges in the vicinity of the
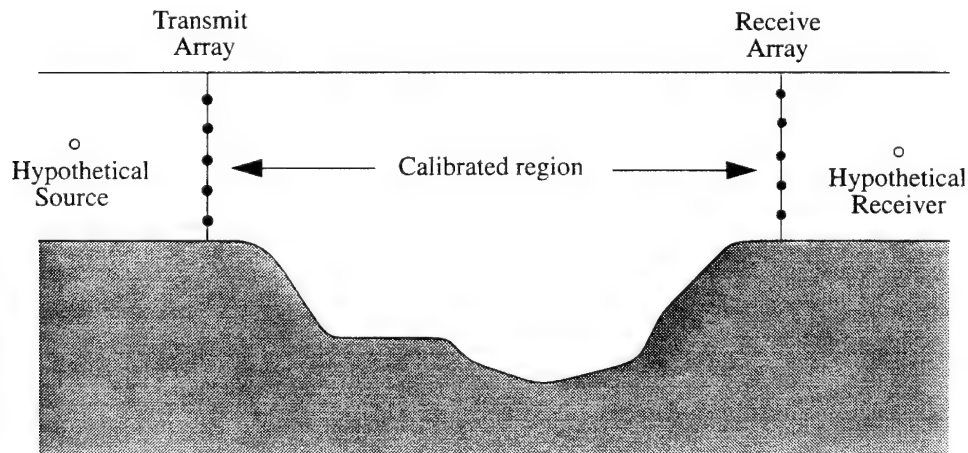
Figure 2.1. Scenario of extrapolation problem.

hypothetical source and receiver that reliable knowledge about the environmental conditions that affect acoustic propagation can be obtained, and, therefore, that reliable estimates of the acoustic fields can be calculated through numerical modeling. It is also known, however, that a relatively large region between the source and receiver has unknown or difficult to measure acoustic propagation properties, leading to difficulties in predicting acoustic fields across this region through numerical modeling methods alone.

Now we place vertical arrays of sources and receivers near the boundaries of the "unknown" region so that by transmitting and receiving acoustic energy through this part of the medium it is "calibrated." This situation is much like that seen in the HAP algorithm in Section 1.3, and that development should give us a clue as to how to proceed in predicting the acoustic fields between hypothetical sources and receivers that are located outside the calibrated region. In the next section, we will examine Huygens' principle which will give us further guidance in how to proceed.

2.3. Huygens' Principle

The Dutch physicist Christian Huygens (1629-1695) presented his theory on the nature of light in 1678. Huygens postulated that if the position of a wavefront was known at time $t = 0$, then any point on the wavefront could be considered as the location of a "secondary source" which could produce secondary spherical wavelets. At some later time $t = t_1$, the position of the wavefront would be the tangent surface to these secondary wavelets. This idea is illustrated in Fig. 2.2. Huygens' principle can be applied to all wave phenomena [Halliday and Resnick], including acoustic waves.

An interesting application of Huygens' principle from the field of optics serves as a motivation for our underwater acoustic application. Imagine the situation pictured in Fig. 2.3 with an infinite plane screen and a finite aperture. A point source at P_2 illuminates the aperture with the field
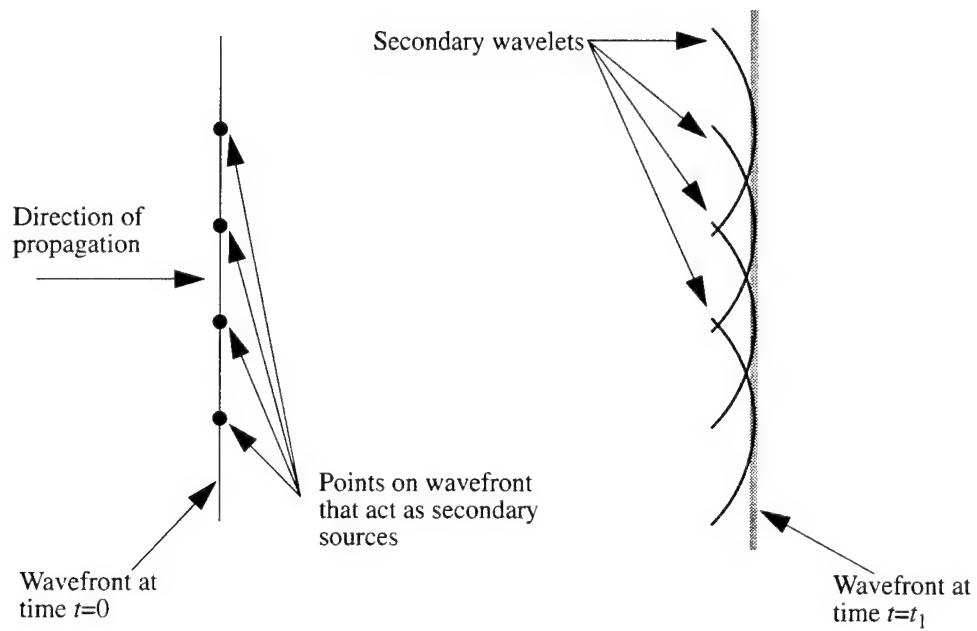
Figure 2.2. Illustration of Huygens' principle.
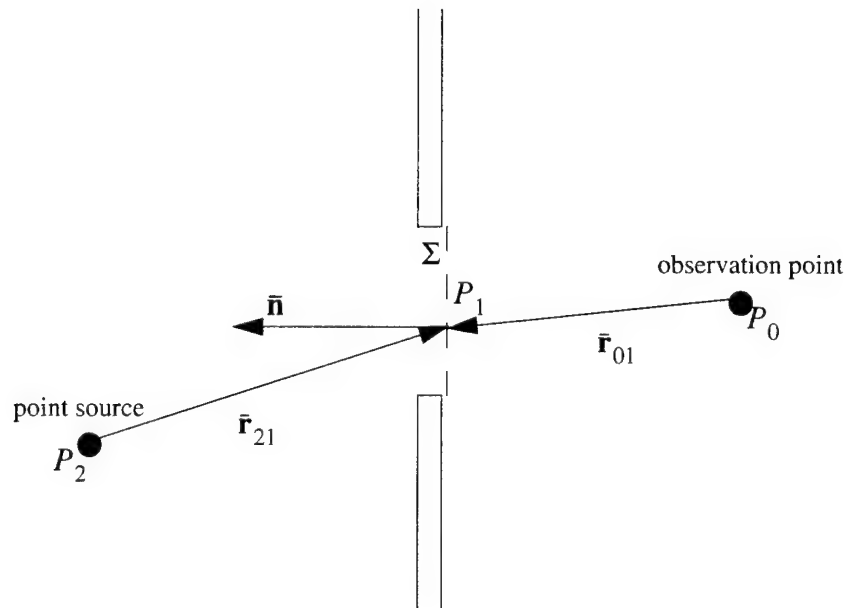
Figure 2.3. Infinite plane screen with finite aperture.

$$U(P_1) = \frac{Ae^{jkr_{21}}}{r_{21}}, \tag{2.1}$$

where A is an arbitrary amplitude factor, r_{21} is the length of the vector pointing from P_2 to P_1, and $k = 2\pi/\lambda$ is the wave number with λ the wavelength of the assumed monochromatic light. The so-called Huygens-Fresnel principle (an interpretation of the Fresnel-Kirchhoff diffraction formula) [Goodman] states that the field at P_0 can be approximated by

$$U(P_0) \cong \iint\limits_{\Sigma} U'(P_1)\frac{e^{jkr_{01}}}{r_{01}}ds \ , \tag{2.2}$$

where Σ denotes the two-dimensional area of the aperture and

$$U'(P_1) = \frac{1}{j\lambda}\left[\frac{Ae^{jkr_{21}}}{r_{21}}\right]\left[\frac{\cos{(\bar{\mathbf{n}}, \bar{\mathbf{r}}_{01})} - \cos{(\bar{\mathbf{n}}, \bar{\mathbf{r}}_{21})}}{2}\right]$$

$$= N U(P_1)\theta(\bar{\mathbf{n}}, \bar{\mathbf{r}}_{01}, \bar{\mathbf{r}}_{21}), \tag{2.3}$$

where $N = (j\lambda)^{-1}$, $\cos{(\bar{\mathbf{a}}, \bar{\mathbf{b}})}$ denotes the cosine of the angle between the two vectors, and θ will be referred to as an "obliquity factor." The rest of the integrand in Eq. 2.2 (apart from $U'(P_1)$) can be thought of as the free-space Green's function for the region on the right of the screen.

Eq. 2.2 implies that "the field at P_0 arises from an infinity of fictitious 'secondary' point sources located within the aperture itself." As mentioned above, θ is called an obliquity factor and applies a scaling to each secondary source that is dependent on the directions of the true point source and the observation point relative to the position of the given secondary source. This can be thought of as applying a "directivity pattern" to each

secondary source. We will draw analogies to this situation in our acoustic field extrapolation derivation.

2.4. An Idealized Geometry and Acoustic Calibration

Figure 2.4 is a schematic of the idealized geometry that will be used for the initial development of the theory behind the acoustic calibration algorithm. Ultimately, we will be interested in the acoustic pressure $p = p(r_c, z_c)$ at the receiver due to a source emitting a cw signal of frequency f from the coordinates $(0, z_0)$. Our ideal ocean will be assumed to be a time-invariant horizontally stratified acoustic waveguide of depth h meters characterized by a range-independent sound speed profile $c(z)$. The ocean surface is modeled as a planar free (or pressure release) surface, and the ocean bottom is modeled as a perfectly rigid planar surface (see Sec. 1.2.1 for a discussion of boundary conditions).

For this development, the water column will be assumed to be spanned by an ideal transmitting array at range r_a and an ideal receiving array at range r_b as shown in Fig. 2.4. These reference arrays are ideal in the sense that sound can be transmitted from any point z_a along the transmit array such that $0 < z_a < h$, and sound can be received at any point z_b along the receive array such that $0 < z_b < h$, i.e., the arrays are not limited by having fixed, discrete transducer locations. This allows for continuous integration of functions along the arrays. For the more realistic situation of fixed transducer locations, numerical integration
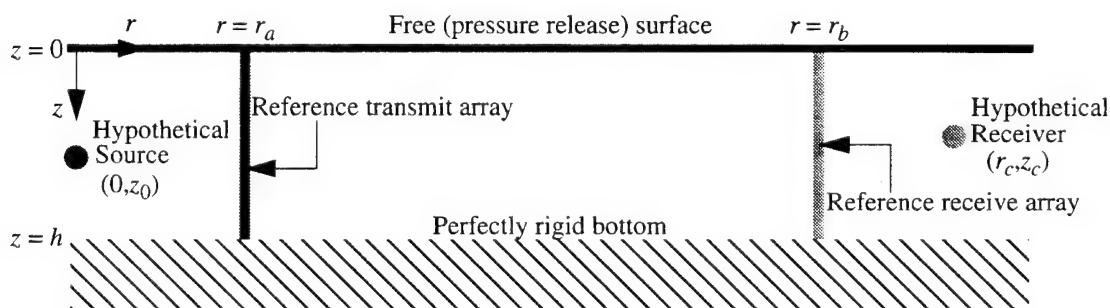
Figure 2.4. Idealized geometry for acoustic calibration algorithm.

(quadrature) techniques can be used. Also, the assumption will be made that the source, receiver, and reference arrays are all in a common vertical plane.

This acoustic field extrapolation algorithm is based on the idea of acoustic calibration of the medium as was the HAP algorithm in Sec. 1.3. A given region of ocean is calibrated by transmitting a cw signal of frequency f from all depths $0 < z_a < h$ along the reference transmit array and recording the resulting complex pressure field as a function of depth along the reference receive array for all depths $0 < z_b < h$. This process essentially gives us a spatial impulse response, or Green's function, describing the propagation of sound from r_a to r_b, $G(r_b, z_b; r_a, z_a)$. It will be assumed that the reference transmit array and the hypothetical source operate at the same frequency f, which will then be implicit for all expressions of pressure and Green's functions to follow.

The idea now is to use this "calibration" data to predict what the acoustic pressure would be at the receiver at coordinates (r_c, z_c) due to the source at coordinates $(0, z_0)$. Once the calibration (Green's function) data have been collected, the algorithm proceeds as follows: 1) estimate a value related to the pressure field (to be described later) at the transmit reference array $(r = r_a)$ due to the source using local environmental information at the array and an acoustic field modeling method, 2) combine the results of step 1) with the measured Green's function via a specialization of Huygens' principle to obtain an estimate of the pressure field along the receive reference array $(r = r_b)$, 3) estimate a value related to the Green's function (to be described later) between the receive reference array and the receiver (between r_b and r_c) using local environmental information at the array and an acoustic field modeling method, and 4) combine the result of step 2) with the result of step 3) via a specialization of Huygens' principle to obtain an estimate of the pressure at the receiver.

The calibration range $r_{cal} = r_b - r_a$ is assumed to be much greater than either of the "extrapolation" ranges, $r_{e1} = r_a$ or $r_{e2} = r_c - r_b$. The main idea behind the

algorithm is, as mentioned in Sec. 2.2, that the calibration procedure will measure the acoustic transmission properties of the medium between the arrays and incorporate this knowledge into the field estimate, removing the effects of medium variability that would be difficult to determine using only environmental measurements.

2.5. Mathematical Statement of Acoustic Field Extrapolation Algorithm

For this part of the development it is assumed that the propagation properties of the medium, i.e., the range-independent sound speed profile $c(z)$ and subsequently the normal mode decomposition, are known perfectly for the modeling steps. If this were the case in true applications, there would be no advantage to using the extrapolation algorithm since one of the other propagation simulation methods mentioned in Ch. 1 could be used to predict the acoustic field over the entire range. This assumption, however, is helpful in developing the theory. The more realistic cases of range-dependent propagation and mismatch between the assumed properties and the true properties will be dealt with in later sections.

A normal mode representation will be used for both the measured (calibration) and modeled fields. It should be noted that this representation is not a requirement of the theory for this part of the development, i.e., the modeled fields could be generated using any of a number of acoustic field modeling methods. This representation is useful, however, in showing the mathematical relationships between the actual and extrapolated fields.

2.5.1. Field Extrapolation to the Reference Receive Array

Assuming that the medium has been acoustically calibrated between r_a and r_b (giving us $G(r_b, z_b; r_a, z_a)$), the first step in predicting the field at (r_c, z_c) is to extrapolate a modeled field (due to the source at $(0, z_0)$) along the reference transmit array at range r_a to the receive array at range r_b. As mentioned above, this can be accomplished by

combining the modeled field with the Green's function data via a specialization of Huygens' principle. One way to do this is to define [Rouseff (Feb. 1993)]

$$\tilde{p}'(r_b, z_b) \equiv N_a' \int_0^h \hat{p}(r_a, z_a) G(r_b, z_b; r_a, z_a) dz_a = N_a' I_a', \qquad (2.4)$$

where the tilde denotes that this is an extrapolated value, the prime corresponds to this particular method of combining the information, N_a' is a scaling constant to be determined, and $\hat{p}(r_a, z_a)$ is a modeled field along the reference transmit array due to the hypothetical source. This is a modification of Eq. 2.2 where we are now integrating in one dimension, the measured Green's function $G(r_b, z_b; r_a, z_a)$ takes the place of the free space Green's function $e^{jkr_{01}}/r_{01}$, and $\hat{p}(r_a, z_a)$ takes the place of $U'(P_1)$. Note that the "incident" field, $\hat{p}(r_a, z_a)$, is not modified as its counterpart is in Eqs. 2.2-3.

Using the range-independent normal mode-based expression for underwater acoustic fields (Eq. 1.10), we can express the modeled field $\hat{p}(r_a, z_a)$ as

$$\hat{p}(r_a, z_a) = p(r_a, z_a) \cong \left[\frac{i}{8\pi r_a}\right]^{1/2} \frac{1}{\rho(z_0)} \sum_m \psi_m(z_0)\psi_m(z_a)\xi_m^{-1/2} e^{i\xi_m r_a}. \qquad (2.5)$$

The caret indicates that this is a modeled pressure field based on local environmental data. Since the assumption of perfect knowledge about the environment has been made, the estimate is equal to the true pressure field (the approximate equality is used due to the Hankel function approximation from Eq. 1.9). Assuming that $r_b > r_a$, the Green's function can also be represented using a normal mode decomposition by

$$G(r_b, z_b; r_a, z_a) \cong \left[\frac{i}{8\pi(r_b - r_a)}\right]^{1/2} \frac{1}{\rho(z_a)} \sum_m \psi_m(z_a)\psi_m(z_b)\xi_m^{-1/2} e^{i\xi_m(r_b - r_a)}. \qquad (2.6)$$

Combining Eqs. 2.4-6 and taking the integral inside the summations we find that

$$I_a' \cong \frac{i}{8\pi \left[r_a \left(r_b - r_a \right) \right]^{1/2} \rho(z_0)} \times$$

$$\sum_m \sum_n \psi_m(z_0) \psi_n(z_b) e^{i \left[\xi_m r_a + \xi_n (r_b - r_a) \right]} \left(\xi_m \xi_n \right)^{-1/2} \left[\int_0^h \frac{\psi_m(z_a) \psi_n(z_a)}{\rho(z_a)} dz_a \right].$$

(2.7)

Since the integral at the end of Eq. 2.7 is a Kronecker delta function δ_{mn} (due to the orthonormality property of the mode functions - see Sec. 1.2.1), the double summation collapses and

$$I_a' \cong \frac{i}{8\pi \left[r_a \left(r_b - r_a \right) \right]^{1/2} \rho(z_0)} \sum_m \psi_m(z_0) \psi_m(z_b) \xi_m^{-1} e^{i \xi_m r_b}.$$

(2.8)

The true pressure field at the receive reference array would be

$$p(r_b, z_b) \cong \left[\frac{i}{8\pi r_b} \right]^{1/2} \frac{1}{\rho(z_0)} \sum_m \psi_m(z_0) \psi_m(z_b) \xi_m^{-1/2} e^{i \xi_m r_b}.$$

(2.9)

Note that the differences between Eqs. 2.8 and 2.9 occur in the range scaling in front of the summation, and the power of the horizontal wavenumber inside the summation (-1 vs. $-1/2$). N_a' can now be chosen so as to make $\tilde{p}'(r_b, z_b)$ a better approximation to $p(r_b, z_b)$ [Rouseff (Feb. 1993)]. By setting

$$N_a' = \left[\frac{8\pi k_{ref} r_a \left(r_b - r_a \right)}{i \qquad r_b} \right]^{1/2}$$

(2.10)

where k_{ref} is a reference wavenumber (see Eq. 1.13 and accompanying discussion), Eq. 2.4 becomes

$$\tilde{p}'(r_b, z_b) \cong \left[\frac{i}{8\pi r_b}\right]^{1/2} \frac{1}{\rho(z_0)} \sum_m \psi_m(z_0)\psi_m(z_b)\xi_m^{-1/2} e^{i\xi_m r_b}\left[\frac{k_{ref}}{\xi_m}\right]^{1/2}. \qquad (2.11)$$

Note that the extra $\xi_m^{-1/2}$ has been combined with the k_{ref} in order to form a modal-dependent multiplier. This multiplier will be discussed in the next section.

Care must be taken in applying the normalization constant N_a' in practice, especially if absolute field level is the desired result. This is due to the fact that some numerical modeling codes use different conventions for normalizing their output fields (see Eq. 1.10).

2.5.2. The Obliquity Factor

The expressions for the "ground truth" field $p(r_b, z_b)$ and the extrapolated field $\tilde{p}'(r_b, z_b)$ due to the hypothetical source differ only in the modal-dependent multiplier

$$\theta_m' = \left[\frac{k_{ref}}{\xi_m}\right]^{1/2}, \qquad (2.12)$$

where we will call θ_m' an "obliquity factor" [Rouseff (April 1993)]. In referring back to the Huygens-Fresnel principle (Eqs. 2.2-3), which was the motivation for our acoustic field extrapolation formulation, we see that the obliquity factor (which depended on the source-aperture-receiver geometry) was included in the integration as a modifier to the incident field. Here, however, the incident (modeled) field was used unaltered, and the obliquity factor appears in our estimate of the observed field. Indeed, if a normal mode formulation is used for the modeled field, a modified scaling of each mode could be applied to account for the obliquity factor. For now, however, we will assume a general formulation in that no modifications of this kind will be made to the incident field. This allows for the use of any type of acoustic field modeling algorithm in generating the

modeled fields.

In addition, the obliquity factor takes on a geometric interpretation as it does in the optics application. Keeping in mind that the approximate grazing angle for each mode can be given by

$$\chi_m \sim \text{acos}\left[\frac{\xi_m}{k_{ref}}\right],$$ (2.13)

we can say that for each mode in the estimated field

$$\theta_m' \sim (\cos\chi_m)^{-1/2}.$$ (2.14)

Since lower order modes propagate with grazing angles close to horizontal, we can say that $\theta_m' \approx 1$ for these modes. Progressively steeper grazing angles, however, lead to an overweighting of the higher-order modes compared to the true pressure field. For environments where high-order modes propagate over long distances, this can significantly degrade the estimate (examples will be shown in Ch. 3). Figure 2.5 shows a plot of the obliquity factor vs. grazing angle. The gray line shows $\theta_m' = 1$ for reference.
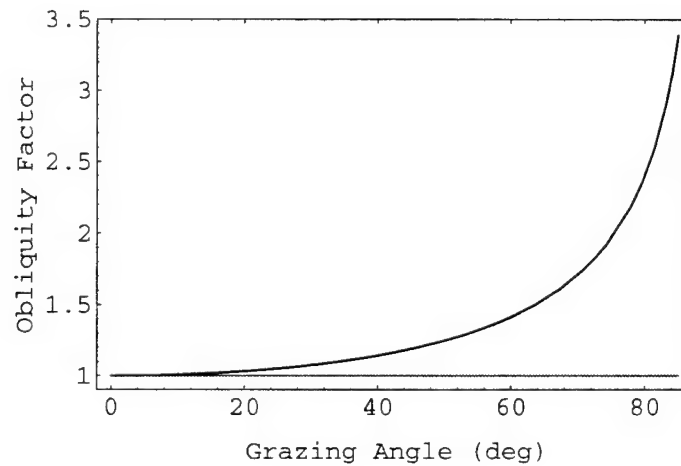
Figure 2.5. Obliquity factor vs. grazing angle.

The obliquity factor tends to infinity as the grazing angle tends to $90°$.

2.5.3. An Alternate Extrapolation Formula and Obliquity Factor

We can form an alternate extrapolation formula by defining [Rouseff (April 1993)]

$$\tilde{p}''(r_b, z_b) \equiv N_a'' \int_0^h \left[\frac{\partial \hat{p}(r_a, z_a)}{\partial r_a} \right] G(r_b, z_b; r_a, z_a) dz_a = N_a'' I_a''. \tag{2.15}$$

Here the secondary sources take on the amplitude and phase of the range derivative of the incident field. In practice the derivative of the modeled quantity can be obtained through discrete difference methods or direct computation. Differentiating Eq. 2.5 gives

$$\frac{\partial \hat{p}(r_a, z_a)}{\partial r_a} \cong \left[\frac{i}{8\pi} \right]^{1/2} \frac{1}{\rho(z_0)} \sum_m \psi_m(z_0) \psi_m(z_a) \xi_m^{-1/2} e^{i\xi_m r_a} \left[i\xi_m r_a^{-1/2} - \frac{r_a^{-3/2}}{2} \right]. \tag{2.16}$$

We will neglect the range term to the -3/2 power for this analysis since it is dominated by the other range term as range increases. So doing will greatly simplify the following results.

Inserting this result into Eq. 2.15 and taking advantage of the orthonormality of the mode functions as before gives

$$I_a'' \cong \frac{-1}{8\pi \left[r_a (r_b - r_a) \right]^{1/2}} \frac{1}{\rho(z_0)} \sum_m \psi_m(z_0) \psi_m(z_b) e^{i\xi_m r_b}. \tag{2.17}$$

As was done for N_a' and $\tilde{p}'(r_b, z_b)$, N_a'' can be chosen so as to make $\tilde{p}''(r_b, z_b)$ a better approximation to $p(r_b, z_b)$ by setting

$$N_a'' = \left[\frac{8\pi}{i^3} \frac{r_a (r_b - r_a)}{k_{ref} r_b} \right]^{1/2} \tag{2.18}$$
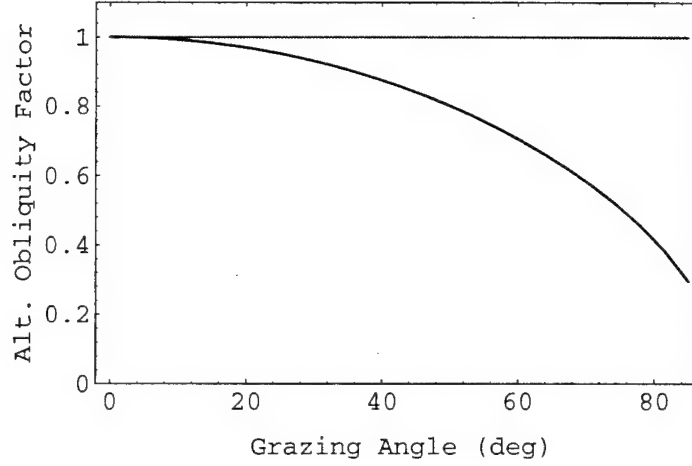
Figure 2.6. Alternate obliquity factor vs. grazing angle.

which leads to

$$\tilde{p}''(r_b, z_b) \cong \left[\frac{i}{8\pi r_b}\right]^{1/2} \frac{1}{\rho(z_0)} \sum_m \psi_m(z_0) \psi_m(z_b) \xi_m^{-1/2} e^{i\xi_m r_b} \left[\frac{\xi_m}{k_{ref}}\right]^{1/2}.$$ (2.19)

In this case the obliquity factor is

$$\theta_m'' = \left[\frac{\xi_m}{k_{ref}}\right]^{1/2} \sim (\cos\chi_m)^{1/2},$$ (2.20)

which leads to an underweighting of the higher-order modes compared to the true pressure field. Figure 2.6 is a plot of this alternate obliquity factor vs. grazing angle. This obliquity factor tends to zero as the grazing angle tends to $90°$.

The Huygens-Fresnel principle (an interpretation of the Fresnel-Kirchhoff diffraction formula) is an approximate solution to the plane screen diffraction problem that is derived from the integral theorem of Helmholtz and Kirchhoff (see [Goodman] and [Porter *et al.* (1992)]). This theorem can be stated as

$$\mathbf{U}(P_0) = \frac{1}{4\pi} \iint_S \left(\frac{\partial \mathbf{U}}{\partial n} \mathbf{G} - \mathbf{U} \frac{\partial \mathbf{G}}{\partial n} \right) ds$$

(2.21)

where S is a closed surface surrounding the point P_0, $\mathbf{G}$ is the Green's function, and the derivatives are normal to the surface. An interpretation of this formula from the standpoint of Huygens' principle is that the field at P_0 is the result of both monopole secondary sources that radiate the Green's function and dipole secondary sources that radiate the normal derivative of the Green's function [Porter (1994)].

The extrapolation algorithm of Eq. 2.15 can be thought of as an approximation to the monopole contribution from the Helmholtz-Kirchhoff integral, since we can think of the secondary sources having the amplitude and phase of the spatial derivative of the incident field, and radiating the Green's function. The extrapolation algorithm of Eq. 2.4 can be thought of as an approximation to the dipole contribution from the Helmholtz-Kirchhoff integral in the sense that the secondary sources take on the amplitude and phase of the incident field itself rather than its spatial derivative. In general, the spatial derivatives of acoustic fields are difficult to measure, and since for the extrapolation algorithm the Green's function is measured data, we consider the approximation

$$\frac{\partial \mathbf{G}}{\partial r_a} \cong \sum_m W_m \psi_m(z) \varphi_m,$$

(2.22)

where φ is a geometry dependent multiplier. It's form is similar to the multiplier seen in Eq. 2.16, and is encompassed in the obliquity factor θ_m'.

2.5.4. The Averaged Obliquity Factor

We now have two ways to synthesize our estimated field, one that overweights and one that underweights contributions according to grazing angle. While the Helmholtz-Kirchhoff integral implies that a differencing operation should take place between the
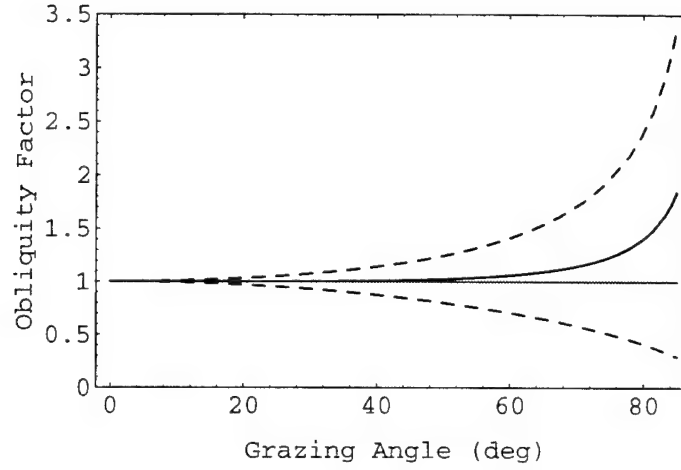
Figure 2.7. Averaged obliquity factor vs. grazing angle.

monopole and dipole contributions in order to determine the observed field, we have artificially scaled the two contributions so that they are each better approximations to the observed field. In this case, averaging the two components is more appropriate, i.e.,

$$\tilde{p}(r_b, z_b) = \frac{\tilde{p}'(r_b, z_b) + \tilde{p}''(r_b, z_b)}{2}. \tag{2.23}$$

Since Eqs. 2.11 and 2.19 differ only in the obliquity factors, we can think of their average as having a new mode-dependent obliquity factor θ_m. Fig. 2.7 shows a comparison of the two previously plotted obliquity factors (dashed lines) with the averaged one (solid line) vs. grazing angle.

As an example, consider a mode with a grazing angle of 60 degrees. Its contribution to the estimate $\tilde{p}'(r_b, z_b)$ would be ~1.41 times what its contribution to the true pressure field $p(r_b, z_b)$ would be, while its contribution to the estimate $\tilde{p}''(r_b, z_b)$ would only be ~0.71 times what it should be. Averaging the two estimates results in a contribution of ~1.06 times its proper contribution. The averaged obliquity factor is closer to 1 than either of the other two for all but the steepest grazing angles, but it still tends to infinity as the grazing angle moves toward 90 degrees.

One way to analyze the averaging effect is to consider the ξ_m as perturbations from the reference wavenumber k_{ref} [Rouseff (April 1993), Porter *et al.* (1993), Fox *et al.*],

$$\xi_m = k_{ref} (1 - \varepsilon_m), \tag{2.24}$$

where ε_m is assumed small. Expanding the obliquity factors in a Taylor series about $\varepsilon_m = 0$ gives

$$\theta_m{}' = (1 - \varepsilon_m)^{-1/2} = 1 + \frac{1}{2}\varepsilon_m + O(\varepsilon_m^2)$$

$$\theta_m{}'' = (1 - \varepsilon_m)^{1/2} = 1 - \frac{1}{2}\varepsilon_m + O(\varepsilon_m^2). \tag{2.25}$$

Averaging the right hand sides results in a cancellation of the first order terms. The field estimate $\tilde{p}(r_b, z_b)$ is, therefore, said to be "invariant" to first order errors introduced by the obliquity factors [Porter *et al.* (1993)].

It may be surmised from Fig. 2.7 that the higher order terms from Eq. 2.23 become significant for the steeper grazing angles. If we continue the Taylor series expansion out to second and third order terms, we obtain

$$\theta_m{}' = (1 - \varepsilon_m)^{-1/2} = 1 + \frac{1}{2}\varepsilon_m + \frac{3}{8}\varepsilon_m^2 + \frac{5}{16}\varepsilon_m^3 + O(\varepsilon_m^4)$$

$$\theta_m{}'' = (1 - \varepsilon_m)^{1/2} = 1 - \frac{1}{2}\varepsilon_m - \frac{1}{8}\varepsilon_m^2 - \frac{1}{16}\varepsilon_m^3 + O(\varepsilon_m^4). \tag{2.26}$$

Since $\varepsilon_m > 0$, averaging the right-hand sides of Eq. 2.26 shows that second and third order terms are not canceled and are positive. This accounts for the upturn in the averaged curve of Fig. 2.7. Note that the Helmholtz-Kirchhoff integral is an exact formulation. Our errors are due to the facts that we are integrating in one dimension along the linear reference

array instead of over a closed surface and that we have used the measured Green's function instead of its spatial derivative in the dipole contribution.

2.5.5. Field Extrapolation to the Receiver

The value $\tilde{p}(r_b, z_b)$ can now be extrapolated further in order to predict the pressure field at the receiver located at coordinates (r_c, z_c) [Rouseff (Feb. 1993)]. In extrapolating out to the reference receive array, environmental data local to the reference transmit array were used as input to an acoustic field modeling routine to predict a pressure field and its range derivative at the reference transmit array (due to the hypothetical source at coordinates $(0, z_0)$). These estimates were then combined with the measured Green's function data in order to calculate the extrapolated field. Extrapolating from r_b to r_c is a dual problem of the first case. Now the Green's function between $r = r_b$ and $r = r_c$, $\hat{G}(r_c, z_c; r_b, z_b)$, and its range derivative at $r = r_b$ must be modeled based on environmental data at the reference receive array, and then combined with $\tilde{p}(r_b, z_b)$.

Specifically, we will now define

$$\tilde{p}'(r_c, z_c) \equiv N_b' \int_0^h \tilde{p}(r_b, z_b) \hat{G}(r_c, z_c; r_b, z_b) dz_b = N_b' I_b'. \tag{2.27}$$

Using the approximation $\tilde{p}(r_b, z_b) \cong p(r_b, z_b)$, the math follows much as before, and we can set

$$N_b' = \left[\frac{8\pi}{i} \frac{k_{ref} r_b (r_c - r_b)}{r_c} \right]^{1/2}. \tag{2.28}$$

We also define

$$\tilde{p}''(r_c, z_c) \equiv N_b'' \int_0^h \tilde{p}(r_b, z_b) \left[\frac{\partial \hat{G}(r_c, z_c; r_b, z_b)}{\partial r_b} \right] dz_b \qquad (2.29)$$

and set

$$N_b'' = \left[8\pi i \frac{r_b(r_c - r_b)}{k_{ref} r_c} \right]^{1/2}. \qquad (2.30)$$

The obliquity factors work out as before, so our final estimate of the pressure at the receiver is

$$\tilde{p}(r_c, z_c) = \frac{\tilde{p}'(r_c, z_c) + \tilde{p}''(r_c, z_c)}{2}. \qquad (2.31)$$

The flow diagram in Fig. 2.8 gives an overview of the extrapolation algorithm. Note that the part of the algorithm that deals with extrapolating from the receive reference array to the hypothetical receiver could also be used alone in the case where there was an actual source, there was no transmit reference array, and the field generated by the source was measured along the receive reference array. In other words, measuring the field along the array would allow one to extrapolate that field for hypothetical receiver locations beyond the array.

2.5.6. Adiabatic Propagation and Acoustic Field Extrapolation

We now consider the situation where the medium varies slightly with range and the adiabatic approximation adequately describes the pressure fields. This section will consider only the part of the extrapolation algorithm that estimates the field along the receive reference array due to a hypothetical source outside the calibration region.

First we will assume that the medium is adiabatic between the reference arrays and
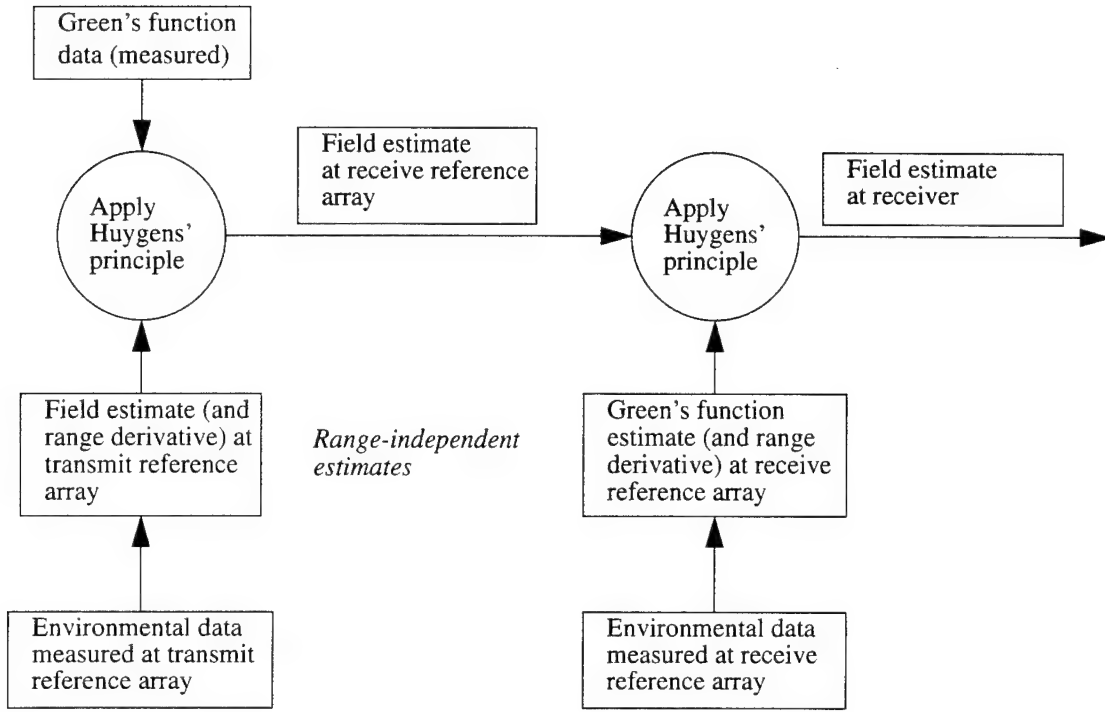
Figure 2.8. Flow diagram of extrapolation algorithm.

range-independent outside this region (much as is pictured in Fig. 2.1). We can, therefore, write the true pressure along the receive reference array as

$$
p(r_b, z_b) \cong \left[\frac{i}{8\pi r_b} \right]^{1/2} \frac{1}{\rho(z_0)} \times
$$

$$
\sum_m \psi_m(r_0, z_0) \psi_m(r_b, z_b) \xi_m(r_b)^{-1/2} e^{i\left[\xi_m(r_a)r_a + \int_{r_a}^{r_b} \xi_m(r')dr' \right]},
$$

(2.32)

keeping in mind that $\psi_m(r, z) = \psi_m(r_a, z)$ and $\xi_m(r) = \xi_m(r_a)$ for $0 \leq r \leq r_a$ due to the range-independence in the region near the hypothetical source. We can also write the measured Green's function as

$$G(r_b, z_b; r_a, z_a) \cong \left[\frac{i}{8\pi (r_b - r_a)} \right]^{1/2} \frac{1}{\rho(z_a)} \times$$

$$\sum_m \psi_m(r_a, z_a) \psi_m(r_b, z_b) \xi_m(r_b)^{-1/2} e^{i \int_{r_a}^{r_b} \xi_m(r') dr'}.$$

(2.33)

Applying the specialization of Huygens' principle as for the previous case (using Eqs. 2.4-5, 2.10, and 2.33), we find that

$$\tilde{p}'(r_b, z_b) \cong \left[\frac{i}{8\pi r_b} \right]^{1/2} \frac{1}{\rho(z_a)} \times$$

$$\sum_m \psi_m(r_0, z_0) \psi_m(r_b, z_b) \xi_m(r_b)^{-1/2} e^{i \left[\xi_m(r_a) r_a + \int_{r_a}^{r_b} \xi_m(r') dr' \right]} \left[\frac{k_{ref}}{\xi_m(r_a)} \right]^{1/2}.$$

(2.34)

The only difference between the extrapolated field (Eq. 2.34) and the true field (Eq. 2.32) is the modal-dependent obliquity factor, as was the case for the ideal range-independent case. The acoustic calibration step, therefore, takes into account the range-dependence of the medium that would be difficult to measure by direct sampling of the environmental properties. The same technique of using the range derivative of the modeled pressure field at the reference array to form another estimate and averaging the two estimates can be used to ameliorate the effects of the obliquity factor.

2.5.7. Coupled Modes and Acoustic Field Extrapolation

We now will show how the acoustic calibration step can also take into account more severe environmental variability to aid in predicting acoustic fields. For environments where the adiabatic approximation does not hold, we can use the coupled mode formulation for underwater acoustic fields.

In order to keep the math tractable, we will work with the problem of extrapolating
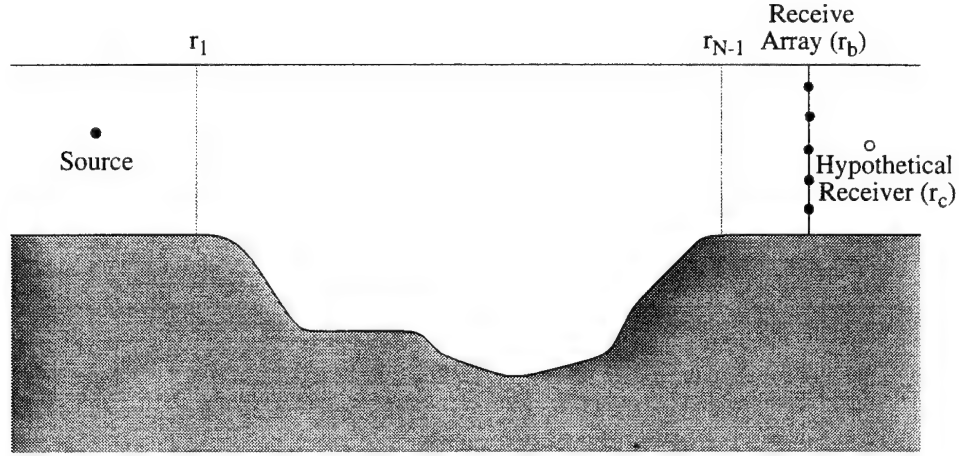
Figure 2.9. Scenario for extrapolation in coupled mode environment.

a field received along a reference receive array as pictured in Fig. 2.9 (it was noted earlier that this is a dual problem of predicting the field along an array due to a hypothetical source). We are assuming that the acoustic energy from the source has travelled through a part of the medium that must be described using coupled mode theory, and that the extrapolation region is range-independent.

Using the coupled mode theory described in Sec. 1.2.3, we can write the pressure field measured along the receive array as

$$p_N(r_b, z_b) = \sum_m A_{N,m} H1_{N,m}(r_b) \psi_{N,m}(z_b), \tag{2.35}$$

and the desired pressure field at the hypothetical receiver as

$$p_N(r_c, z_c) = \sum_m A_{N,m} H1_{N,m}(r_c) \psi_{N,m}(z_c), \tag{2.36}$$

since $B_{N,m} = 0$ [Evans] (see Eq. 1.16). We write the estimated Green's function in the region near the reference receive array as (again assuming perfect knowledge of the environmental conditions for $r > r_b$)

$$\hat{G}(r_c, z_c; r_b, z_b) = G(r_c, z_c; r_b, z_b) \cong$$

$$\left[\frac{i}{8\pi (r_c - r_b)} \right]^{1/2} \frac{1}{\rho_N(z_b)} \sum_m \psi_{N,m}(z_b) \psi_{N,m}(z_c) \xi_{N,m}^{-1/2} e^{i\xi_{N,m}(r_c - r_b)}, \tag{2.37}$$

which is our usual range-independent estimate with perfect knowledge of the environmental parameters that affect the propagation.

Combining Eqs. 2.35 and 2.37 via Eq. 2.27 and taking account of the orthonormality of the modes at range $r = r_b$ results in

$$I_b' = \left[\frac{i}{8\pi (r_c - r_b)} \right]^{1/2} \sum_m A_{N,m} H1_{N,m}(r_b) \psi_{N,m}(z_c) \xi_{N,m}^{-1/2} e^{i\xi_{N,m}(r_c - r_b)}. \tag{2.38}$$

Considering the asymptotic expansion of $H1_{N,m}(r)$ for any $r > r_{N-1}$,

$$H1_{N,m}(r) = \frac{\left[\frac{2}{\pi \xi_{N,m} ri} \right]^{1/2} e^{i\xi_{N,m}r}}{\left[\frac{2}{\pi \xi_{N,m} r_{N-1} i} \right]^{1/2} e^{i\xi_{N,m}r_{N-1}}} = \left[\frac{r_{N-1}}{r} \right]^{-1/2} e^{i\xi_{N,m}(r - r_{N-1})} \tag{2.39}$$

and using the normalizing constant from Eq. 2.28, i.e.,

$$N_b' = \left[\frac{8\pi}{i} \frac{k_{ref} r_b (r_c - r_b)}{r_c} \right]^{1/2}, \tag{2.40}$$

we find that

$$\tilde{p}_N'(r_c, z_c) = \sum_m A_{N,m} H1_{N,m}(r_c) \psi_{N,m}(z_c) \left[\frac{k_{ref}}{\xi_{N,n}} \right]^{1/2}. \tag{2.41}$$

Eq. 2.41 is the now familiar result of the true pressure field with modal-dependent

obliquity factors (compare with Eq. 2.36). The same technique of averaging estimates can be used to lessen the effect of the obliquity factor. The point here is that, as for the case of mild range dependence where the adiabatic approximation could be used to describe the calibrated data, the calibration step can also effectively take into account environments for which coupled mode formulations must be used to describe the propagation. Once this part of the medium has been calibrated, reliable field extrapolations can take place.

We also briefly note that known range dependencies in the extrapolation regions can be taken into account by the modeled fields through use of range-dependent modeling schemes. This can improve the fidelity of the extrapolated fields. The case of range-dependent bathymetry is considered in [Rouseff *et al.*].

2.5.8. Reciprocal Calibration

One form of the principle of acoustic reciprocity is stated simply in [Kinsler *et al.*] as "if in an unchanging environment the locations of a small source and a small receiver are interchanged, the received signal will remain the same." An informative application which utilizes the reciprocity principle can be found in [Dowling]. Applying this to the situation pictured in Fig. 2.4, we can say that calibrating by transmitting from $r = r_a$ and receiving at $r = r_b$ is the same as calibrating by transmitting from $r = r_b$ and receiving at $r = r_a$. In other words, fields can be extrapolated due to hypothetical sources either in the region $r < r_a$ or $r > r_b$ using the one-way calibration data. One way to think of this is to write

$$G(r_a, z_a; r_b, z_b) = G^T(r_b, z_b; r_a, z_a),\qquad(2.42)$$

where T represents a transpose operation.

2.6. Summary of Chapter 2

This chapter has outlined the basic theory behind the acoustic field extrapolation algorithm. The problem of predicting acoustic fields over long ranges that include environments with unknown or difficult to determine propagation conditions was discussed, and how deploying vertical arrays of transmitters and receivers may aid in this effort. Huygens' principle and an interpretation of the Fresnel-Kirchhoff diffraction formula (the Huygens-Fresnel principle) were discussed in order to motivate our extrapolation formula. An ideal range-independent ocean waveguide was described, and the idea of acoustic calibration using reference arrays spanning the medium in depth was introduced.

Perfect knowledge of the propagation conditions was assumed, and a mathematical statement for this extrapolation was presented that used a modification of the Fresnel-Kirchhoff diffraction formula. An obliquity factor in the expression for the extrapolated field, analogous to that seen in the optics example, was described. By forming two versions of the extrapolated field and averaging them (one based on an estimate of the pressure field at the reference transmit array and the other on its range derivative), the first-order effects of the obliquity factor were negated. The two estimates were likened to monopole and dipole secondary source contributions from Huygens' principle. It was then shown how the field can be extrapolated to a receiver in the vicinity of the reference receive array using similar methods.

Range-dependence in the medium (for the case of adiabatic propagation as well as full mode coupling) was discussed, and it was seen that the extrapolation formulas stated for the range-independent case were still valid. It was also shown how the roles of the reference transmit and receive arrays can be interchanged due to the acoustic reciprocity principle.

The following chapter will illustrate some of the mathematical relationships

expressed in this chapter through numerical modeling.

Chapter 3: Acoustic Field Extrapolation - Numerical Modeling

3.1. Introduction to Chapter 3

This chapter will use numerical modeling methods to illustrate the acoustic field extrapolation algorithm discussed in Ch. 2. These examples will only illustrate the part of the algorithm that extrapolates the acoustic pressure field to the reference receive array $(r = r_b)$. The extrapolated field will be compared to a "ground truth" estimate of the acoustic field (computed using perfect knowledge of the medium and a conventional numerical propagation method) along the array.

The normal mode computer program KRAKEN [Porter (1992)] will be used to synthesize all modeled fields in these examples. The first examples will examine the effects of the obliquity factor on the extrapolation algorithm in an acoustic waveguide with perfectly reflecting boundaries and no attenuation. The extrapolated and ground truth fields will be compared qualitatively through the use of transmission loss and phase space plots, as well as quantitatively through the use of a matching coefficient. Additionally, a measure that characterizes a given environment called the obliquity characterization number will be defined, and its relationship to the matching coefficient will be examined. Finally, the effects of an attenuating sediment layer on the algorithm will be illustrated.

In this chapter and the rest of the dissertation, examples will be numbered using the convention of a number followed by a letter, where the number is the chapter number and the letter (A,B,C,...) differentiates examples within that chapter.

3.2. Obliquity Factor Effects: Rigid Bottom (Example 3A)

An expression was derived in Sec. 2.5 for the extrapolated pressure field at the reference receive array, $\tilde{p}(r_b, z_b)$, due to a source at position $(0, z_0)$. This estimated field is the result of averaging two extrapolated fields that deviate from the "ground truth" field by modal-dependent obliquity factors. By averaging these two estimates, the effect of the

obliquity factors is cancelled to first order. This example will utilize a simple environmental scenario to illustrate the procedure.

3.2.1. Modal Structure

The simulated ocean for Ex. 3A will follow the idealized geometry of Sec. 2.4. We assume a pressure release ocean surface and a perfectly rigid bottom. The operating frequency will be $f = 150$ Hz. The depth of the ocean will be $h = 50$ m, and the sound speed profile will be range-independent and also constant with depth. The calibration range will be $r_{cal} = 20$ km. The reference transmit and receive arrays will be populated with ideal point sources with spacing $\Delta z_t = \Delta z_r = 1$ m. Figure 3.1 is a schematic for this scenario.

For Ex. 3A we will use a constant sound speed $c(z) = 1500$ m/s. KRAKEN calculates 10 propagating modes for this scenario, and the mode functions are plotted in Fig. 3.2. The dashed gray lines in the plots represent zero pressure, and each mode is individually normalized by the maximum amplitude of that mode. Also note how each mode, or eigenfunction, satisfies the boundary conditions: the pressure is zero at $z = 0$ and the derivative of the pressure is zero at $z = h$. The horizontal wavenumber, or eigenvalue, of each mode is tabulated (to three decimal places) along with the approximate grazing angle (to one decimal place) in Table 3.1. Note that for this situation, the mode
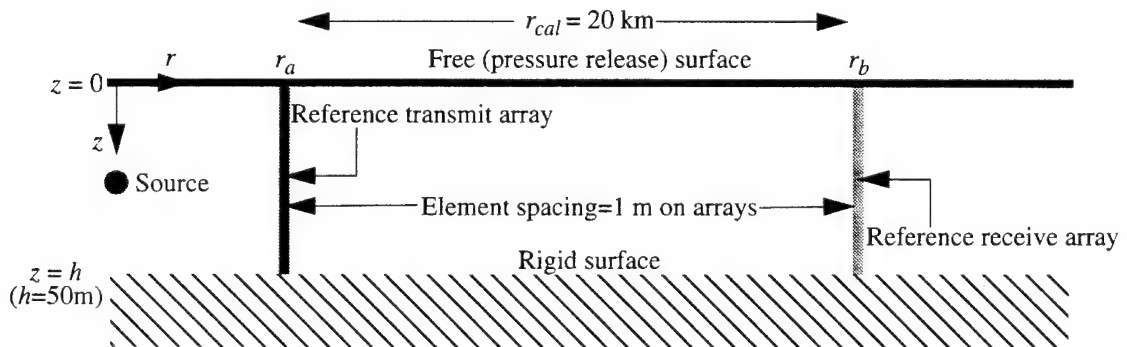
Figure 3.1. Geometry for Exs. 3A and 3B.
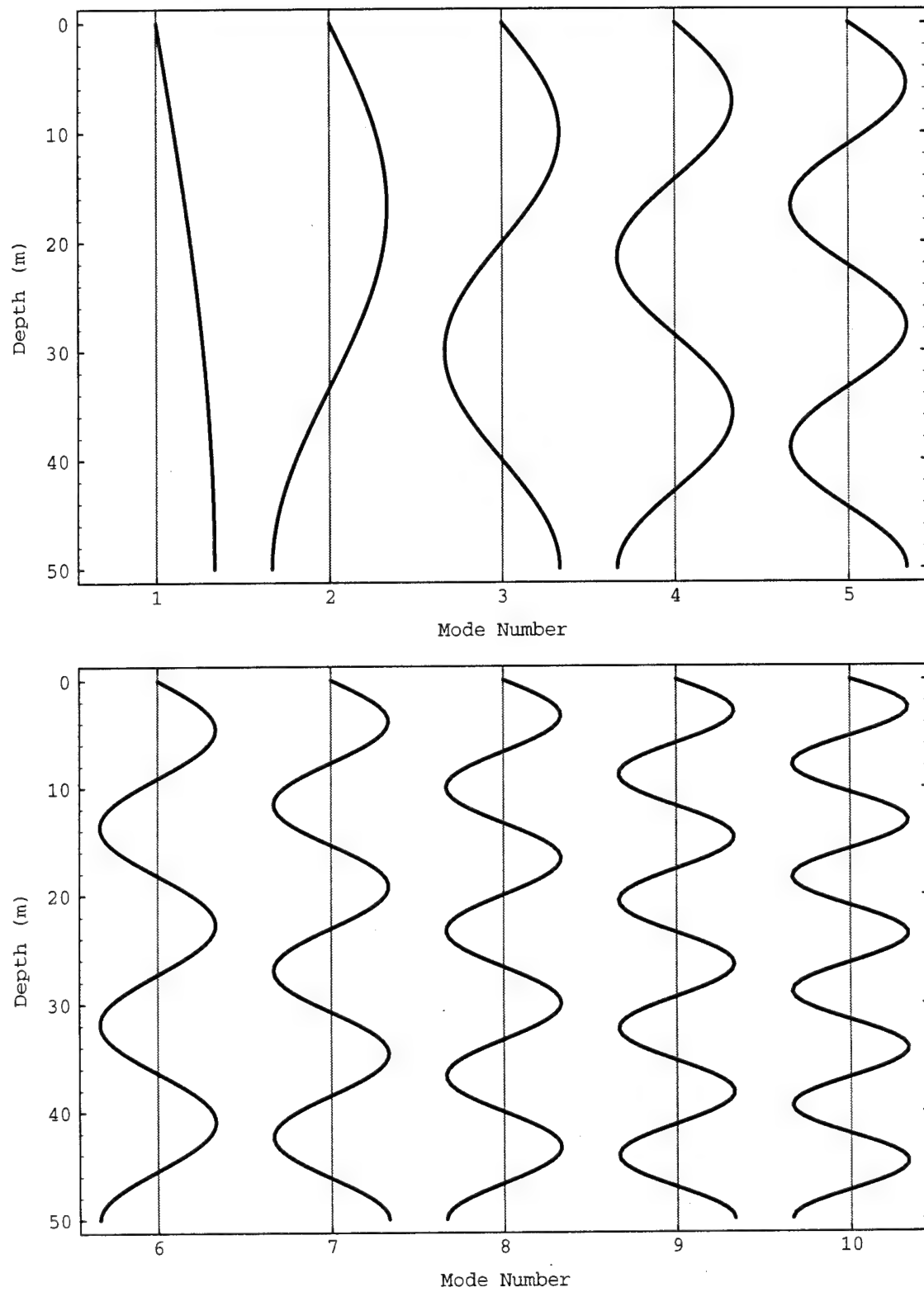
Figure 3.2. Mode functions for Ex. 3A.

Table 3.1. Eigenvalues for Ex. 3A.

Mode # (m)	Eigenvalue (ξ_m)	Grazing Angle (χ_m) (deg.)
1	0.628	2.9
2	0.621	8.6
3	0.608	14.5
4	0.589	20.5
5	0.561	26.7
6	0.525	33.4
7	0.477	40.5
8	0.416	48.6
9	0.331	58.2
10	0.196	71.8

functions and horizontal wavenumbers can be obtained analytically [Boyles] and represented as

$$\xi_m = \left[k^2 - \left(\frac{(2m-1)}{h} \frac{\pi}{2} \right)^2 \right]^{1/2}$$

$$\psi_m(z) = \left[\frac{2}{h} \right]^{1/2} \sin\left[(k^2 - \xi_m^2)^{1/2} z \right] \tag{3.1}$$

for $m = 1, 2, 3, \ldots$

3.2.2. Primary Extrapolation

To simulate calibration of the medium, we numerically model the fields that would be incident on the receive reference array due to the sources along the transmit reference

array, giving us a discrete version of $G(r_b, z_b; r_a, z_a)$. We then place a hypothetical source $r_a = 3$ km from the reference transmit array and $z_s = 25$ m in depth and numerically model what the field would be along the reference transmit array, $\hat{p}(r_a, z_a)$. We now apply Eq. 2.4 in order to extrapolate the field to the reference receive array. A simple trapezoidal rule is used to approximate the integral (numerical integration issues will be addressed in Ch. 5).

Figure 3.3 shows comparisons of the extrapolated field to the "ground truth" field which is calculated by numerically modeling the field along the receive reference array due to the hypothetical source. Figure 3.3a compares the transmission loss of the fields. Transmission loss is defined as

$$TL(r, z) = -20\log\left|\frac{p(r, z)}{p^0(r)\big|_{r = 1}}\right|, \tag{3.2}$$

where

$$p^0(r) = \frac{e^{ikr}}{4\pi r} \tag{3.3}$$

is the expression for the pressure due to the source in free space. Large transmission loss values correspond to small acoustic pressures, hence the inverted nature of the scaling on the y-axis.

In Fig. 3.3a the black line represents the ground truth transmission loss curve, and the gray line represents the extrapolated estimate. Note how the extrapolated transmission loss curve is consistently above the ground truth curve, but especially so near the peaks in the curve. Equations 1.10-11 showed how the expression for the pressure field can be thought of as a linear sum of the mode functions with complex-valued weights. The extrapolated field, then, can be thought of in the same way, except with the weights
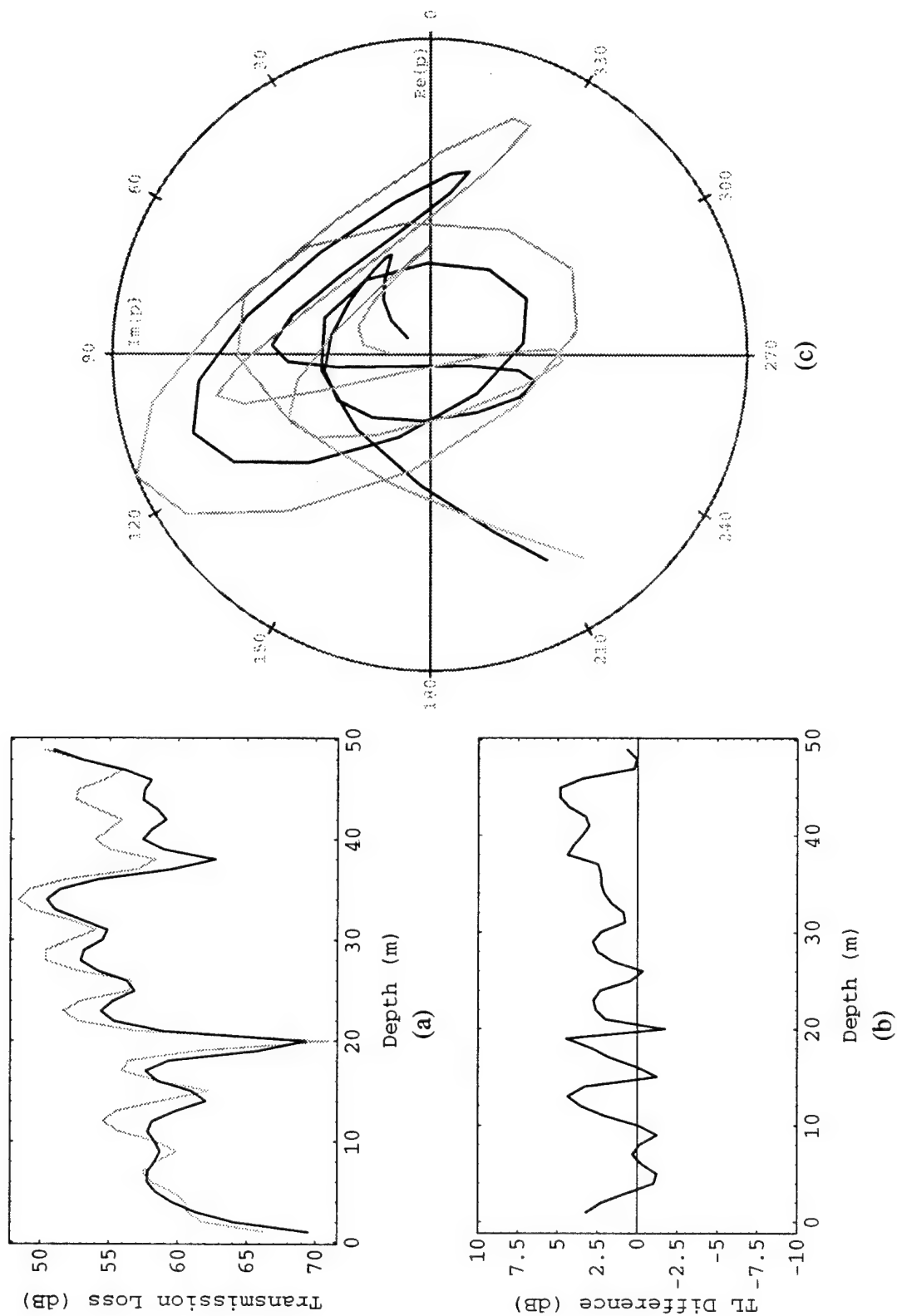
Figure 3.3. Ex. 3A: Primary field extrapolation.

multiplied by the obliquity factor. Since the peaks in the transmission loss curve are where the contributions to the pressure field tend to constructively interfere to the greatest degree, the overemphasis caused by the obliquity factors (θ_m') is most evident here. Fig. 3.3b is simply the difference between the estimated and true transmission loss curves in Fig. 3.3a.

No information about the phase of the extrapolated field is available through examining transmission loss only. Figure 3.3c is a so-called "Argand diagram" [Uscinski]. It shows the trajectory, parameterized by depth, of the complex-valued pressure fields in phase space. The outside circle represents the maximum amplitude contained in either field. Again the ground truth is the black line and the extrapolated is gray. Although these diagrams can tend to be quite "busy," they can give a good qualitative feel for how close of a coherent "match" the two fields are.

A more quantitative measure is obtained by calculating the magnitude-squared of the "normalized scalar product" [Goncharov and Voronovich] of the two pressure fields. This is given by

$$|K|^2 = \frac{\left|\sum_{i=1}^{N} p1_i p2_i^*\right|^2}{\sum_{i=1}^{N}|p1_i|^2 \times \sum_{i=1}^{N}|p2_i|^2}, \tag{3.4}$$

where N is the number of receivers. For this work, $|K|^2$ will be referred to as the "matching coefficient." The maximum value of this measure is unity, and is attained when the two fields differ only by a constant complex multiplier. For the situation in Fig. 3.3, $|K|^2 \cong 0.940$.

3.2.3. Alternate and Averaged Extrapolations

We can also calculate the alternate extrapolated field given by Eq. 2.15, the results of which are shown in Fig. 3.4. The three parts of Fig. 3.4 follow the same pattern as Fig. 3.3. Note that now the amplitude of the extrapolated field is generally underestimated in comparison with the ground truth field due to the attenuating effect of the obliquity factors on the constituent modal amplitudes. Here, $|K|^2 \cong 0.936$. The averaged extrapolated field (as per Eq. 2.23) is shown in Fig. 3.5. The partial cancellation of the first two obliquity factors has brought the matching coefficient up to $|K|^2 \cong 0.982$.

It should be noted that as the location of the hypothetical source is varied in range and depth, the nature of the pressure fields produced by it will change. For example, placement of the source in depth determines to what extent each mode is excited, while placement in range affects the phase multiplier, and, hence, the constructive/destructive nature of the mode functions' interaction (see Eq. 1.10). Variation of the source position within the same environmental scenario, then, will produce small fluctuations in the matching coefficient measure for two reasons. One is that if some higher order modes are not excited to a significant extent, this will lower the effects that their obliquity factors would have on the extrapolation. The second is that the matching coefficient is somewhat sensitive to the actual shapes of the pressure waveforms. Since the errors in the extrapolated fields vary with depth, the points where the fields happen to be evaluated/ measured (i.e., the locations of receivers) may contribute more or less to a matching error. This contribution to the fluctuations will decrease as the number of receiver points is increased.

Since we are not interested in these incidental fluctuations, but rather the overall performance as a function of environment, we will average results over a grid of source locations. For this scenario, the hypothetical source location was varied over a grid of ranges from 1 km to 5 km spaced at 1 km and depths from 5 m to 45 m spaced at 5 m, and
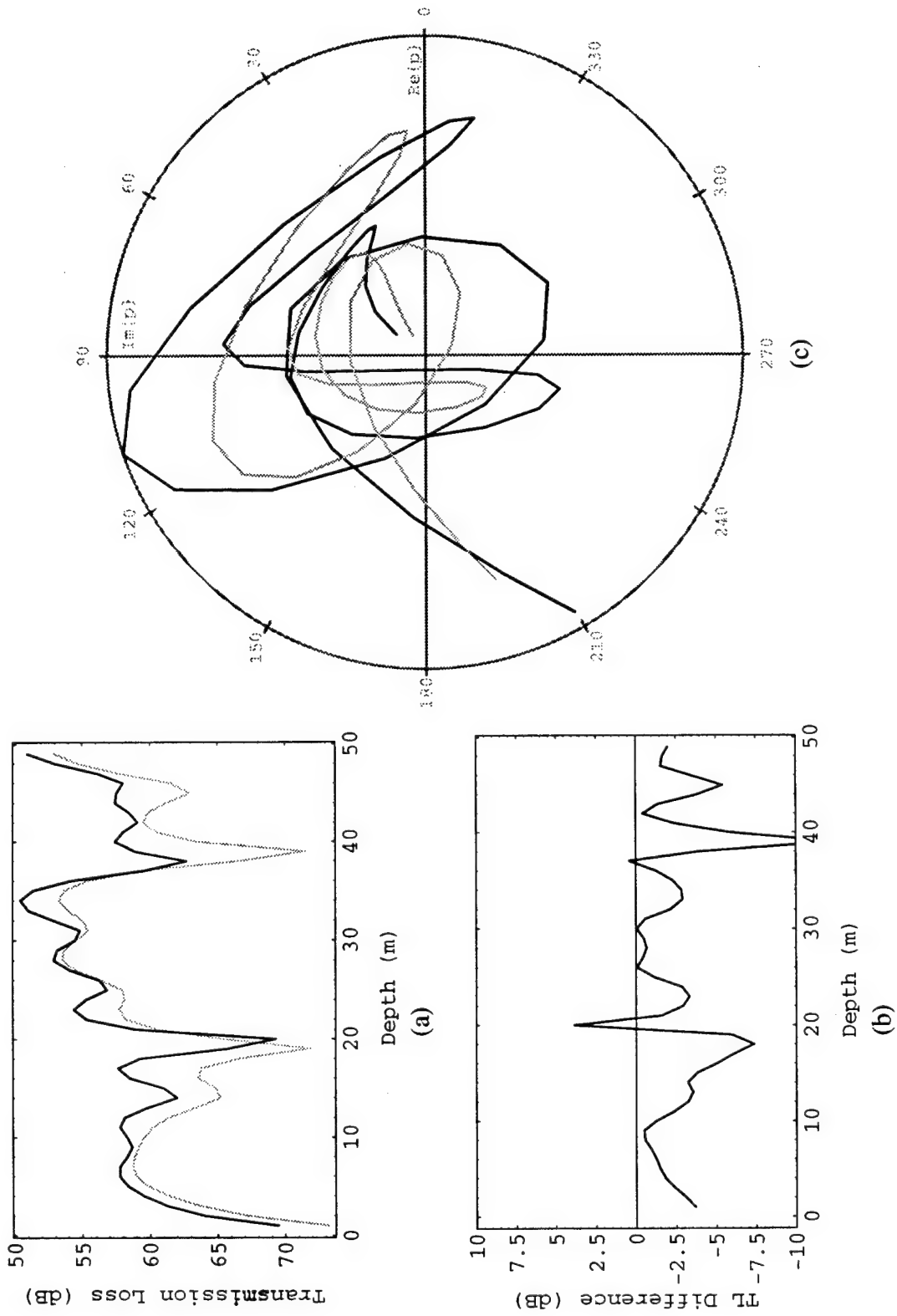
Figure 3.4. Ex. 3A: Alternate field extrapolation.
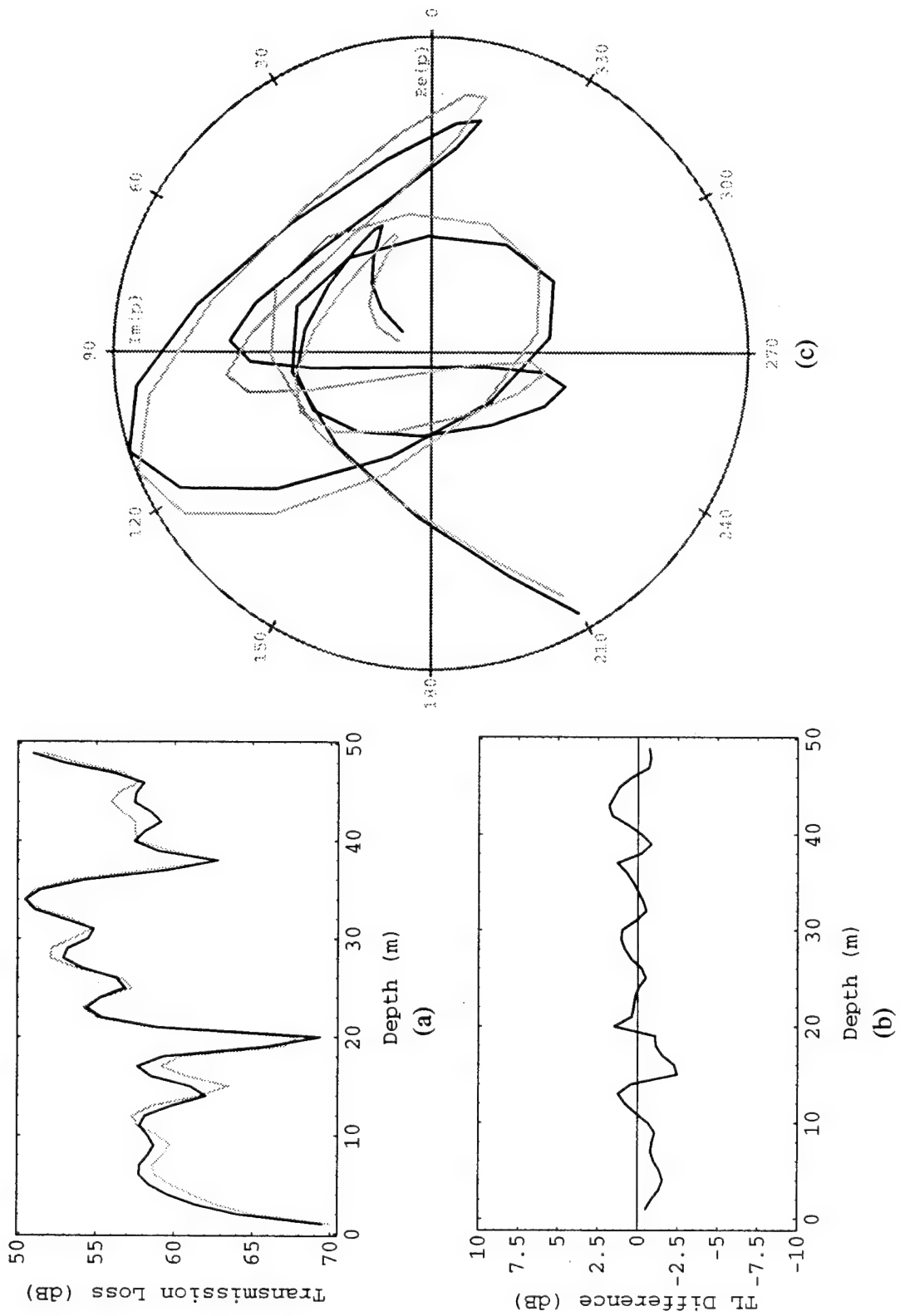
Figure 3.5. Ex. 3A: Averaged field extrapolation.

the average value of $|K|^2$ for $\tilde{p}(r, z)$ was found to be 0.984 with a variance of 7.545×10^{-5}. The range and depth of the source used in this example were then chosen for the plots because the extrapolated field for this source position gave a matching coefficient close to the average over the grid, making it a representative example.

3.3. Obliquity Factor Effects: Steeper Grazing Angles (Example 3B)

Example 3B is designed to increase the severity of the effects of the obliquity factors in comparison with Ex. 3A. The only change here from Ex. 3A will be a constant sound speed of 1570 m/s instead of 1500 m/s.

3.3.1. Modal Structure

KRAKEN calculates 10 propagating modes for Ex. 3B, with identical mode functions to those of Ex. 3A (see Fig. 3.2). This may be surprising at first, but through examination of Eq. 3.1 we see that the mode functions are sections of sine waves that must meet certain boundary conditions at the surface and bottom. The horizontal wavenumbers (eigenvalues), however, have changed and are listed in Table 3.2. Note that all the grazing angles have become steeper, leading to obliquity factors further from one for each mode when compared with those of Ex. 3A.

3.3.2 Primary, Alternate, and Averaged Extrapolations

Using a hypothetical source location $(r_{e1}, z_s) = (2 \text{ km}, 35 \text{ m})$, the extrapolated vs. ground truth field comparisons can be found in Figs. 3.6-8 with analogous ordering to those found in Ex. 3A. The matching coefficients are, respectively, 0.848, 0.782, and 0.944. For the same grid of source locations as in Ex. 3A, the average value of the matching coefficient was 0.945 with a variance of 2.719×10^{-4}. Note how the increase in the grazing angles, and consequently the distance of the obliquity factors from unity, has degraded the quality of the extrapolations in comparison with Ex. 3A.

Table 3.2. Eigenvalues for Ex. 3B.

Mode # (m)	Eigenvalue (ξ_m)	Grazing Angle (χ_m) (deg.)
1	0.599	3.0
2	0.593	9.0
3	0.579	15.2
4	0.559	21.5
5	0.530	28.1
6	0.491	35.1
7	0.440	42.9
8	0.372	51.7
9	0.274	62.8
10	0.064	83.9

3.4. Obliquity Characterization Number

At this point, we desire some simple quantity that can be calculated before any fields are measured or modeled in order to aid us in determining to what extent the acoustic field extrapolation algorithm will be affected by the obliquity factors for a given underwater environment. Since for this work our "goodness" measure is the matching coefficient, we will use that as our starting point.

We note that the summations over the discretely sampled points in depth in the definition of the matching coefficient (Eq. 3.4) can be thought of as approximations to an integral formulation, i.e.,

53
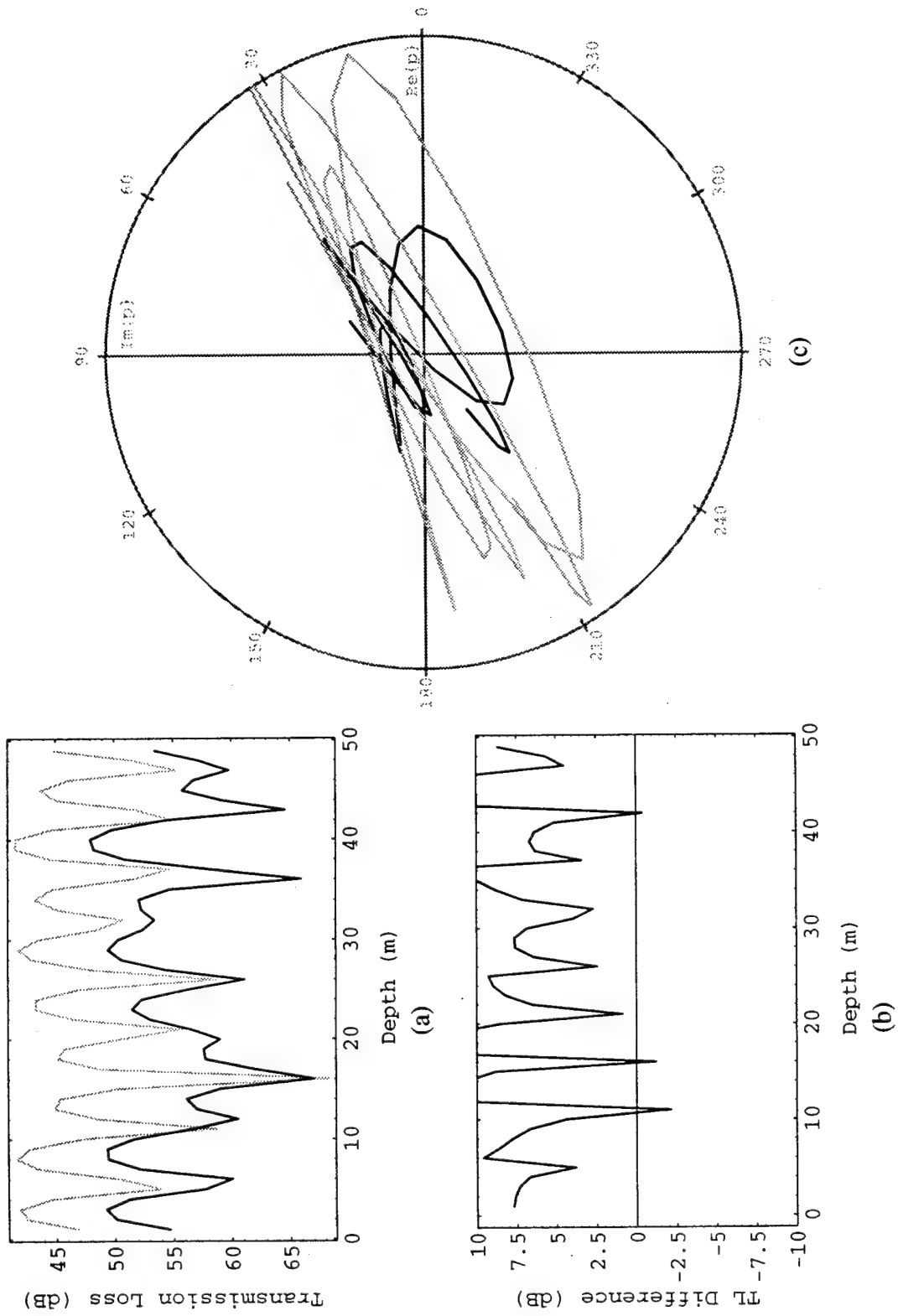
Figure 3.6. Ex. 3B: Primary field extrapolation.

54
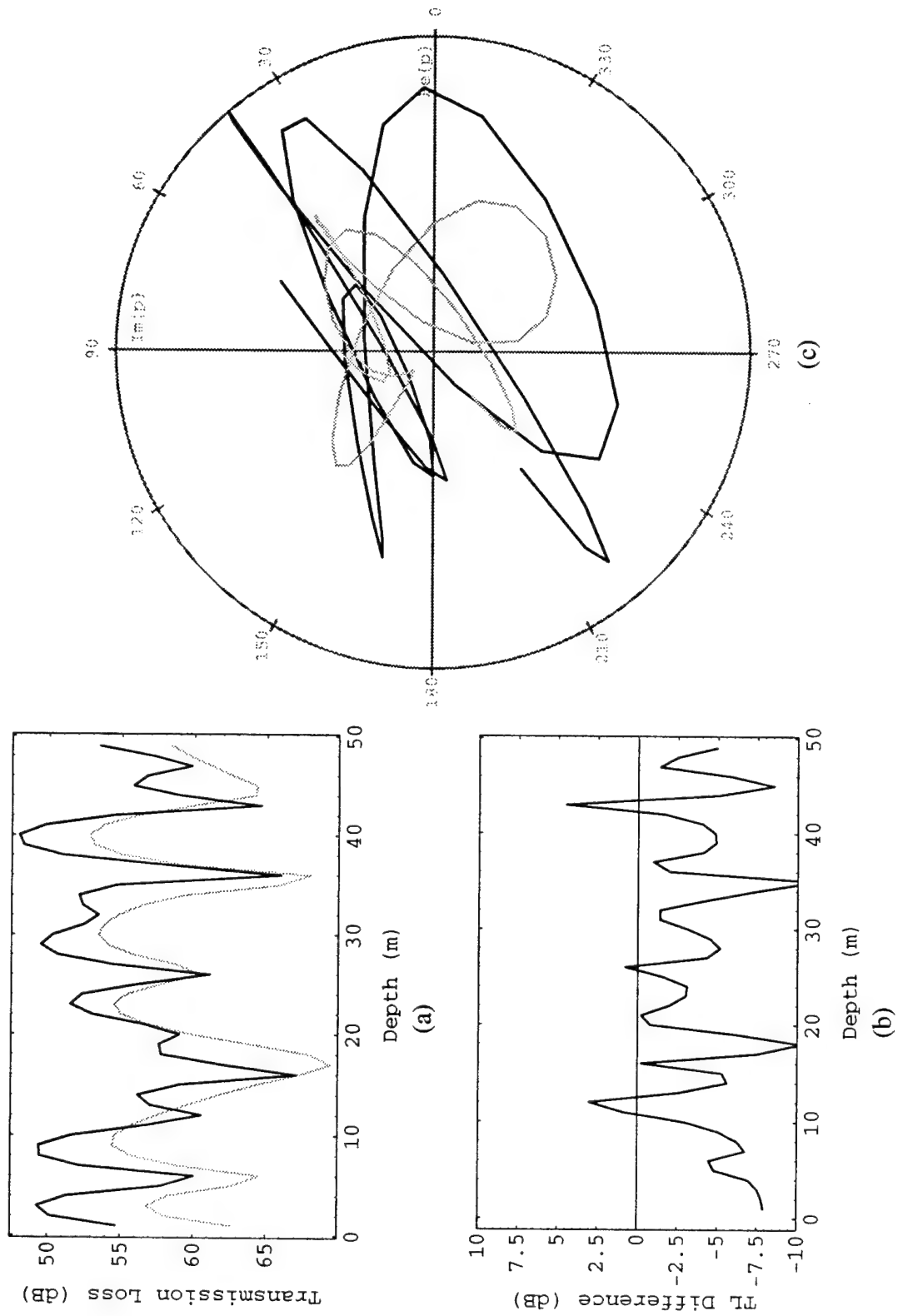
Figure 3.7. Ex. 3B: Alternate field extrapolation.
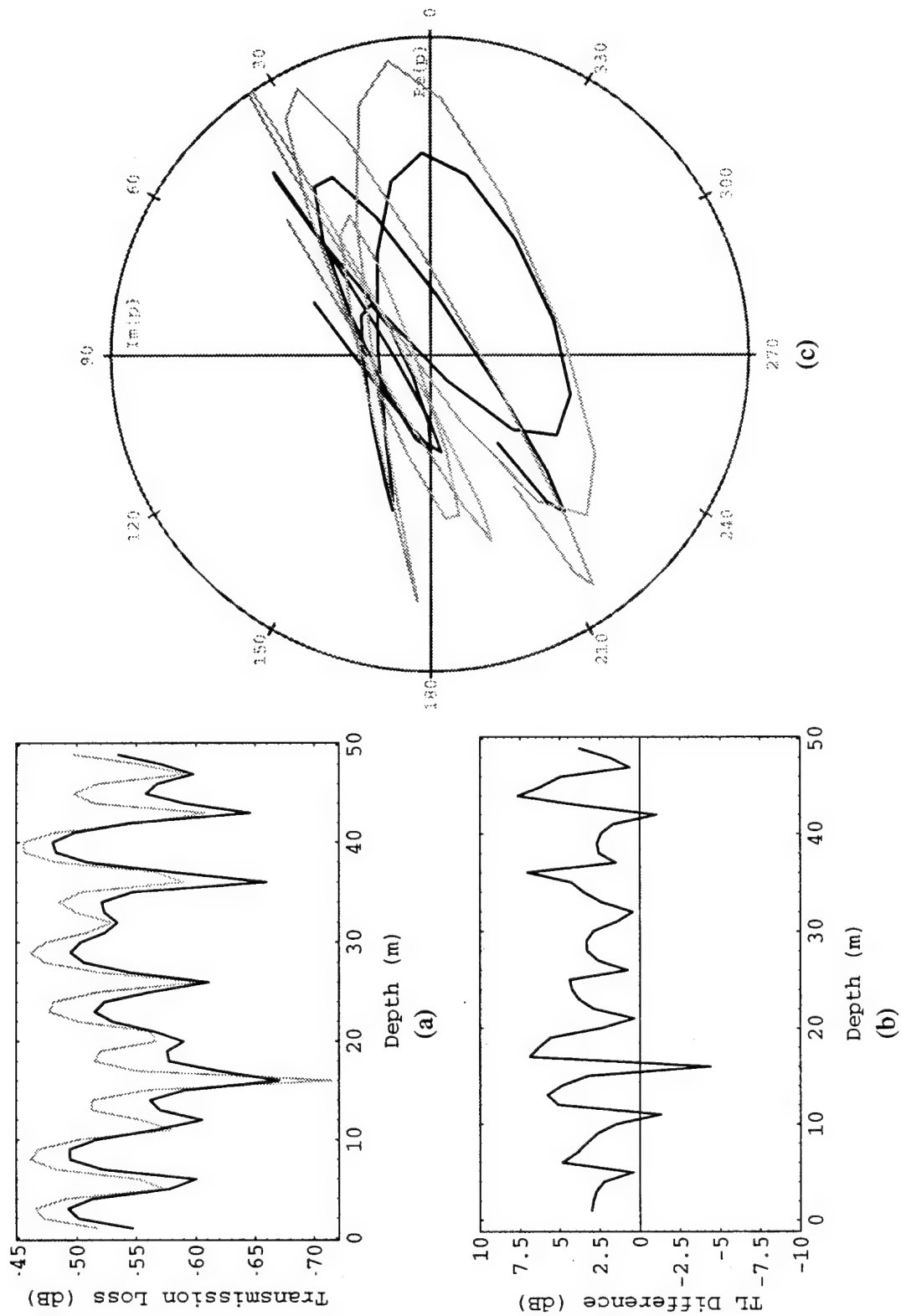
Figure 3.8. Ex. 3B: Averaged field extrapolation.

$$|K|^2 = \frac{\left|\sum_{i=1}^{N} p1_i p2_i^*\right|^2}{\sum_{i=1}^{N} |p1_i|^2 \times \sum_{i=1}^{N} |p2_i|^2} \sim \frac{\left|\int p1(z)p2^*(z)dz\right|^2}{\int |p1(z)|^2 dz \times \int |p2(z)|^2 dz}, \tag{3.5}$$

where the integrals are over the length of the array. We now substitute $\tilde{p}(z)$ (the extrapolated field) for $p1(z)$ and $p(z)$ (the ground truth field) for $p2(z)$. Noting that we can write the fields as

$$p(z) = \sum_m W_m \psi_m(z)$$

$$\tilde{p}(z) = \sum_m W_m \psi_m(z)\theta_m, \tag{3.6}$$

where the θ_m are the obliquity factors, we substitute into the second part of Eq. 3.5 and obtain

$$\frac{\left|\int \left(\sum_m \theta_m A_m \psi_m(z)\right)\left(\sum_m A_m^* \psi_m^*(z)\right)dz\right|^2}{\int \left|\sum_m \theta_m A_m \psi_m(z)\right|^2 dz \times \int \left|\sum_m A_m \psi_m(z)\right|^2 dz}. \tag{3.7}$$

Interchanging the order of summation and integration in the numerator and expanding the magnitude squared operators while interchanging the order of summation and integration in the denominator results in

$$\frac{\left|\sum_m \sum_n \theta_m A_m A_n^* \int \psi_m(z)\psi_n^*(z)dz\right|^2}{\sum_m \sum_n \theta_m \theta_n^* A_m A_n^* \int \psi_m(z)\psi_n^*(z)dz \times \sum_m \sum_n A_m A_n^* \int \psi_m(z)\psi_n^*(z)dz}. \tag{3.8}$$

Assuming real-valued mode functions and unity density profiles, the inner products of the mode functions become Kronecker delta functions δ_{mn} and collapse the double summations. Also assuming that only the real-valued parts of the horizontal wavenumbers are used to calculate the obliquity factors and expanding the magnitude squared operator in the numerator yields

$$\frac{\sum_m \sum_n \theta_m \theta_n |A_m|^2 |A_n|^2}{\sum_m \sum_n \theta_m^2 |A_m|^2 |A_n|^2} = \frac{\sum_m \sum_n \theta_m \theta_n X_{m,n}}{\sum_m \sum_n \theta_m^2 X_{m,n}}, \tag{3.9}$$

where $X_{m,n} = |A_m|^2 |A_n|^2$.

In order to simplify the expression, we will now use the approximation that the values $X_{m,n}$ are a constant for all combinations of m and n. This approximation is somewhat justified for the following two reasons. One is that the phase of the A_m's has been canceled due to the magnitude operators. The other is that we have tended to examine average matching coefficients for a grid of source locations in a given region. This tends to average out the effects seen because some modes are excited to different extents due to the placement of the source in depth. Further ramifications of this assumption will be discussed shortly. Simplifying Eq. 3.9 with the assumption just stated gives us

$$\Upsilon_\theta = \frac{\left(\sum_m \theta_m\right)^2}{M \sum_m \theta_m^2}, \tag{3.10}$$

where M is the number of modes and we will call Υ_θ an "obliquity characterization number." Ideally this measure would give us the expected matching coefficient for a given environment. Note that if all the θ_m's are equal to one, effectively giving us a perfect

Table 3.3. Matching Coefficients vs. Obliquity Characterization Numbers.

Example #	Obliquity Characterization Number (Υ_θ)	Matching Coefficient ($|K|^2$)
3C	0.999	0.986
3A	0.997	0.984
3D	0.994	0.979
3E	0.983	0.966
3B	0.965	0.944

extrapolation, that Υ_θ is also equal to one which is the maximum value of the matching coefficient.

We will now experimentally explore the relationship between the obliquity characterization number and the matching coefficient. Note that we are still assuming perfect knowledge of the environmental parameters, as reflected in our modeled fields. In addition to the two examples already run, three more environmental scenarios were devised in order to vary the obliquity characterization number (as well as the matching coefficient). Examples 3C, 3D, and 3E utilized the same general geometry as Exs. 3A and 3B, but the constant sound speed was changed to 1465 m/s, 1535 m/s, and 1560 m/s, respectively. Table 3.3 contains the obliquity characterization numbers and average matching coefficients for all the examples. Note that the table entries are listed in order of decreasing Υ_θ. Notice the consistent decreasing nature of the matching coefficient as the obliquity characterization number decreases.

Figure 3.9 shows the data points from Table 3.3 along with a least-squares linear fit. The equation for this least-squares fit is

$$|K|^2 \cong 1.236\Upsilon_\theta - 0.248 . \tag{3.11}$$
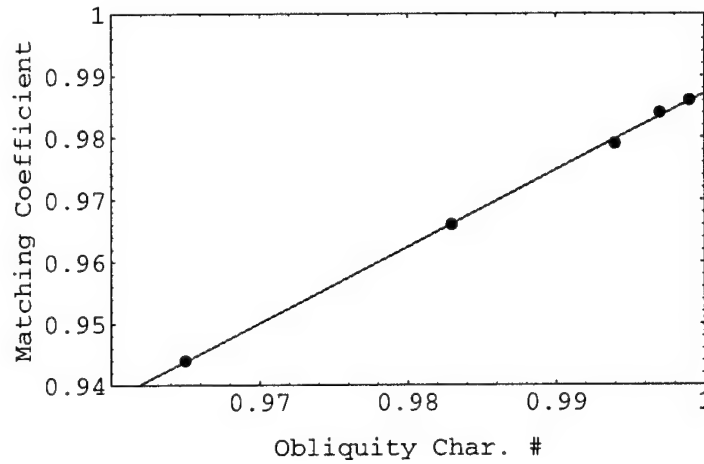
Figure 3.9. Matching Coeff. vs. Obliquity Char. Number and Linear Fit.

As can be seen from examination of Fig. 3.9, the linear fit is an excellent one to the data points. Note that extrapolating the quadratic fit out to an obliquity characterization number of one results in a matching coefficient of approximately only 0.988. Also, the ideal slope of the linear fit should be one.

The fact that the extrapolated line does not produce a matching coefficient of one for an obliquity characterization number of one can be explained by the numerical integration method used to do the extrapolation. This will be explored in Ch. 5, and the relationship between Υ_θ and $|K|^2$ will be revisited there. The variation of the slope of the linear fit from one is due to the assumption that the values of $X_{m,n}$ were constant for all m and n. These values are, in fact, not constant and tend to decrease as m and n increase due to the $\xi_m^{-1/2}$ factor in the representation of the pressure field. This consistent nonuniformity of the $X_{m,n}$'s is then the cause of the steeper slope in the fitted line. This effect could be incorporated into a new obliquity characterization number calculation, but this would involve a double summation in the denominator and would be less intuitive to analyze. As it is, the simply stated expression for the obliquity characterization number gives a good relative measure of how the matching coefficient in an extrapolation is

affected by the obliquity factors.

3.5. Obliquity Factor Effects: Attenuating Sediment Layer (Example 3F)

A common situation for shallow water acoustic propagation is to have an attenuating sediment layer beneath the water column, as opposed to the rigid boundary that has been assumed for the previous examples. We will use the environmental parameters depicted in Fig. 3.10. The sediment parameters were determined from experimental data taken from a deep ocean basin off the west coast of Vancouver Island, B.C., and are representative of a sediment with a "clayey-silt" composition [Dosso and Chapman]. The somewhat arbitrary negative gradient in the water column's sound speed profile produces a downward refracting effect on the sound traveling through the water, in effect "forcing" the sound into more interaction with the sediment.

The array geometry for Ex. 3F will be similar to that for Exs. 3A and 3B in that the calibration range will be $r_{cal} = 20$ km, and the arrays will be populated with ideal point sources with spacing $\Delta z_t = \Delta z_r = 1$ m.

3.5.1. Modal Structure

Using a source frequency of 300 Hz, KRAKEN calculates 52 propagating modes for the scenario depicted in Fig. 3.10. Table 3.4 contains a subset of the horizontal wavenumbers (eigenvalues) and associated approximate grazing angles for this scenario. Since attenuation due to material absorption can be dealt with by allowing the sound speed [Jensen *et al.*], or, equivalently, the wavenumber [Boyles], to become complex, the eigenvalues for this scenario are complex.

The mode functions corresponding to the eigenvalues listed in Table 3.4 are shown in Fig. 3.11. Note that the sediment layer begins at a depth of 150 m, and that significant extension of the mode functions into the sediment begins somewhere between modes 15 and 22.
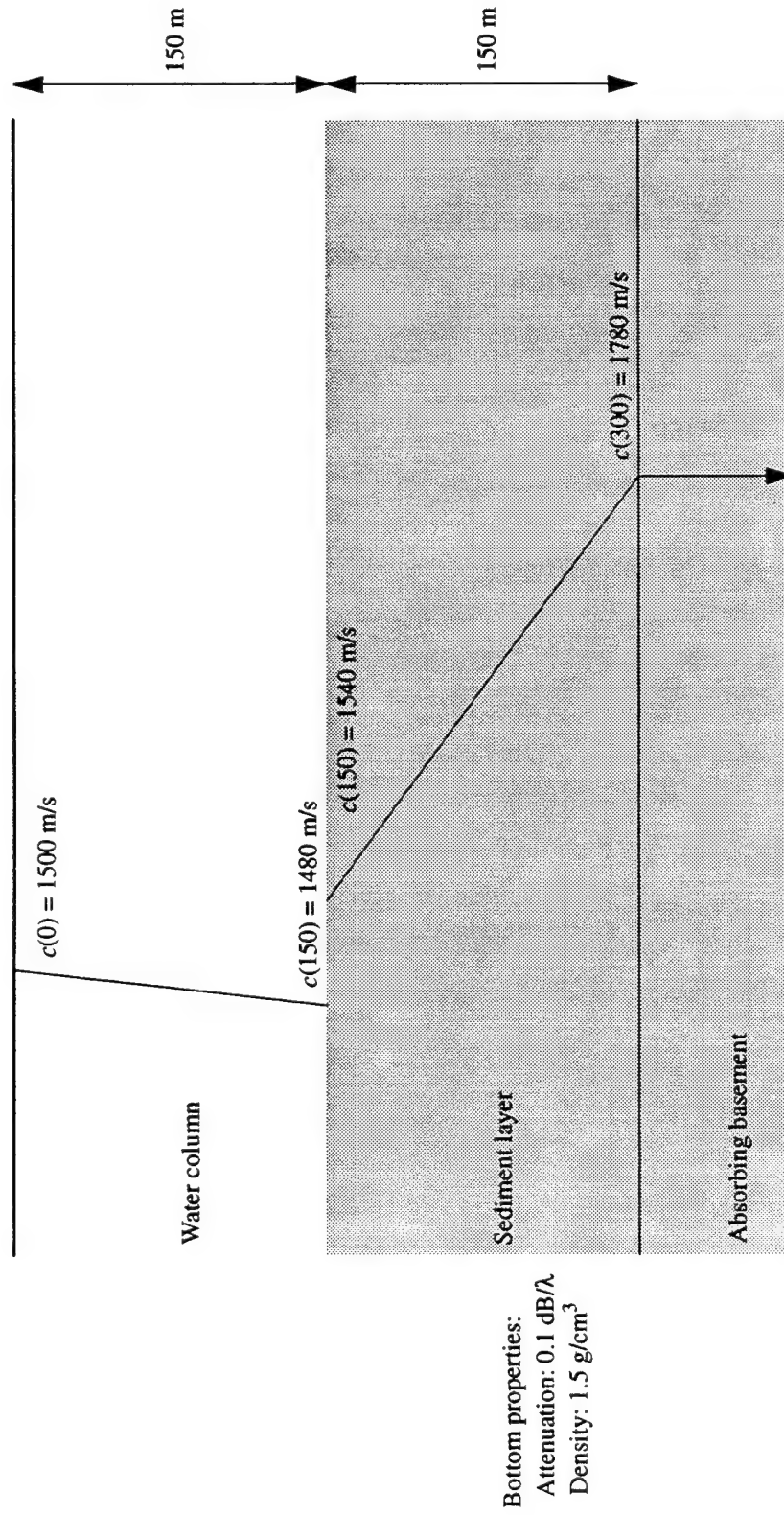
Figure 3.10. Environment with attenuating sedimentary layer.

150 m

150 m

$c(0) = 1500$ m/s

Water column

$c(150) = 1480$ m/s

$c(150) = 1540$ m/s

$c(300) = 1780$ m/s

Sediment layer

Absorbing basement

Bottom properties:
Attenuation: 0.1 dB/λ
Density: 1.5 g/cm^3

Table 3.4. Eigenvalues for Ex. 3F.

Mode # (m)	Eigenvalue (ξ_m)	Grazing Angle (χ_m) (deg.)
2	$1.267 + i\,9.201\text{x}10^{-6}$	5.8
4	$1.262 + i\,8.846\text{x}10^{-6}$	7.6
6	$1.259 + i\,9.218\text{x}10^{-6}$	8.8
8	$1.254 + i\,1.338\text{x}10^{-5}$	10.0
10	$1.248 + i\,1.967\text{x}10^{-5}$	11.4
15	$1.228 + i\,5.303\text{x}10^{-5}$	15.5
22	$1.193 + i\,1.306\text{x}10^{-3}$	20.5
29	$1.162 + i\,1.440\text{x}10^{-3}$	24.2
36	$1.131 + i\,1.563\text{x}10^{-3}$	27.4
43	$1.101 + i\,1.466\text{x}10^{-3}$	30.2

Referring back to the normal mode equation governing range-independent propagation (Eq. 1.10), we see that the contribution of each mode to the acoustic pressure at a given range r is weighted by an $e^{i\xi_m r}$ term. When the eigenvalues are complex, i.e., $\xi_m = a_m + ib_m$ (b_m is defined to be a positive number), the weighting factor becomes

$$e^{i\xi_m r} = e^{i(a_m + ib_m)r} = e^{ia_m r}e^{-b_m r} = \alpha(r)e^{ia_m r}, \qquad (3.12)$$

where $\alpha(r)$ is a multiplicative factor that decreases with increasing range, i.e., the attenuation due to this factor increases with range. Also, this factor decreases as b_m increases. In Table 3.4, we see that the imaginary part of the eigenvalues increases by roughly two orders of magnitude somewhere between mode numbers 15 and 22. This makes intuitive sense in that this is also the region where the mode functions begin to extend into the sediment, i.e., modes that interact more with the sediment are more
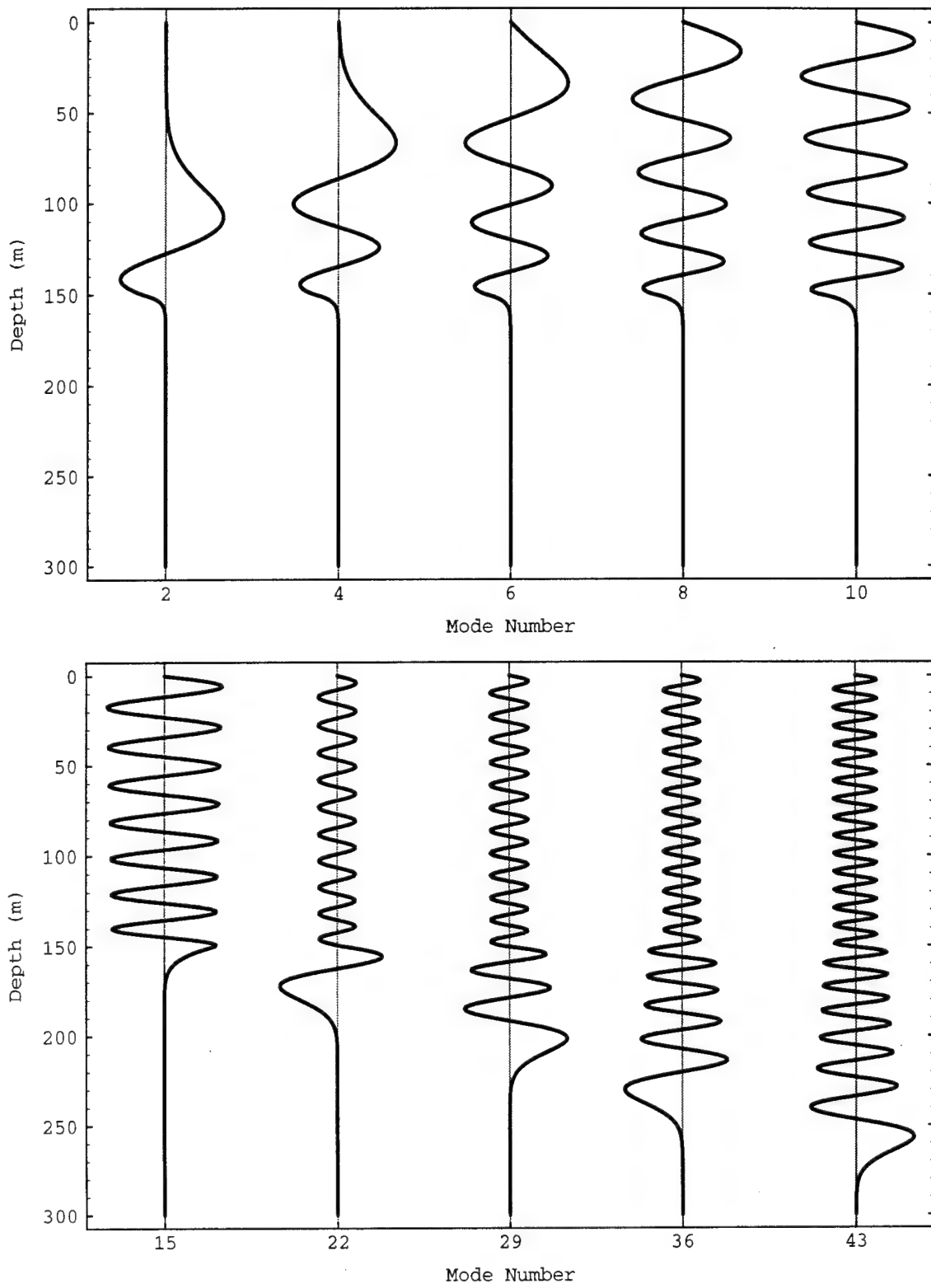
Figure 3.11. Mode functions for Ex. 3F.
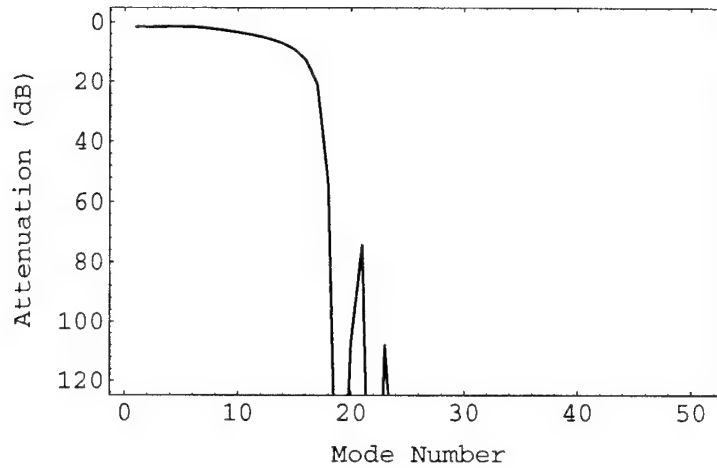
Figure 3.12. Attenuation at 20 km due to imaginary parts of eigenvalues (sediment).

severely attenuated in range. Figure 3.12 shows the attenuation due solely to the imaginary parts of the eigenvalues in this scenario at a range of 20 km. We see attenuations of greater than 60 dB for all modes after number 18, and attenuations greater than 120 dB for all modes after number 24.

Keeping these issues in mind, Fig. 3.13 shows a transmission loss plot for our sediment interaction scenario. Note the high loss in the sediment (greater than 90 dB) for ranges greater than 5 km. The modes that have the most penetration into the sediment have been "stripped" by this point in range, and the modes that have little or no penetration into the sediment continue to propagate (there is some incidental acoustic energy propagating in the sediment for ranges > 5 km).

3.5.2. Averaged Extrapolation

We can now examine what effect mode stripping by the sediment layer has on the acoustic field extrapolation algorithm. As was seen in Ex. 3B, the existence of very steeply propagating modes (leading to extreme obliquity factors) caused a degradation of the extrapolation algorithm. One would expect, then, that the elimination of steeply propagating modes would aid the extrapolation algorithm, and this is indeed the case.
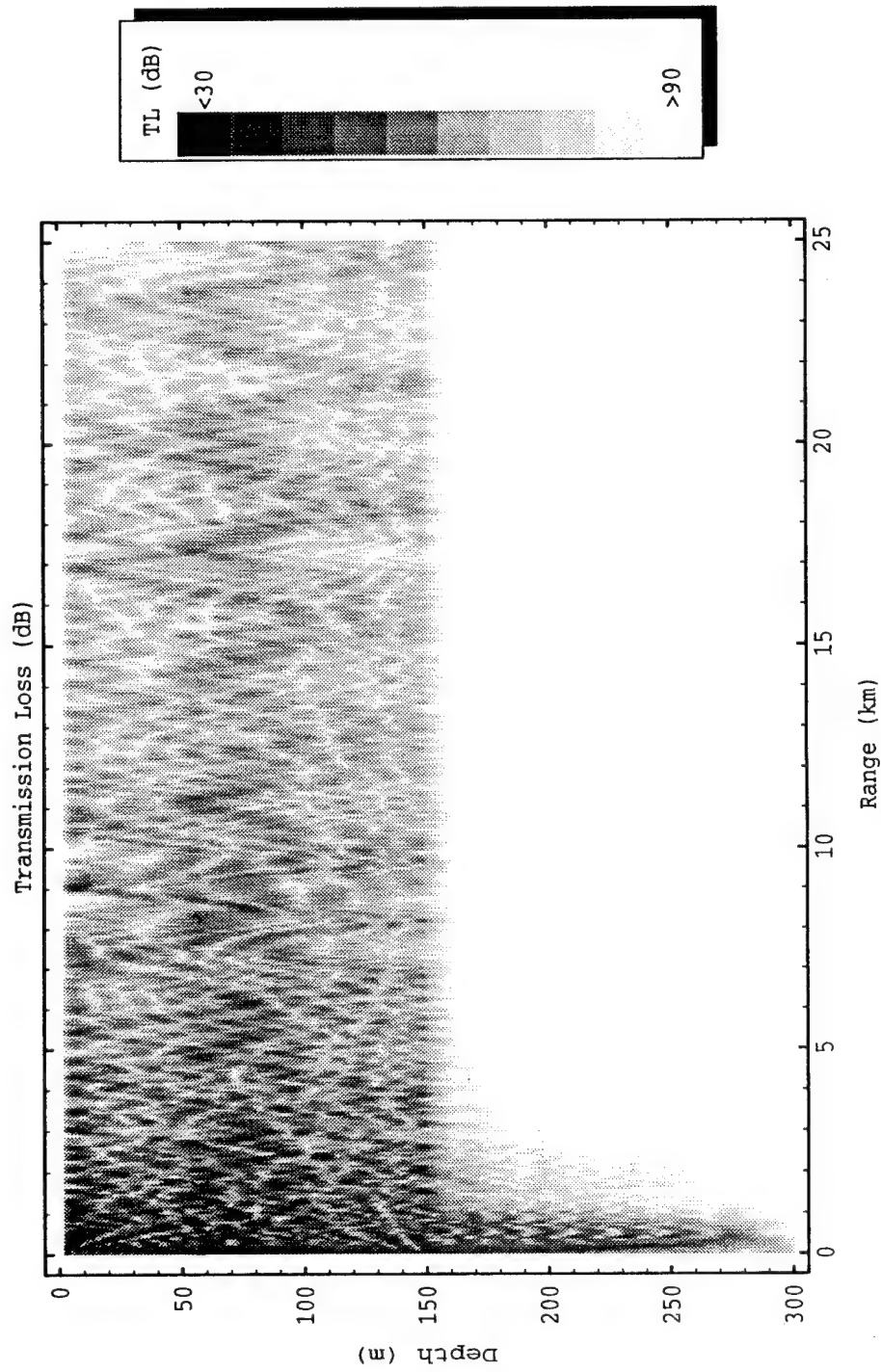
Figure 3.13. Transmission loss for Ex. 3F.

In order to find a representative matching coefficient for this scenario, source positions were varied over a grid of ranges from 1 km to 5 km spaced at 1 km and depths from 15 m to 135 m spaced at 15 m. The average value of the matching coefficient over this grid of source locations was approximately 0.996 with a variance of 1.764×10^{-5}. Figure 3.14 shows the averaged extrapolation results for a hypothetical source location $(r_{e1}, z_s) = (5 \text{ km}, 30 \text{ m})$. The matching coefficient is approximately 0.996. The primary and alternate extrapolations are not shown because the obliquity factors have a negligible effect, making the results of these two extrapolations nearly identical.

3.5.3. Obliquity Characterization of the Medium

Example 3F is significantly different from Examples 3A and 3B in that not all of the calculated propagating modes contribute significantly to the fields at the receiving array. Based on Fig. 3.12, it seems reasonable to assume that the first 18 modes contribute the bulk of the acoustic energy to the field measured along the receiving array, so we will use only these modes in the calculation of the obliquity characterization number, which turns out to be approximately 1.0. This is the expected result due to the shallow grazing angles of the propagating modes, resulting in obliquity factors very close to one. This in turn helps to explain the high matching coefficient between the ground truth and extrapolated fields of Ex. 3F.

Also note that there is not as great a discrepancy between the predicted matching coefficient for an obliquity characterization number of one. In Sec. 3.4, the linear fit was extrapolated to a value of $|K|^2 = 0.988$ for $\Upsilon_\theta = 1$, whereas in this example an actual value of 0.996 was obtained for $\Upsilon_\theta = 1$. This can again be explained by the numerical integration method used, and will be revisited in Ch. 5.

3.6. Summary of Chapter 3

Chapter 3 was intended mainly as an illustration through numerical modeling of

67
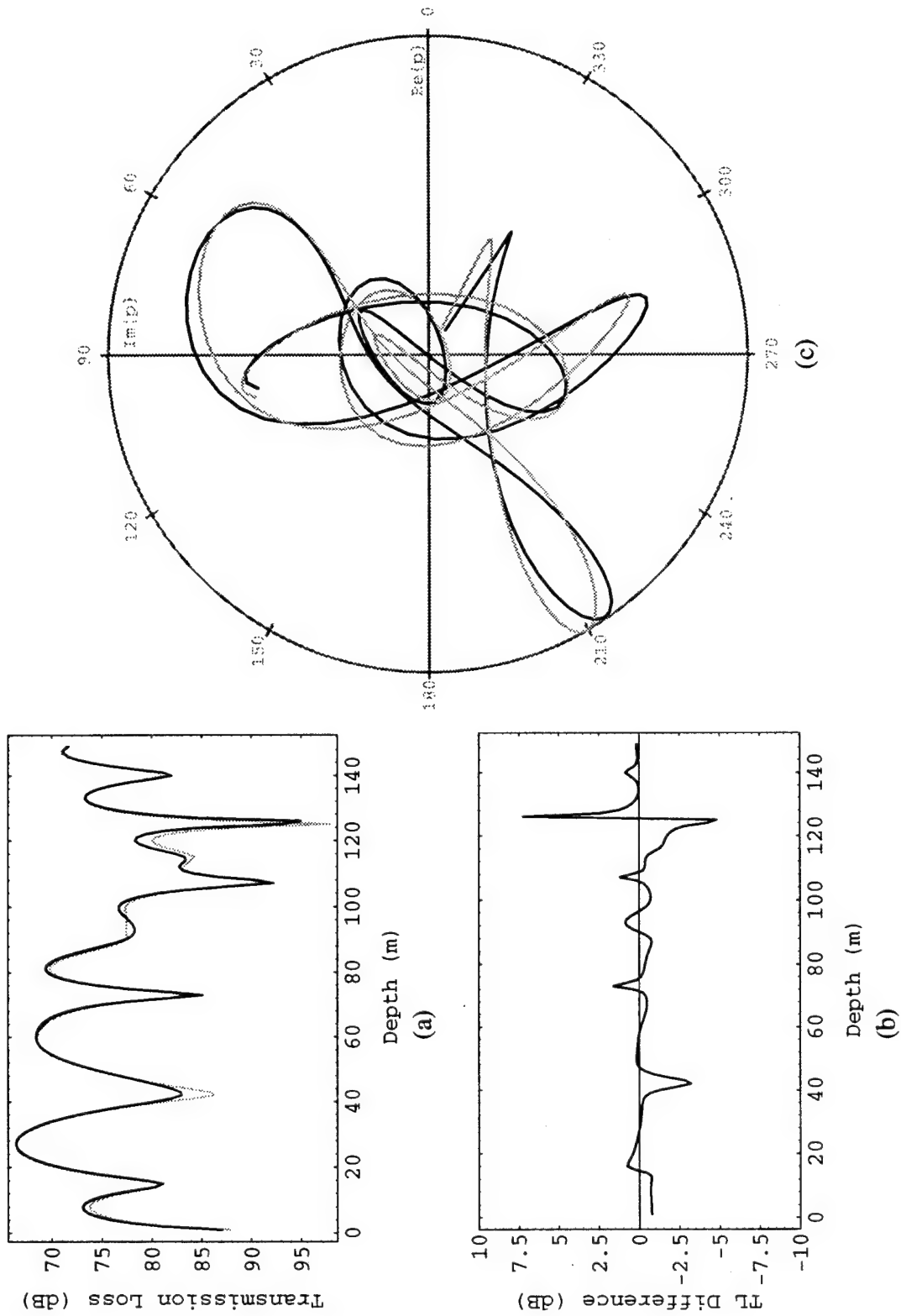
Figure 3.14. Ex. 3F: Averaged field extrapolation.

the mathematical relationships explored in Ch. 2. Through qualitative comparisons it was seen how the overemphasis of the individual modes in the primary extrapolation and underemphasis in the alternate extrapolation lead to distinctly different types of distortions in the extrapolated fields. It was also seen how averaging these two estimates ameliorates these effects and produces a better approximation of the ground truth field. It was shown how a quantitative comparison of the extrapolated and ground truth fields can be made through use of the matching coefficient, and how approximations of the obliquity factors for each mode in a given environmental scenario can give an approximation to the expected matching coefficient.

Chapter 4 will examine the effects of inaccurate knowledge of the environmental parameters used to produce the modeled fields on the extrapolation algorithm.

Chapter 4: Acoustic Field Extrapolation - Modeled Field Mismatch

4.1. Introduction to Chapter 4

The examples given in Ch. 3 assumed perfect knowledge of the medium to be used as input to an acoustic field modeling algorithm in order to calculate $\hat{p}$. This led, then, to "exact" modeled fields (in the sense that they reflect what the actual fields would look like along the reference array), and extrapolated fields that are affected only by the extrapolation algorithm itself. These effects were seen to be modal dependent obliquity factors, which became more severe for more steeply propagating energy.

We will now examine the effects of using erroneous environmental information in the modeling step, leading to a situation we will refer to as "environmental mismatch." The erroneous environmental information results in modeled fields that do not accurately reflect what the actual field would look like along the reference array, and therefore degrade the extrapolation results. Numerous studies of the effect of mismatch on matched-field processing algorithms have been done (see references in [Baggeroer *et al.*], as well as [Gingras]). This chapter will examine the effect of mismatch due to errors in the sound speed profile of the water column as well as errors in sediment parameters.

This chapter will take a "perturbational" approach to the problem, i.e., for a small perturbation in the water column sound speed profile, what is the change in the expression for the modeled—and subsequently the extrapolated—field? This will be accomplished with the normal mode theory used throughout this work. First an existing derivation from the field of quantum mechanics will be presented that shows how an equation like the modal equation can be treated perturbationally. This result will then be translated into the underwater acoustic modal equation form in order to show the changes in the horizontal wavenumbers and mode functions due to perturbations in the sound speed profile in the water column. A "zero-order" acoustic waveguide scenario will be used to determine

some general characteristics of the first-order perturbations. The perturbations will be integrated into the field extrapolation expressions, and examples of errors in the water column sound speed profile as well as the sediment properties will be given and their effects on the algorithm shown.

4.2. Quantum Mechanical Perturbation Theory

In quantum mechanics, the time-independent Schrödinger equation has a form very similar to our modal equation for underwater sound propagation. The consequences of perturbing the "energy operator" in quantum mechanics are well known, and can serve as a guide in doing a similar operation with the modal equation. The following first-order perturbation derivation follows the order and notation found in [Yariv]. A parallel development can be found in [Schiff].

The time-independent Schrödinger equation is given as

$$\hat{H}_0 u_m = E_m u_m,$$ (4.1)

where the u_m are the wavefunctions (eigenfunctions) for a given state, and the E_m are the energies (eigenvalues) for that state. $\hat{H}_0$ is the energy operator, or Hamiltonian (the exact form of the Hamiltonian is not of immediate relevance here). The problem posed is thus: if the Hamiltonian is perturbed from $\hat{H}_0$ to $\hat{H}_0 + \hat{H}'$, what are the new eigenfunctions and eigenvalues? Assuming $\hat{H}_0 \gg \hat{H}'$, we can use the following approach.

We set the perturbed Hamiltonian to be $\hat{H}_0 + \lambda \hat{H}'$, where λ is simply a parameter that is set to one where a perturbation is desired and set to zero where it is not. For the final results, λ will be set to one. We are now looking for the eigenvalues W and eigenfunctions Ψ that satisfy

$$(\hat{H}_0 + \lambda \hat{H}') \Psi = W \Psi.$$ (4.2)

Expanding W and Ψ in power series in λ, i.e.,

$$\Psi = \Psi_0 + \lambda\Psi_1 + \lambda^2\Psi_2 + \dots$$

$$W = W_0 + \lambda W_1 + \lambda^2 W_2 + \dots, \tag{4.3}$$

and substituting these expansions back into Eq. 4.2, we obtain

$$(\hat{H}_0 + \lambda\hat{H}') \, (\Psi_0 + \lambda\Psi_1 + \lambda^2\Psi_2 + \dots) = (W_0 + \lambda W_1 + \lambda^2 W_2 + \dots) \times$$
$$(\Psi_0 + \lambda\Psi_1 + \lambda^2\Psi_2 + \dots). \tag{4.4}$$

Now we can equate like powers of λ on both sides of Eq. 4.4, giving

$$\hat{H}_0\Psi_0 = W_0\Psi_0$$

$$\hat{H}_0\Psi_1 + \hat{H}'\Psi_0 = W_0\Psi_1 + W_1\Psi_0 \tag{4.5}$$

and so on. Comparing the first line of Eq. 4.5 with Eq. 4.1, we see that the zero-order solutions are

$$\Psi_0 = u_m$$

$$W_0 = E_m, \tag{4.6}$$

or the unperturbed eigenfunctions and eigenvalues.

To determine the first order perturbations to the eigenfunctions and eigenvalues, Ψ_1 and W_1 respectively, we first expand Ψ_1 in terms of the u_n as

$$\Psi_1 = \sum_n a_n^{(1)} u_n, \tag{4.7}$$

where the $a_n^{(1)}$ are coefficients for the first-order perturbation. Noting that E_m can be substituted for $\hat{H}_0$ (see Eq. 4.1) and using Eq. 4.7, the second line of Eq. 4.5 (λ^1, first-order perturbation) can now be written

$$\sum_n a_n^{(1)} E_n u_n + \hat{H}' u_m = E_m \sum_n a_n^{(1)} u_n + W_1 u_m. \qquad (4.8)$$

The eigenfunctions here take on an orthonormality property similar to the mode functions for the underwater acoustic propagation formulas, i.e.,

$$\int u_m^* u_n = \delta_{mn}, \qquad (4.9)$$

where the * denotes conjugation and δ_{mn} is a Kronecker delta function. Taking advantage of this, we premultiply Eq. 4.8 by u_k^* and integrate, resulting in

$$E_k a_k^{(1)} + (u_k^*, \hat{H}' u_m) = E_m a_k^{(1)} + W_1 \delta_{km}, \qquad (4.10)$$

where (a, b) denotes an inner product of a and b. Letting $k = m$ in Eq. 4.10 yields

$$W_1 = (u_m, \hat{H}' u_m), \qquad (4.11)$$

giving us the first order correction for the energy E_m. For $k \neq m$, we find that

$$a_k^{(1)} = \frac{(u_k, \hat{H}' u_m)}{E_m - E_k}, \quad k \neq m. \qquad (4.12)$$

It can be shown [Yariv] that $a_m^{(1)} = 0$, so the complete first-order perturbational expressions for the eigenfunctions and eigenvalues are given by

$$\Psi = u_m + \sum_{k \neq m} \frac{(u_k, \hat{H}' u_m)}{E_m - E_k} u_k$$

$$W = E_m + (u_k, \hat{H}' u_m) . \tag{4.13}$$

4.3. Underwater Acoustic Modal Equation Perturbation Theory

We can now apply the above results to the underwater acoustic modal equation to determine what the changes in the mode functions and horizontal wavenumbers would be for perturbations in the water column sound speed profile. Similar results are shown in [Rajan *et al.*], and we use elements of their notation here. A parallel derivation was also done in [Rouseff (Feb. 1993)].

We begin by assuming a piecewise constant density profile, and rewriting the modal equation, Eq. 1.4, as

$$\left[\frac{d^2}{dz^2} + (k^{(0)}(z))^2 \right] \psi_m^{(0)}(z) = (\xi_m^{(0)})^2 \psi_m^{(0)}(z), \tag{4.14}$$

where

$$k^{(0)}(z) = \frac{\omega}{c_0(z)} \tag{4.15}$$

is the unperturbed depth-dependent acoustic wavenumber, and $c_0(z)$ is the unperturbed sound speed profile in the water column. Comparing Eq. 4.14 with Eq. 4.1, we see that the mode functions $\psi_m^{(0)}(z)$ correspond to the quantum mechanical wavefunctions (eigenfunctions) u_m, the squared horizontal wavenumbers $(\xi_m^{(0)})^2$ correspond to the quantum mechanical energy levels (eigenvalues) E_m, and the operator term in [ ]'s corresponds to the Hamiltonian $\hat{H}_0$. We will use the same notation and terminology for this operator as was used in the quantum mechanical derivation, although the two

operators have different forms when expanded.

Since it appears explicitly in the perturbed eigenfunction and eigenvalue expression, the next task is to determine the perturbation in the Hamiltonian, $\hat{H}'$, due to a perturbation in the sound speed profile. We will denote the sound speed perturbation as $\Delta c(z)$, and assume that $\Delta c(z) \ll c_0(z)$. We now write the expression for the perturbed depth-dependent acoustic wavenumber as

$$k(z) = \frac{\omega}{c_0(z) + \Delta c(z)} = \frac{\omega(c_0(z) - \Delta c(z))}{c_0^2(z) - (\Delta c(z))^2} \cong \frac{\omega}{c_0(z)} - \frac{\omega \Delta c(z)}{c_0^2(z)}, \tag{4.16}$$

assuming terms of $(\Delta c(z))^2$ are negligible. We then find that

$$k^2(z) \cong \frac{\omega^2}{c_0^2(z)} - \frac{2\omega^2 \Delta c(z)}{c_0^3(z)} + \frac{\omega^2 (\Delta c(z))^2}{c_0^4(z)} \cong (k^{(0)}(z))^2 - 2(k^{(0)}(z))^2 \frac{\Delta c(z)}{c_0(z)}, \tag{4.17}$$

again neglecting terms of $(\Delta c(z))^2$. Inserting this into the expression for the Hamiltonian, we see that

$$\hat{H}_0 + \hat{H}' = \frac{d^2}{dz^2} + k^2(z) = \frac{d^2}{dz^2} + (k^{(0)}(z))^2 - 2(k^{(0)}(z))^2 \frac{\Delta c(z)}{c_0(z)}. \tag{4.18}$$

Comparing this to Eq. 4.14, we can see that the perturbation in the Hamiltonian is

$$\hat{H}' = -2(k^{(0)}(z))^2 \frac{\Delta c(z)}{c_0(z)}. \tag{4.19}$$

Note also from Eq. 4.14 that the energies (eigenvalues) of the quantum mechanical expression are the counterpart of the square of the horizontal wavenumbers for the underwater acoustic modal equation. We can say that

$$\Delta\xi_m^2 = \xi_m^2 - (\xi_m^{(0)})^2 \cong (\xi_m^{(0)} + \Delta\xi_m^{(1)})^2 - (\xi_m^{(0)})^2$$

$$= (\xi_m^{(0)})^2 + 2\xi_m^{(0)}\Delta\xi_m^{(1)} + (\Delta\xi_m^{(1)})^2 - (\xi_m^{(0)})^2$$

$$\cong 2\xi_m^{(0)}\Delta\xi_m^{(1)} \tag{4.20}$$

neglecting terms of $(\Delta\xi_m^{(1)})^2$, and consequently

$$\Delta\xi_m^{(1)} = \frac{\Delta\xi_m^2}{2\xi_m^{(0)}}. \tag{4.21}$$

Translating the quantum mechanical perturbation results (Eq. 4.10), we see to first order that

$$\Delta\xi_m^2 = (\psi_m^{(0)}(z), \hat{H}'\psi_m^{(0)}(z)). \tag{4.22}$$

Keeping in mind that the inner product orthonormality condition for the modal equation involves a weighting by the inverse of the density profile (see Eq. 1.6), we can combine Eqs. 4.21 and 4.22 to determine the first order perturbation expression for the horizontal wavenumbers and write it as

$$\Delta\xi_m^{(1)} = \frac{-1}{\xi_m^{(0)}}\int_0^\infty \rho^{-1}(z')(\psi_m^{(0)}(z'))^2(k^{(0)}(z'))^2 \frac{\Delta c(z')}{c_0(z')}dz'. \tag{4.23}$$

Translating the proper quantum mechanical results, we can also write the expression for the perturbation in the mode functions as

$$\Delta\psi_m^{(1)}(z) = \sum_n a_n^{(1)}\psi_n^{(0)}(z), \tag{4.24}$$

where

$$
a_n^{(1)} = \left\{ \begin{array}{cc} \dfrac{(\psi_n^{(0)}(z), \hat{H}'\psi_m^{(0)}(z))}{(\xi_m^{(0)})^2 - (\xi_n^{(0)})^2} & , \quad n \neq m \\ \\ 0 & , \quad n = m. \end{array} \right. \tag{4.25}
$$

Substituting in the proper expressions results in

$$
\Delta\psi_m^{(1)}(z) = \sum_{n \neq m} \frac{-2\psi_n(z)\left(\displaystyle\int_0^\infty \rho^{-1}(z')\psi_n^{(0)}(z')\psi_m^{(0)}(z')(k^{(0)}(z'))^2 \frac{\Delta c(z')}{c_0(z')}dz' \right)}{(\xi_m^{(0)})^2 - (\xi_n^{(0)})^2} . \tag{4.26}
$$

4.4. Discussion of Perturbation Results

We will now examine some of the implications of the above perturbation results. We will use a "zero-order" acoustic waveguide case in order to gain some insight into how perturbations in the sound speed profile affect the horizontal wavenumbers and mode functions. Both constant offsets and random fluctuations will be examined.

4.4.1. Constant Offset

Examples 3A and 4A will serve as our "zero-order" acoustic waveguide examples. In Ex. 3A we had an idealized ocean with a pressure release surface and a perfectly rigid bottom at a depth of $h = 50$ m, and we used a constant sound speed profile in the water column of 1500 m/s. Note that the mode functions and horizontal wavenumbers can be calculated analytically for this case (see Eq. 3.1). Example 4A will use a similar scenario with a constant sound speed of 1510 m/s.

We can examine our first-order perturbational results in order to see what the effects of perturbing the sound speed profile (as in going from Ex. 3A to Ex. 4A) on the horizontal wavenumbers and mode functions should be. Examining Eq. 4.23, we realize

that the density, depth-dependent wavenumber, and sound speeds (both the $\Delta c(z)$ and the $c_0(z)$) are constants with depth which can be pulled out of the integral. Taking the orthonormality condition into account, we see that the perturbation in each horizontal wavenumber should be

$$\Delta \xi_m^{(1)} \approx \frac{-A}{\xi_m^{(0)}}, \qquad (4.27)$$

where A is a constant for all m (A is positive for $\Delta c(z) > 0$). In other words, the change in each horizontal wavenumber is a constant divided by the unperturbed horizontal wavenumber. Since the eigenvalues are ordered such that $\xi_m^{(0)} > \xi_{m+1}^{(0)}$, the perturbations should be greater as m increases. This is borne out in Table 4.1 which lists the horizontal wavenumbers (to four decimal places) for Examples 3A and 4A along with their differences. The perturbations do indeed grow as m increases.

Using the first mode in order to get an estimate of the constant A (without rounding the KRAKEN output), we see that

$$A \approx -\Delta \xi_1^{(1)} \xi_1^{(0)} \cong 2.61449 \times 10^{-3}. \qquad (4.28)$$

Using this to predict what $\Delta \xi_{10}^{(1)}$ should be, we arrive at an approximate value of -0.0133. Keeping in mind that this is a first order approximation, it is quite close to the actual value of -0.0138.

We can do a similar simplification for the mode function perturbations of Eq. 4.26. This time, however, when the constant terms are pulled outside the integral, we are left with inner products of orthogonal components (since the sum is over all $n \neq m$), and the result is that $\Delta \psi_m^{(1)}(z) = 0$. This coincides with the result from Ch. 3 where it was seen that the mode functions are indeed the same for simple constant offsets of the sound speed

Table 4.1. Eigenvalue Comparison for Ex. 4A.

Mode # (m)	Example 3A	Example 4A	Difference
1	.6275	.6234	-.0041
2	.6212	.6170	-.0042
3	.6084	.6041	-.0043
4	.5886	.5841	-.0045
5	.5611	.5564	-.0047
6	.5247	.5198	-.0049
7	.4775	.4720	-.0055
8	.4156	.4093	-.0063
9	.3310	.3230	-.0080
10	.1962	.1824	-.0138

for environments of this type.

4.4.2. Random Fluctuations

We will now examine the situation where the perturbation to the sound speed is a random process. Specifically, $\Delta c(z)$ will be a wide-sense stationary zero-mean white Gaussian process with variance σ^2. For this case, we can write the first-order perturbations to the horizontal wavenumbers as

$$\Delta \xi_m^{(1)} = \frac{-A'}{\xi_m^{(0)}} \int_0^h \left(\psi_m^{(0)}(z') \right)^2 \Delta c(z') dz'. \tag{4.29}$$

Taking the expected value [Papoulis] of this expression yields

$$E\{\Delta\xi_m^{(1)}\} = E\left\{\frac{-A'}{\xi_m^{(0)}}\int_0^h (\psi_m^{(0)}(z'))^2 \Delta c(z')dz'\right\} = \frac{-A'}{\xi_m^{(0)}}\int_0^h (\psi_m^{(0)}(z'))^2 E\{\Delta c(z')\}\,dz'$$

$$= 0 \qquad\qquad (4.30)$$

since $\Delta c(z)$ is zero-mean.

We can also calculate the variance of the perturbations of the horizontal wavenumbers as

$$Var\{\Delta\xi_m^{(1)}\} = E\{(\Delta\xi_m^{(1)})^2\} - E\{\Delta\xi_m^{(1)}\}^2$$

$$= E\left\{\frac{A'^2}{(\xi_m^{(0)})^2}\int_0^h\int_0^h (\psi_m^{(0)}(z'))^2 (\psi_m^{(0)}(z''))^2 \Delta c(z')\Delta c(z'')dz'dz''\right\} \qquad (4.31)$$

since we have seen that the mean value is zero. Taking the expectation operator inside the integral and simplifying due to our definition of the sound speed perturbations results in

$$Var\{\Delta\xi_m^{(1)}\} = \frac{A'^2}{(\xi_m^{(0)})^2}\int_0^h\int_0^h (\psi_m^{(0)}(z'))^2 (\psi_m^{(0)}(z''))^2 E\{\Delta c(z')\Delta c(z'')\}\,dz'dz''$$

$$= \frac{A'^2}{(\xi_m^{(0)})^2}\int_0^h\int_0^h (\psi_m^{(0)}(z'))^2 (\psi_m^{(0)}(z''))^2 \sigma^2\delta(z'-z'')dz'dz''. \qquad (4.32)$$

Collapsing the double integral due to the Dirac delta function $\delta(z'-z'')$ results in

$$Var\{\Delta\xi_m^{(1)}\} = \frac{\sigma^2 A'^2}{(\xi_m^{(0)})^2}\int_0^\infty (\psi_m^{(0)}(z'))^4 dz' = \frac{A''}{(\xi_m^{(0)})^2} \qquad (4.33)$$

Table 4.2. Results of Random Fluctuations on Eigenvalues.

Mode # (m)	Unperturbed $\xi_m^{(0)}$	Sample Mean	Sample Variance
1	.628	.628	5.23×10^{-9}
2	.621	.621	5.35×10^{-9}
3	.608	.608	5.76×10^{-9}
4	.589	.589	6.53×10^{-9}
5	.561	.561	6.41×10^{-9}
6	.525	.525	7.46×10^{-9}
7	.477	.477	8.86×10^{-9}
8	.416	.416	1.29×10^{-8}
9	.331	.331	1.83×10^{-8}
10	.196	.196	5.45×10^{-8}

since it can be shown that the integral of the mode functions to the fourth power is a constant for all m, given the form of the mode functions in Eq. 3.1.

While the mean of the perturbations of the horizontal wavenumbers is zero for all modes, the variance grows proportionally to the inverse of the square of the unperturbed horizontal wavenumbers. A Monte Carlo experiment was run using KRAKEN to calculate the horizontal wavenumbers for realizations of perturbed sound speed profiles. Realizations of $\Delta c(z)$ (spacing in z was 1 m) with $\sigma^2 = 1$ m/s were added to a constant sound speed profile of 1500 m/s (i.e., perturbing the environmental parameters of Example 1). The results over 500 realizations are listed in Table 4.2. Note that the sample means match the unperturbed horizontal wavenumbers for all modes, and the variances show a more-or-less consistent increase with m (there is an anomaly at $m = 5$).

Doing a similar operation as was done for determining the constant A, we can use

the results from the first mode to determine A'':

$$A'' \approx Var\{\Delta\xi_1^{(1)}\} \; (\xi_1^{(0)})^2 \cong 2.06 \times 10^{-9}. \tag{4.34}$$

Using this to predict what the variance should be for the tenth mode results in a value of 5.37×10^{-8}, which compares very favorably with the actual value of 5.45×10^{-8}. Again we see the trend in which the higher order modes are affected to a greater degree by perturbations in the sound speed profile. The expression for the variance of the $\Delta\psi_m^{(1)}(z)$ is easily derivable, but is of little use for gaining insight into how the modes are affected by the sound speed fluctuations.

It is important to note that the results in this section (4.4) apply only to the special "zero-order" acoustic waveguide case, whereas the general results from Sec. 4.3 apply to any environmental scenario that satisfies the assumptions stated there. By making the background sound speed constant with depth, we were able to move terms based on it outside the depth integral, and some illustrative analytical results were obtained. For other scenarios, Eqs. 4.23 and 4.26 could be numerically integrated in order to provide estimates of the changes in the horizontal wavenumbers and mode functions for a given perturbation of the sound speed.

4.5. Mismatch Effects: Water Column Sound Speed Profile (Example 4B)

This section will provide an example of the effects on the acoustic field extrapolation algorithm due to mismatch in the sound speed profile of the water column. Random fluctuations about the true sound speed profile will be considered here.

4.5.1. Environmental Parameters and Modal Structure

For this example, we will assume imperfect knowledge of the environment in the form of a mismatched sound speed profile in the water column. The "true" environmental
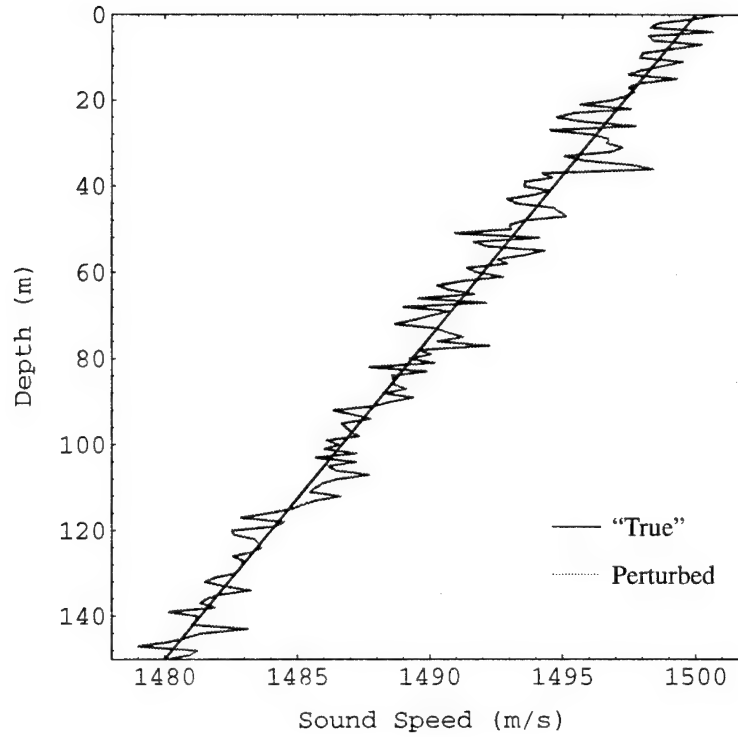
Figure 4.1. "True" and perturbed sound speed profile in water column.

conditions will be the same as those found in Sec. 3.4, i.e., an attenuating sediment layer underlying the water column. We choose this environment in order to focus attention on the effects due to mismatch instead of the obliquity factors. The "calibration" data, then, will be taken (simulated, in this case) using these conditions. The erroneous environmental conditions we will use in constructing our modeled fields will be the same as the "true" conditions except for random fluctuations $\Delta c(z)$ in the sound speed of the water column. $\Delta c(z)$ will be a wide-sense stationary zero-mean white Gaussian process with variance $\sigma^2 = 1$ m/s. A plot of the true and perturbed sound speed profiles can be seen in Fig. 4.1.

This mis-estimation of the sound speed profile leads to perturbations in the modeled mode functions and horizontal wavenumbers as was seen in the previous section. Although the mean values of the perturbations were shown to be zero, any given realization of $\Delta c(z)$ will impart a finite perturbation to the mode functions and horizontal

Table 4.3. Eigenvalue Comparison for Ex. 4B.

Mode # (m)	Eigenvalue (ξ_m)	Change in Eigenvalue
2	$1.267 + i\,9.475 \times 10^{-6}$	$-1.945 \times 10^{-4} + i\,2.739 \times 10^{-7}$
4	$1.262 + i\,7.404 \times 10^{-6}$	$1.645 \times 10^{-5} - i\,1.442 \times 10^{-6}$
6	$1.259 + i\,9.951 \times 10^{-6}$	$-6.378 \times 10^{-5} + i\,7.328 \times 10^{-7}$
8	$1.254 + i\,1.489 \times 10^{-5}$	$3.672 \times 10^{-5} + i\,1.515 \times 10^{-6}$
10	$1.248 + i\,1.988 \times 10^{-5}$	$-9.394 \times 10^{-5} + i\,2.017 \times 10^{-7}$
15	$1.228 + i\,5.270 \times 10^{-5}$	$5.519 \times 10^{-5} - i\,3.296 \times 10^{-7}$
22	$1.193 + i\,1.299 \times 10^{-3}$	$2.741 \times 10^{-6} - i\,6.843 \times 10^{-6}$
29	$1.162 + i\,1.421 \times 10^{-3}$	$-2.694 \times 10^{-5} - i\,1.908 \times 10^{-5}$
36	$1.131 + i\,1.570 \times 10^{-3}$	$-2.742 \times 10^{-6} + i\,6.573 \times 10^{-6}$
43	$1.101 + i\,1.470 \times 10^{-3}$	$-5.245 \times 10^{-6} + i\,3.560 \times 10^{-6}$

wavenumbers. Table 4.3 shows a comparison between the "true" and perturbed horizontal wavenumbers for this example. Although it is difficult to draw any general conclusions, it does appear that greater variations in the horizontal wavenumbers appear in the lower order modes.

This can be explained in the following manner. Referring back to Eq. 4.23, we see that the perturbation for a given horizontal wavenumber is expressed as an integral over the squared mode function times environmental parameters, including the sound speed perturbations. Since the $\Delta c(z)$ are zero for depths past the water/sediment boundary, the integral need only go from 0 to $h = 150$ m. Also keep in mind that due to the orthonormality condition, each mode has unit "energy" when their squares are integrated from 0 to ∞ (or in this case, to the attenuating basement at $h = 300$ m). Since higher order mode functions have increasingly more "energy" in the sediment, and, hence, less

"energy" that is encompassed by the integral of Eq. 4.23, we would expect that the lower order modes would be affected more by the water column sound speed fluctuations due to the integral part of Eq. 4.23. This effect ends up competing with the inverse weighting of the unperturbed horizontal wavenumbers, but since for this case the horizontal wavenumbers vary over a relatively small range, the integration factor wins out.

Figure 4.2 shows a plot comparing the mode functions for the "true" and perturbed cases (the perturbed modes are plotted in gray). Small errors can be observed in the first four mode functions shown, but the rest show near exact coincidence between the "true" and perturbed mode functions. Again we can appeal to our perturbation relationships. Equation 4.26 shows the first-order perturbation results for the mode functions. Note that for a given mode m, the perturbation to the mode function is a sum of integrals (again only over the water depth) over that weighted mode function times the rest of the mode functions to which it is orthogonal (the weighting skews the orthogonality). Since the higher order modes have less "energy" in the water column, we can expect that they will be perturbed less than the lower order modes which have nearly all their "energy" in the water column.

4.5.2. Extrapolation Results

An extrapolation experiment was run using the same array geometry as in Ex. 3F. Extrapolations were performed for a grid of source locations varying in range from 0.2 km to 10 km spaced at 0.2 km and in depth from 15 m to 135 m spaced at 5 m. Instead of averaging over the entire grid, the matching coefficients for a given range were averaged, yielding an average matching coefficient vs. range. The results are shown in Fig. 4.3. There is a very regular decreasing trend in the matching coefficient as range increases. The reasons for this degradation will be examined in the next subsection.

Figures 4.4, 4.5, and 4.6 show transmission loss plots and Argand diagrams for
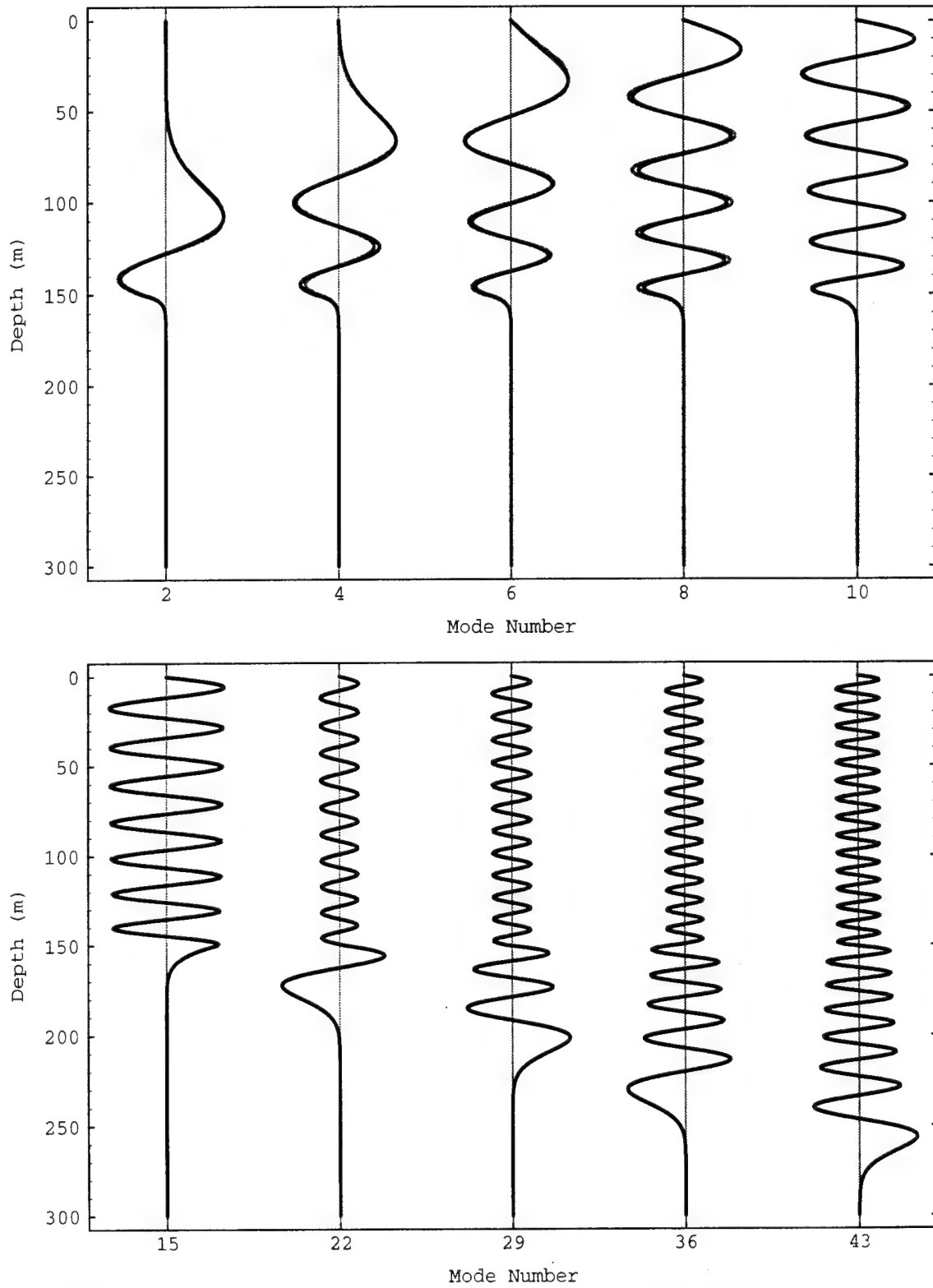
Figure 4.2. Comparison of "true" and perturbed mode functions for Ex. 4B.
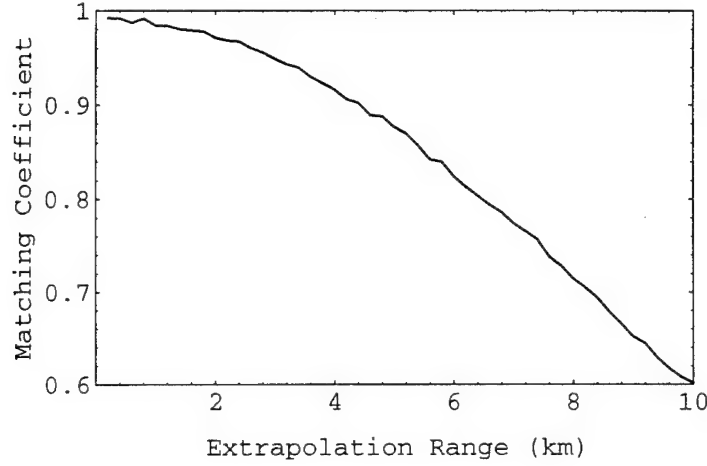
Figure 4.3. Averaged extrapolation results vs. range for Ex. 4.

three different extrapolation ranges. The matching coefficients and ranges are, respectively, 0.993 at 0.2 km, 0.948 at 3.0 km, and 0.871 at 5.0 km. As before, the specific cases shown were chosen because their matching coefficients were close to the average matching coefficient for, in this case, the given range. Notice that the matching coefficient for 0.2 km is only slightly below that for the unperturbed case (0.993 vs. 0.996). Some other interesting characteristics will be examined in the next subsection.

4.5.3. Discussion of Mismatched Extrapolation

We can analytically examine the effects of the water column sound speed profile mismatch on the extrapolation algorithm by going back to our normal mode representation for the modeled field (Eq. 2.5), and inserting terms for the perturbations:

$$\hat{p}(r_a, z_a) = \left[\frac{i}{8\pi r_a}\right]^{1/2} \frac{1}{\rho(z_0)} \sum_m (\psi_m(z_0) + \Delta\psi_m(z_0)) \; (\psi_m(z_a) + \Delta\psi_m(z_a)) \times$$

$$(\xi_m + \Delta\xi_m)^{-1/2} e^{i(\xi_m + \Delta\xi_m) r_a}. \tag{4.35}$$

Multiplying out, ignoring terms that multiply perturbations together, and expanding the
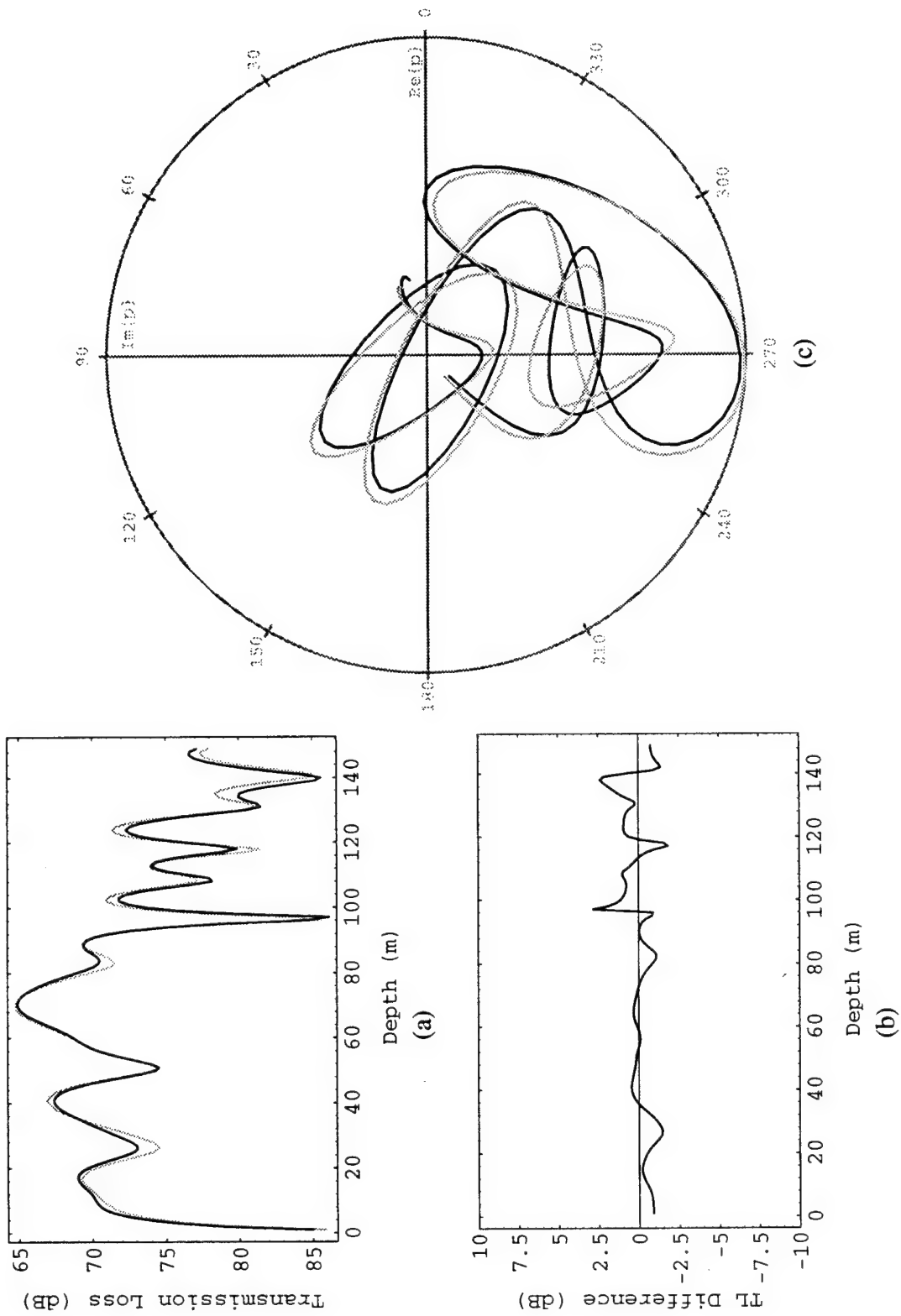
Figure 4.4. Ex. 4B: Field extrapolation at 0.2 km.
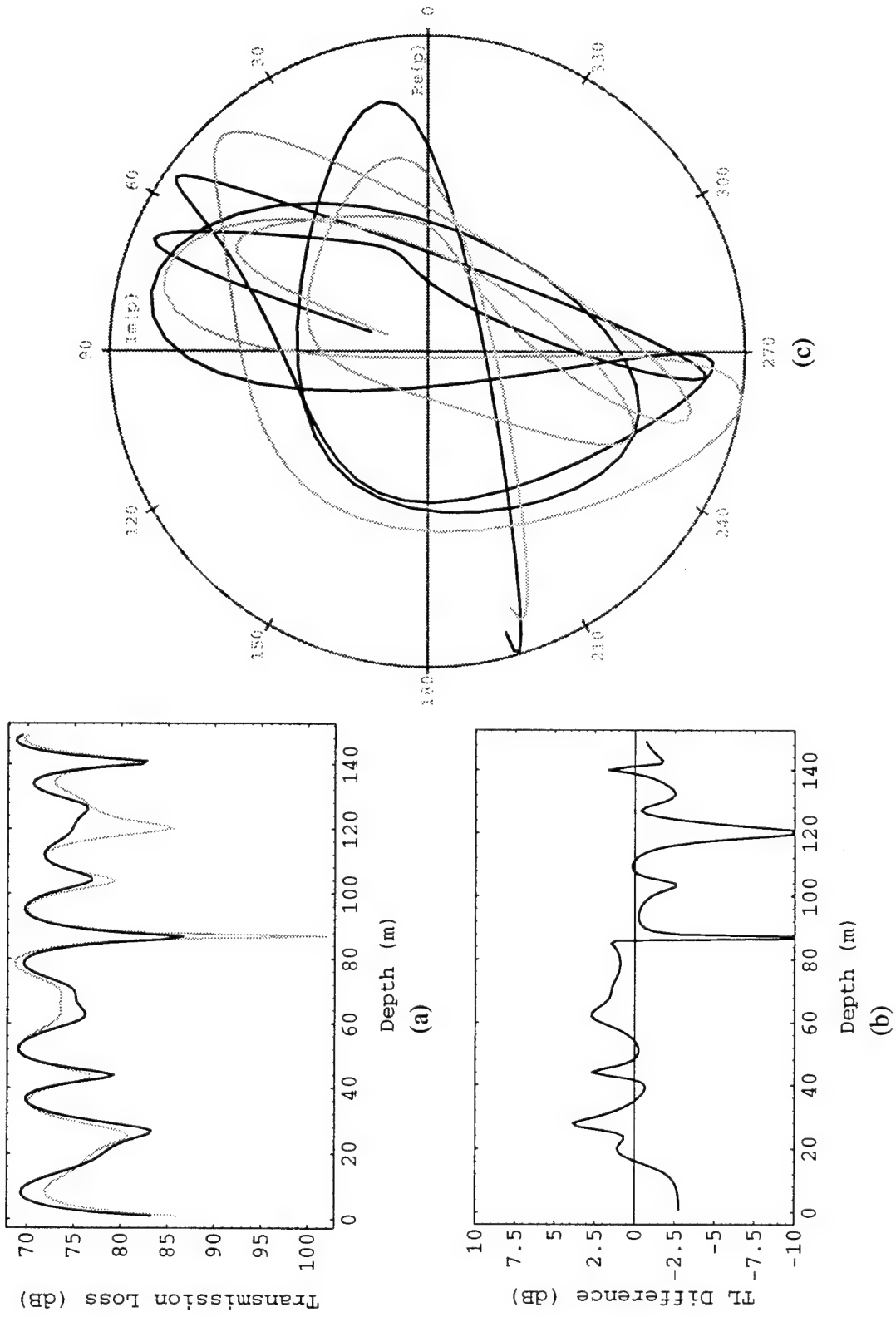
Figure 4.5. Ex. 4B: Field extrapolation at 3.0 km.
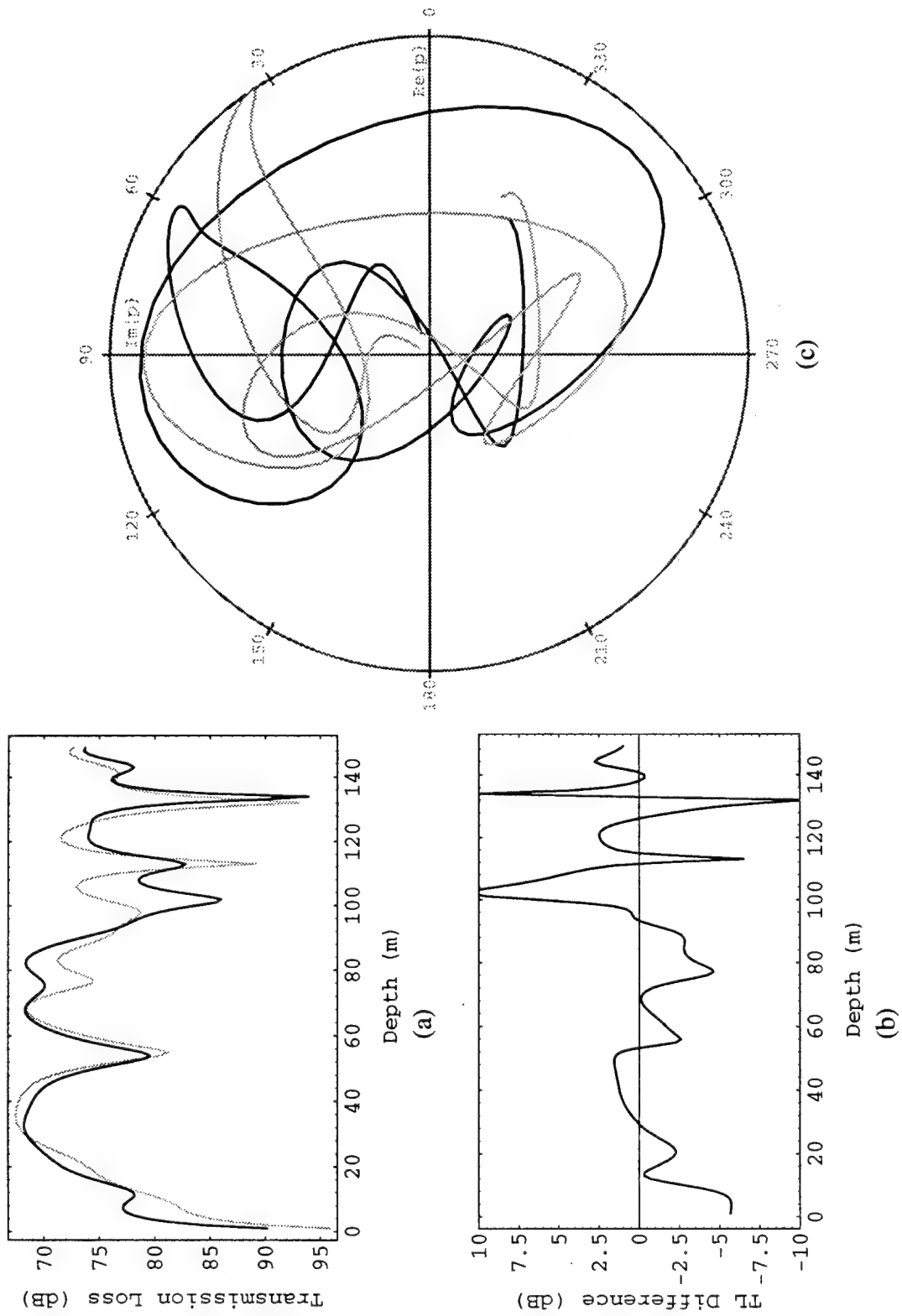
Figure 4.6. Ex. 4B: Field extrapolation at 5.0 km.

inverse square root of the perturbed eigenvalue in a first-order Taylor series approximation results in

$$\hat{p}(r_a, z_a) \cong \left[\frac{i}{8\pi r_a}\right]^{1/2} \frac{1}{\rho(z_0)} \sum_m \left(\psi_m(z_0)\psi_m(z_a) + \psi_m(z_0)\Delta\psi_m(z_a) + \Delta\psi_m(z_0)\psi_m(z_a)\right) \times$$

$$\left(\xi_m^{-1/2} - \frac{\Delta\xi_m \xi_m^{-3/2}}{2}\right) e^{i\xi_m r_a} e^{i\Delta\xi_m r_a}. \tag{4.36}$$

This expression can be expanded, once again ignoring terms that multiply perturbations together, into the following form:

$$\hat{p}(r_a, z_a) \cong \left[\frac{i}{8\pi r_a}\right]^{1/2} \frac{1}{\rho(z_0)} \left[\sum_m \psi_m(z_0)\psi_m(z_a)\xi_m^{-1/2} e^{i\xi_m r_a} e^{i\Delta\xi_m r_a} + \right.$$

$$\sum_m \left(\psi_m(z_0)\Delta\psi_m(z_a) + \Delta\psi_m(z_0)\psi_m(z_a)\right)\xi_m^{-1/2} e^{i\xi_m r_a} e^{i\Delta\xi_m r_a} -$$

$$\left. \sum_m \frac{\Delta\xi_m}{2\xi_m}\psi_m(z_0)\psi_m(z_a)\xi_m^{-1/2} e^{i\xi_m r_a} e^{i\Delta\xi_m r_a}\right]. \tag{4.37}$$

In Eq. 4.37, we take note of the first summation which would give us the expression for the perfect knowledge modeled field, except for a range-dependent phase factor. The second two summations have perturbational multipliers (either $\Delta\psi_m(z)$ or $\Delta\xi_m$). For Ex. 4B, Fig. 4.2 and Table 4.3 show that these perturbations are very small. Keeping in mind that this expression must be multiplied by the Green's function and integrated over depth, we also take note that for short ranges, where the range-dependent phase factors will have little effect, the matching coefficient is very close to that of the unperturbed case. This implies that the second two summations in Eq. 4.37 are not exerting a meaningful effect on the outcome. Since the effect of these two summations

will not vary much with range, we will neglect their contribution to the modeled field, and write the averaged extrapolated field as

$$\tilde{p}'(r_b, z_b) \cong \left[\frac{i}{8\pi r_b} \right]^{1/2} \frac{1}{\rho(z_0)} \sum_m \psi_m(z_0) \psi_m(z_b) \xi_m^{-1/2} e^{i\xi_m r_b} e^{i\Delta\xi_m r_a}. \tag{4.38}$$

We are assuming that for this scenario the obliquity factor did not appreciably affect the results.

The range-dependent unit-amplitude phase factor at the end of Eq. 4.38 is responsible for the degradation with range of the extrapolation results seen in Figs. 4.3-6. It is helpful to think of the modeled field as a weighted sum of the mode functions as in Eq. 1.11. As the extrapolation range increases, the phase of this term moves away from zero, causing the phase of the complex weight for each mode to skew from its "perfect knowledge" position. The coherent sum of the weighted mode functions is then changed. The larger the extrapolation range, the greater the phase shift, until the phase wraps through $180°$. At this point the matching coefficient would take on a "random" characteristic, depending on which modes had phase shifts closer to zero for a given range.

The degradation in the matching coefficient for this case is distinctly different from that due only to the obliquity factor as seen in Ch. 3. The obliquity factors are amplitude factors for each mode, and therefore sum in phase with the mode they are related to. This effect manifests itself in the transmission loss comparisons in Figs. 3.6-8 where the transmission loss errors tend to be either mostly positive or mostly negative, depending on whether the obliquity factors overweight or underweight the modes. The nature of the phase errors is much different as can be seen in Figs. 4.4-6. Here we see that the transmission loss errors are more evenly distributed about 0 dB.

We can undertake an analysis similar to Sec. 3.4 in order to determine the effect of the phase multipliers on the matching coefficient. We now write the fields as

$$p(z) = \sum_m W_m \psi_m(z)$$

$$\tilde{p}(z) = \sum_m W_m \psi_m(z) e^{i\Delta\xi_m r_a} .$$

$$(4.39)$$

Continuing the analysis much as in Eqs. 3.7-9, we arrive at the relationship

$$|K|^2 \sim \frac{\displaystyle\sum_m \sum_n e^{ir_a(\Delta\xi_m - \Delta\xi_n)} |W_m|^2 |W_n|^2}{\left(\displaystyle\sum_m |W_m|^2\right)^2} .$$

$$(4.40)$$

Making the same approximation as before, namely that the W_m's are constant with m, allows us to write Eq. 4.40 as

$$|K|^2 \sim \frac{\left|\displaystyle\sum_{m=1}^{M} e^{ir_a\Delta\xi_m}\right|^2}{M^2} = \Upsilon_{\Delta c} ,$$

$$(4.41)$$

where M is the number of modes that contribute significantly to the field. Note that for all $\Delta\xi_m$ equal to zero $\Upsilon_{\Delta\xi}$ is equal to one, which would be the expected value of $|K|^2$ for this case.

This relation implies that, if one has estimates of the changes in horizontal wavenumbers due to perturbations in the sound speed profile, predictions of the matching coefficient can be obtained. In this case, it is useful for determining how changing the variance of the sound speed profile perturbations will affect the matching coefficient. In Eqs. 4.31-33 we saw that, for the case of additive white Gaussian perturbations to the sound speed profile, the variance of the noise was a simple multiplier in the expression for the variance of the perturbations in the horizontal wavenumbers.
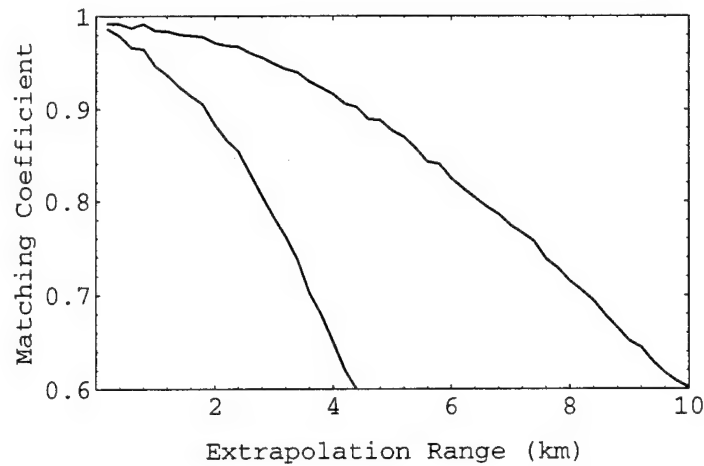
Figure 4.7. Results of increased variance for sound speed perturbations.

If, then, for the same realization of sound speed perturbations as seen in Fig. 4.1 we increase the variance from one to five, each horizontal wavenumber perturbation should be multiplied by $\sqrt{5} \cong 2.236$. In Eq. 4.41, this multiplier could be factored out of the eigenvalue perturbation and would become a multiplier on the range, meaning that the same level of matching coefficient for a given range as seen in Fig. 4.3 should occur at that range divided by approximately 2.236 for the increased variance case. Figure 4.7 shows the results of increasing the variance in the sound speed perturbations compared to the results of Fig. 4.3. Note that for the first case the matching coefficient is approximately 0.6 at a range of 10 km, and at the same level at approximately 4.4 km for the increased variance case ($10/2.236 \cong 4.472$).

4.6. Mismatch Effects: Sediment Parameters

This section will examine the effects of mis-estimation of some of the sediment parameters that affect acoustic propagation, namely compressional wave (sound) speed, compressional wave (sound) attenuation, and density. A general scenario like that seen in

Exs. 3F and 4B, i.e., a sedimentary layer underlying the water column, will be used. Note that this scenario is such that significant propagation of acoustic energy in the sediment does not occur. This scenario will be used to avoid confounding effects in the extrapolation algorithm due to truncated arrays since we are assuming that the arrays cannot extend into the bottom. Effects of a short reference array in deep water on the HAP algorithm (see Sec. 1.3) were examined in [Al-Kurd]. Bottom-propagating acoustic energy is of concern in some underwater scenarios, and its effect on extrapolation algorithms is an area of future work.

Accurate estimation of bottom parameters that affect acoustic propagation is usually a more difficult task than that of determining those for the water column. The sound speed profile in the water column is the most important property there and is commonly measured with CTD (conductivity-temperature-depth) instrumentation [Wen *et al.*]. Methods for determining bottom properties range from coring and grab-sample methods [Hamilton] to sophisticated techniques involving mathematical inversion of acoustic data (see articles by [Lindsay and Chapman] and [Dosso *et al.*], and references therein). The goal of this section is to attempt to gauge the relative importance of the various bottom parameters to the extrapolation technique.

4.6.1. Sound Speed Mismatch (Examples 4C and 4D)

For Ex. 4C, we will examine the effects of a constant offset in the sound speed estimate in the sediment, i.e., the slope of the sound speed profile in the sediment will remain unchanged. A common measure for describing different sediment types is the sound speed ratio, i.e., the ratio of the sound speed in the sediment to the sound speed in the water at the sediment-water boundary. For our scenario this ratio is $1540/1480 \cong 1.041$. It is reported in [Hamilton] that sound speed ratios can vary in the range from 0.976 to 1.201, with the values for "clayey-silt" compositions lying close to

Table 4.4. Eigenvalue Comparison for Ex. 4C.

Mode # (m)	Eigenvalue (ξ_m)	Change in Eigenvalue
2	$1.267 + i\,1.171 \times 10^{-5}$	$3.684 \times 10^{-5} + i\,2.504 \times 10^{-6}$
4	$1.262 + i\,1.121 \times 10^{-5}$	$3.541 \times 10^{-5} + i\,2.365 \times 10^{-6}$
6	$1.259 + i\,1.166 \times 10^{-5}$	$3.684 \times 10^{-5} + i\,2.446 \times 10^{-6}$
8	$1.254 + i\,1.696 \times 10^{-5}$	$5.341 \times 10^{-5} + i\,3.583 \times 10^{-6}$
10	$1.248 + i\,2.530 \times 10^{-5}$	$7.916 \times 10^{-5} + i\,5.625 \times 10^{-6}$
15	$1.228 + i\,8.751 \times 10^{-5}$	$2.390 \times 10^{-4} + i\,3.449 \times 10^{-5}$
22	$1.197 + i\,5.809 \times 10^{-4}$	$3.610 \times 10^{-3} - i\,7.247 \times 10^{-4}$
29	$1.166 + i\,7.716 \times 10^{-4}$	$3.573 \times 10^{-3} - i\,6.682 \times 10^{-4}$
36	$1.136 + i\,1.110 \times 10^{-3}$	$4.892 \times 10^{-3} - i\,4.535 \times 10^{-4}$
43	$1.105 + i\,1.182 \times 10^{-3}$	$4.022 \times 10^{-3} - i\,2.841 \times 10^{-4}$

1.0 (this value varies in the vicinity of 1.0 for clayey-silt sediments depending on the type of region in the ocean where the sediment is found, e.g., continental terrace, abyssal hill, or abyssal plain).

Example 4C will use a constant offset of -10 m/s in the sediment sound speed resulting in a sound speed of 1530 m/s at the sediment/water interface. All other parameters are the same as Ex. 3F (including the slope of the sound speed profile in the sediment). Note that we are assuming perfect knowledge of the sound speed profile in the water column. Table 4.4 shows a subset of the computed eigenvalues and their change from the unperturbed case. Notice the increasing trend in the perturbations to the eigenvalues, and that all the perturbations to the real parts of the eigenvalues are positive. We can use the results derived in Sec. 4.3 to explain this phenomenon.

Even though Eq. 4.23 was derived while considering sound speed perturbations in

the water column, it is also valid for sound speed perturbations in the sediment. Since we are assuming no perturbations in the water column, the integral now spans h (instead of zero) to ∞ and $\Delta c(z')$ becomes a constant with depth that can be taken outside the integral. Using the same reasoning found in Sec. 4.5.1, we can see that modes whose mode functions have more "energy" in the sediment will be affected to a greater extent by the perturbations to the sound speed estimate in the sediment. Also, since the perturbation to the sound speed is a negative constant, it comes out of the integral and multiplies the -1 already in front of the integral to create a positive multiplier. The rest of the integrand is then positive, so the perturbations to the real parts of the eigenvalues are positive in this case (the background wavenumber and sound speed can actually be thought of as complex numbers due to the attenuation in the sediment, as will be discussed in the next subsection).

Figure 4.8 shows a subset of the perturbed (black trace) vs. unperturbed (gray trace) mode functions. Notice that the lower order (propagating, in this case) modes have no noticeable perturbations. Again Eq. 4.26 gives us a clue as to why this is the case. The integrals now need only cover the sediment region since the sound speed profile in the water column is unperturbed. Since the lower order modes have little extension into the sediment, their perturbations are small.

Figure 4.9 shows some extrapolation results for this mis-estimation of the sediment sound speed profile. It is a plot of matching coefficient vs. extrapolation range, plotted on the same scale as Fig. 4.3 for comparison. We can use Eq. 4.41 to explain the much reduced falloff compared to the perturbed water column sound speed profile case (Ex. 4B). Note that the perturbations to the eigenvalues (for the non-stripped modes) are roughly of the same order of magnitude as those for the Ex. 4B, even though the sediment mismatch is 10 m/s, whereas the random perturbations to the water column sound speed profile had a variance of only 1 m/s. Also note that the eigenvalue perturbations for the
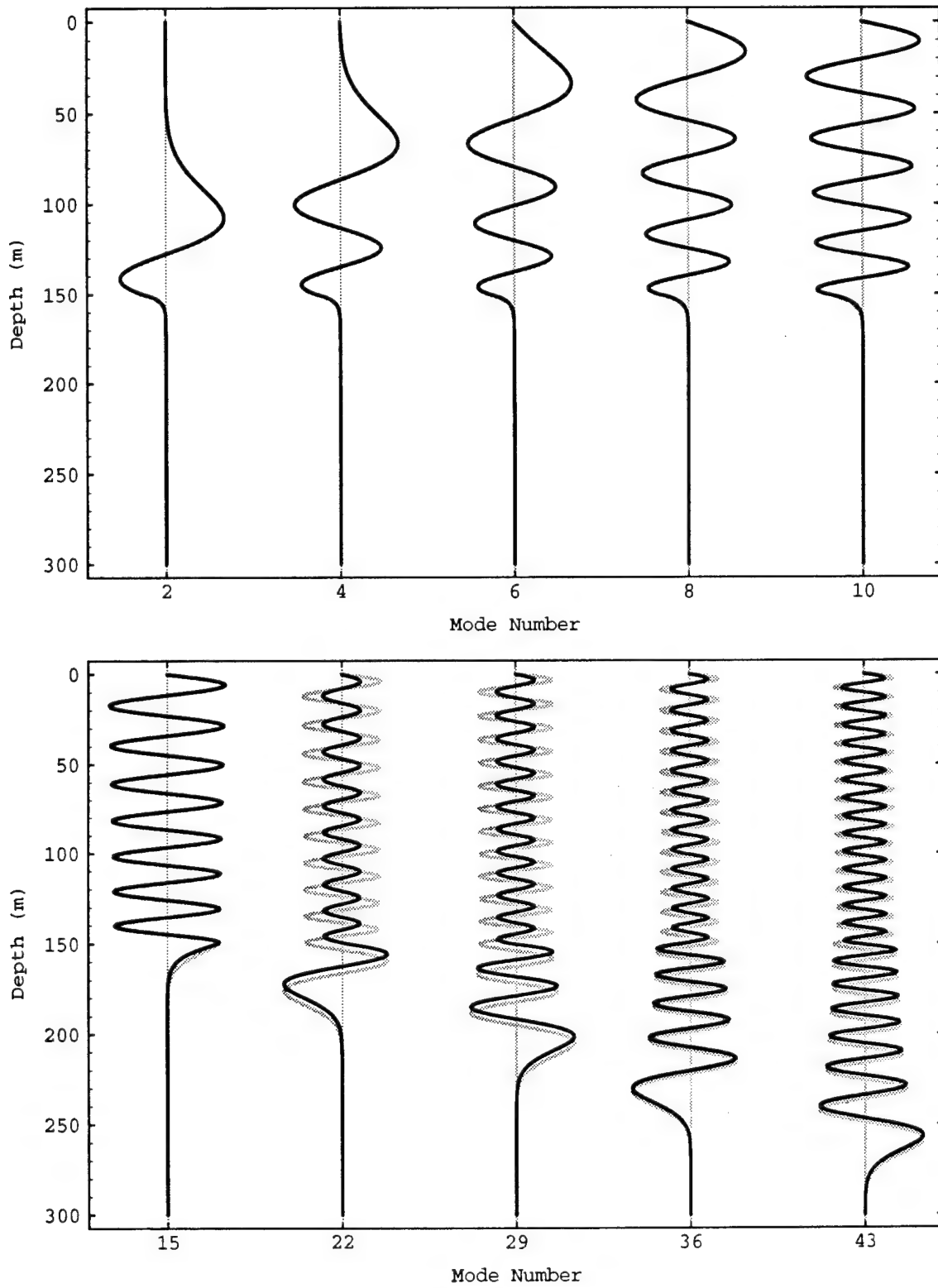
Figure 4.8. Comparison of "true" and perturbed mode functions for Ex. 4C.
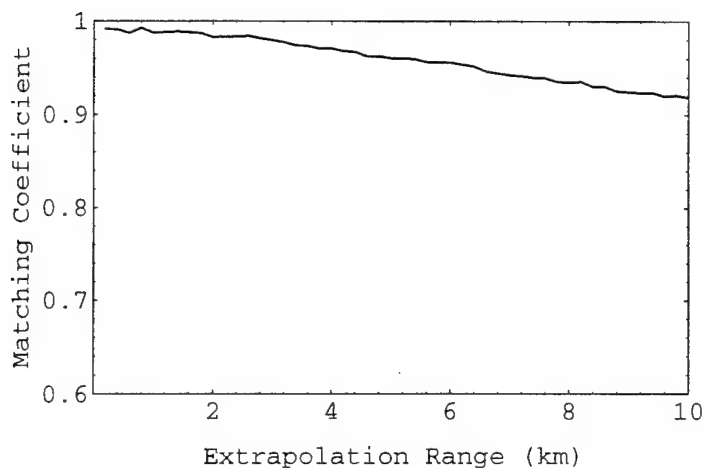
Figure 4.9. Ex. 4C: Constant offset in sediment sound speed profile.

water column fluctuations were not consistent in sign. In Eq. 4.41, we see that $\Upsilon_{\Delta c}$ is a function of the summation of the exponentiated eigenvalue perturbations. When the $\Delta\xi_m$ are all the same sign, they will sum in phase (assuming $r\Delta\xi_m \ll \pi$ for all m, which is the case for ranges considered here) as opposed to the case where they are of differing sign; hence the results seen in Fig. 4.9.

For a more direct comparison, we will perturb the sound speed in the sediment with the same random fluctuations that were added to the water column sound speed profile (Ex. 4D). Table 4.5 shows the eigenvalues for this perturbed system and the changes from the unperturbed state. In comparison to Table 4.3 (water column sound speed fluctuation case), we see that the perturbations to the real parts of the eigenvalues are roughly an order of magnitude less and of consistent sign. In comparison with Table 4.4 (constant offset in sediment sound speed profile), we see that the perturbations are also roughly an order of magnitude less. We would expect, then, that the degradation of the extrapolated fields as expressed in the matching coefficient would be much less for Ex. 4D than for Exs. 4B or 4C. This is indeed the case as seen in Fig. 4.10 which shows the matching coefficient vs. extrapolation range for Ex. 4D. As seen here, the matching

Table 4.5. Eigenvalue Comparison for Ex. 4D.

Mode # (m)	Eigenvalue (ξ_m)	Change in Eigenvalue
2	$1.267 + i\ 9.115 \times 10^{-6}$	$-1.311 \times 10^{-6} - i\ 8.599 \times 10^{-8}$
4	$1.262 + i\ 8.760 \times 10^{-6}$	$-1.192 \times 10^{-6} - i\ 8.535 \times 10^{-8}$
6	$1.259 + i\ 9.125 \times 10^{-6}$	$-1.311 \times 10^{-6} - i\ 9.294 \times 10^{-8}$
8	$1.254 + i\ 1.323 \times 10^{-5}$	$-2.027 \times 10^{-6} - i\ 1.456 \times 10^{-7}$
10	$1.248 + i\ 1.942 \times 10^{-5}$	$-2.981 \times 10^{-6} - i\ 2.520 \times 10^{-7}$
15	$1.228 + i\ 5.084 \times 10^{-5}$	$-1.204 \times 10^{-5} - i\ 2.187 \times 10^{-6}$
22	$1.191 + i\ 8.027 \times 10^{-4}$	$-1.740 \times 10^{-3} - i\ 5.028 \times 10^{-4}$
29	$1.158 + i\ 1.035 \times 10^{-3}$	$-3.960 \times 10^{-3} - i\ 4.044 \times 10^{-4}$
36	$1.126 + i\ 9.483 \times 10^{-4}$	$-4.287 \times 10^{-3} - i\ 6.150 \times 10^{-4}$
43	$1.095 + i\ 1.530 \times 10^{-3}$	$-5.551 \times 10^{-3} - i\ 6.405 \times 10^{-5}$
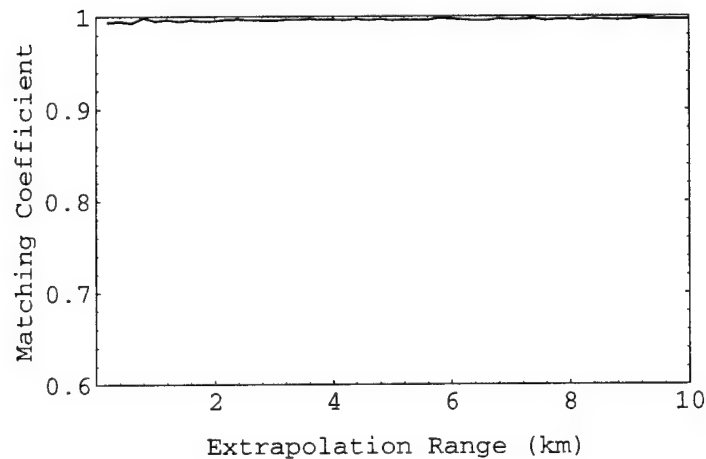
Figure 4.10. Ex. 4D: Random fluctuations in sediment sound speed profile.

coefficient hardly deviates at all from its ideal value of 1.0.

The general conclusion we can draw from the above results is that for environmental scenarios that do not support significant propagation of sound through the

sediment, the most important part of estimating the sound speed profile in the sediment is in the upper most regions of the sediment near the sediment/water interface where boundary conditions are established. While intuitively satisfying, we can also see why this is the case due to our analysis of the perturbations to the eigenvalues. The relationships governing these perturbations involve integrals over the mode functions where the sound speed perturbations exist. If the mode functions are small where the sound speed perturbations exist, then the perturbations to the horizontal wavenumbers (and mode functions) will be small.

4.6.2. Attenuation Mismatch (Example 4E)

The second sediment parameter whose effects on the extrapolation we are interested in gauging is attenuation. As was seen in Ch. 3, imaginary components of the horizontal wavenumbers manifest themselves in mode-dependent attenuations. The usual analysis of attenuation [Jensen *et al.*, Boyles] begins by assuming a small imaginary perturbation to the real-valued sound speed profile, i.e.,

$$c(z) = c_r(z) - ic_i(z). \tag{4.42}$$

This perturbation is negative because when the attenuation rule in general is written as $e^{(ikx - \alpha x)}$, where $k = \omega/c$ is the wavenumber and α is in units of nepers/m, we can set this equal to

$$e^{\frac{i\omega x}{c}} = e^{i\omega x \left(\frac{c_r + ic_i}{c_r^2 + c_i^2} \right)} \cong e^{i\omega x \left(\frac{c_r + ic_i}{c_r^2} \right)} \tag{4.43}$$

assuming that the squared c_i's are negligible. This allows us to make the approximation

$$\alpha \approx \frac{\omega c_i}{c_r^2},$$ (4.44)

meaning that a positive value of c_i leads to a positive value of α.

We can now undertake a perturbational analysis much as in Sec. 4.3 in order to determine what the perturbations to the horizontal wavenumbers will be for a perturbation in attenuation [Rajan *et al.*]. Using Eq. 4.42 as our perturbation and starting with a relationship much like Eq. 4.16, we eventually arrive at

$$\Delta \xi_m^{(1)} = \frac{i}{\xi_m^{(0)}} \int_0^\infty \rho^{-1}(z') \, (\psi_m^{(0)}(z'))^2 \, (k^{(0)}(z'))^2 \frac{c_i(z')}{c_0(z')} dz'.$$ (4.45)

Note that this is positive and wholly imaginary-valued. Substituting in for c_i via Eq. 4.44, we see that

$$\Delta \xi_m^{(1)} = \frac{i}{\xi_m^{(0)}} \int_0^\infty \rho^{-1}(z') \, (\psi_m^{(0)}(z'))^2 k^{(0)}(z') \alpha(z') dz',$$ (4.46)

where α is in units of nepers/m. The model we have been using expressed its attenuation in units of dB/wavelength. Using the approximation that $\alpha^{(\lambda)} \approx 8.686 \alpha \lambda$ [Jensen *et al.*], we can write the perturbations to the horizontal wavenumbers as

$$\Delta \xi_m^{(1)} = \frac{i}{2\pi(8.686)\xi_m^{(0)}} \int_0^\infty \rho^{-1}(z') \, (\psi_m^{(0)}(z'))^2 \, (k^{(0)}(z'))^2 \alpha^{(\lambda)}(z') dz',$$ (4.47)

where $\alpha^{(\lambda)}$ is now in units of dB/wavelength. Since this analysis started from the assumption of no attenuation (real-valued sound speed profile), determining the change in eigenvalues where the starting scenario had attenuation would require computations of the

eigenvalue changes via Eq. 4.47 for both scenarios and a differencing operation.

The perturbations to the mode functions are wholly imaginary-valued as well. These perturbations would be very small, and KRAKEN ignores them for the modes it calculates, so we will neglect them for this analysis.

We will again use the environmental scenario of Ex. 3F as our ground truth case (see Fig. 3.10), and now assume a mis-estimation of the sediment attenuation value. As reported in [Hamilton], attenuation values vary roughly over a range from very near 0.0 to 1.275 dB/λ. Also, it is mentioned in [Rajan *et al.*] that it is common practice to assume a constant attenuation value with depth, as was done for our model. The perturbation here (Ex. 4E) will consist of mis-estimating the sediment attenuation as 0.2 dB/λ vs. the ground truth value of 0.1 dB/λ.

Table 4.6 shows the eigenvalues and the changes from the ground truth case for Ex. 4E. Note that while there are some perturbations to the real parts of the eigenvalues, they are extremely small compared to the actual eigenvalues, and hence we will neglect them. The perturbations to the imaginary parts, however, are comparable in order of magnitude to the base values. Noting that the imaginary parts of the eigenvalues are responsible for attenuations imparted to each mode, we can compare the attenuations over a 20 km range due to the ground truth and perturbed eigenvalues (see Fig. 3.12) as in Fig. 4.11. The perturbed results are in gray. As we would expect, the higher attenuation value has resulted in greater attenuation being imparted to each mode.

Extrapolation results (matching coefficient vs. range) for this case are shown in Fig. 4.12. The degradation in the extrapolated field as expressed by the matching coefficient is quite small for this case.

In general, since the perturbations to the imaginary parts of the eigenvalues manifest themselves in modal-dependent amplitude factors, we can use an analysis similar to that for the obliquity factors to derive an expression that predicts the degradation in

Table 4.6. Eigenvalue Comparison for Ex. 4E.

Mode # (m)	Eigenvalue (ξ_m)	Change in Eigenvalue
2	$1.267 + i\ 1.839\text{x}10^{-5}$	$0 + i\ 9.192\text{x}10^{-6}$
4	$1.262 + i\ 1.768\text{x}10^{-5}$	$0 + i\ 8.837\text{x}10^{-6}$
6	$1.259 + i\ 1.843\text{x}10^{-5}$	$0 + i\ 9.209\text{x}10^{-6}$
8	$1.254 + i\ 2.674\text{x}10^{-5}$	$-1.190\text{x}10^{-7} + i\ 1.336\text{x}10^{-5}$
10	$1.248 + i\ 3.933\text{x}10^{-5}$	$-1.200\text{x}10^{-7} + i\ 1.965\text{x}10^{-5}$
15	$1.228 + i\ 1.060\text{x}10^{-4}$	$-4.770\text{x}10^{-7} + i\ 5.293\text{x}10^{-5}$
22	$1.193 + i\ 2.609\text{x}10^{-3}$	$-8.703\text{x}10^{-6} + i\ 1.304\text{x}10^{-3}$
29	$1.162 + i\ 2.882\text{x}10^{-3}$	$-9.298\text{x}10^{-6} + i\ 1.442\text{x}10^{-3}$
36	$1.131 + i\ 3.125\text{x}10^{-3}$	$-9.537\text{x}10^{-6} + i\ 1.562\text{x}10^{-3}$
43	$1.101 + i\ 2.935\text{x}10^{-3}$	$-9.179\text{x}10^{-6} + i\ 1.469\text{x}10^{-3}$

Figure 4.11. Ex. 4E: Attenuation due to imaginary part of eigenvalues.

matching coefficient for given perturbations in the imaginary parts of the eigenvalues. In this case we arrive at the relationship
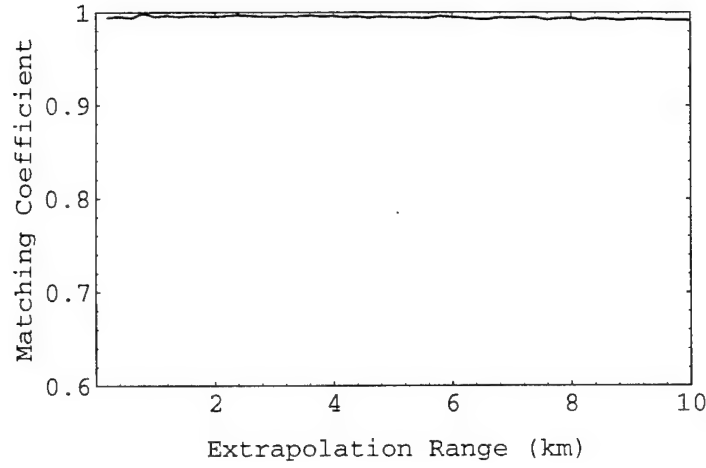
Figure 4.12. Ex. 4E: Constant offset in sediment attenuation.

$$\Upsilon_{\Delta\alpha} = \frac{\left(\sum_m e^{-r_a Im\{\Delta\xi_m\}}\right)^2}{M\sum_m e^{-2r_a Im\{\Delta\xi_m\}}}. \tag{4.48}$$

4.6.3. Density Mismatch (Example 4F)

It is shown in [Rajan *et al.*] that similar results can be obtained for perturbations in the density profile as were obtained for perturbations to the sound speed and attenuation. Specifically, we can define an intermediate function

$$m(z) = \frac{(\rho(z))^{-1/2}}{2}\frac{d}{dz}\left(\frac{\rho'(z)}{(\rho(z))^{3/2}}\right), \tag{4.49}$$

from which the perturbations to the eigenvalues can be written as

$$\Delta\xi_m^{(1)} = \frac{1}{2\xi_m^{(0)}}\int_0^\infty (\rho_0(z'))^{-1}(\psi_m^{(0)}(z'))^2 \Delta m(z')dz'. \tag{4.50}$$

The perturbations to the mode functions follow in a similar manner.

Table 4.7. Eigenvalue Comparison for Ex. 4F.

Mode # (m)	Eigenvalue (ξ_m)	Change in Eigenvalue
2	$1.267 + i\ 1.029 \times 10^{-5}$	$1.162 \times 10^{-4} + i\ 1.092 \times 10^{-6}$
4	$1.263 + i\ 9.065 \times 10^{-6}$	$9.620 \times 10^{-5} + i\ 2.196 \times 10^{-7}$
6	$1.259 + i\ 8.875 \times 10^{-6}$	$8.798 \times 10^{-5} - i\ 3.432 \times 10^{-6}$
8	$1.254 + i\ 1.219 \times 10^{-5}$	$1.098 \times 10^{-4} - i\ 1.191 \times 10^{-6}$
10	$1.249 + i\ 1.702 \times 10^{-5}$	$1.305 \times 10^{-4} - i\ 2.652 \times 10^{-6}$
15	$1.228 + i\ 4.092 \times 10^{-5}$	$9.859 \times 10^{-5} - i\ 1.210 \times 10^{-5}$
22	$1.193 + i\ 1.448 \times 10^{-3}$	$-6.414 \times 10^{-5} + i\ 1.419 \times 10^{-4}$
29	$1.162 + i\ 1.561 \times 10^{-3}$	$8.893 \times 10^{-5} + i\ 1.209 \times 10^{-4}$
36	$1.131 + i\ 1.675 \times 10^{-3}$	$-7.260 \times 10^{-5} + i\ 1.117 \times 10^{-4}$
43	$1.101 + i\ 1.519 \times 10^{-3}$	$1.695 \times 10^{-4} + i\ 5.254 \times 10^{-5}$

Values of density found in sediments vary from lows of roughly 1.2 g/cm^3 [Hamilton] to 2.7 g/cm^3 [Jensen *et al.*]. For Ex. 4F we will perturb our ground truth estimate by changing the density to 2.0 g/cm^3 vs. the true value of 1.5 g/cm^3. Table 4.7 shows a subset of the perturbed eigenvalues and their change from the ground truth case. The perturbed mode functions showed essentially no change from the ground truth, so they are not shown.

Figure 4.13 shows the matching coefficient vs. range results for Ex. 4F. Since the density perturbations affect mainly the real part of the eigenvalues (like sound speed perturbations), we can use the expression in Eq. 4.41 to predict the degradation in the matching coefficient due to the perturbations in the density, i.e., $\Upsilon_{\Delta\rho} = \Upsilon_{\Delta c}$.

4.6.4. Discussion of Sediment Perturbation Results

The goals of this section were twofold. One was to reinforce the finding in
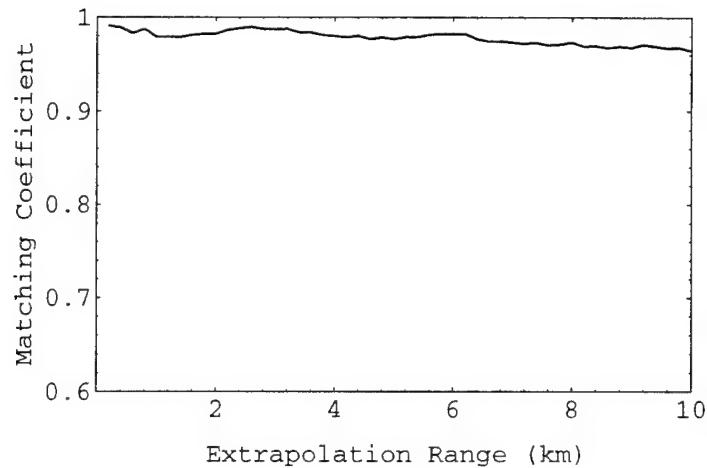
Figure 4.13. Ex. 4F: Constant offset in sediment density.

[Rouseff *et al.*] that for environments where sediment-borne energy is negligible, the parameters in the bulk of the sediment that affect propagation are significantly less important relative to other factors such as the sound speed in the water column or the bathymetry (the bathymetry issue was dealt with in [Rouseff *et al.*]). The examples given here showed that for relatively large perturbations to the sediment parameters, the degradation in matching coefficient was significantly less than that caused by perturbations to the water column sound speed profile. These differences were explained by appealing to the perturbational theory results that showed how modes were affected by the parameter perturbations as a function of how far their mode functions extended into the sediment. In this case, where the mode functions that contributed significantly to the fields did not extend very far into the sediment, the perturbations were relatively small and the extrapolated fields exhibited high matching coefficients relative to the ground truth fields.

The second goal was to give an approximate measure by which one could, given a certain perturbed scenario, determine how the matching coefficient would be affected. This was accomplished through the Υ expressions. In the preceding text, individual Υ's

were derived depending on whether the perturbations to the modes were phase or amplitude factors. We note in summary that a combined Υ can be defined by assuming the extrapolated field is compose of modes with a complex weighting factor, i.e.,

$$\tilde{p}(z) = \sum_m A_m \psi_m(z) a_m e^{i\beta_m}.$$

(4.51)

This results in the more general relation

$$\Upsilon = \frac{\left| \sum_{m=1}^{M} a_m e^{i\beta_m} \right|^2}{M \sum_{m=1}^{M} a_m^2}.$$

(4.52)

4.7. Summary of Chapter 4

Chapter 4 dealt with the effects on the extrapolation algorithm of mis-estimating some of the environmental parameters that are used as input to the modeled field processing. Expressions were derived which showed how perturbations to environmental parameters affect the mode functions and horizontal wavenumbers of the modeled field. These expressions were then interpreted with the aid of several example scenarios. It was seen for scenarios where a sediment layer strips off the higher order, more steeply propagating modes, that the extrapolation algorithm degrades more rapidly with extrapolation range due to perturbations in the water column sound speed profile than due to relatively larger perturbations to sediment parameters (sound speed, attenuation, and density). Expressions were shown which allow estimation of the matching coefficient given estimates of the perturbations to the horizontal wavenumbers. Chapter 5 will explore numerical integration techniques for the extrapolation algorithm.

Chapter 5: Integral Estimation for Acoustic Field Extrapolation

5.1. Introduction to Chapter 5

In Ch. 2, the basic theory behind the acoustic field extrapolation algorithm was explored. There we saw that calculating the integral of the product of either the modeled field or its derivative and the measured calibration data (i.e., Green's function data) is central to the algorithm. Practicality requires that the calibration data be collected for discrete transmitter and receiver locations along the reference arrays, meaning that a numerical integration, or "quadrature," technique must be used to estimate the integral.

This chapter will explore issues related to estimating the integrals as in Eq. 2.4. It will begin with a discussion of trapezoidal integration, and how the extrapolation algorithm degrades as the density of transmitters along the reference array decreases when this numerical integration method is used. It will suggest methods by which we can estimate the spacing of elements required along the reference arrays in order to extrapolate fields reliably. Another numerical integration technique, called an inner product quadrature formula, will be examined which uses the modeled mode functions as an integration basis. This integration method will show the relationship between the Huygens' principle-related extrapolation algorithm and a modal decomposition-based method.

For this material we will assume that the reference transmit array spans the water column and the transmitters are spaced equally along the array. Note that for this application our degrees of freedom are restricted in that the abscissa points where the function to be integrated is evaluated are defined by the locations in depth of the reference transmitters. This means that integration methods that have flexibility in choosing the abscissa locations, thereby adding more degrees of freedom, cannot be used (e.g., certain types of Gaussian quadratures [Press *et al.*, Davis and Rabinowitz].)

5.2. Trapezoidal Integration

5.2.1. Definition

A common and easily implementable method of numerical integration for evenly spaced sample points is trapezoidal integration [Press *et al.*]. Trapezoidal integration is performed by assuming straight lines between the ordinates of the function to be integrated, and summing the areas of the resulting trapezoids as shown in Fig. 5.1. For this example we can say that

$$\int_0^{x_5} y(x)\,dx \approx \sum \text{areas of trapezoids}. \tag{5.1}$$

The area of any given trapezoid is

$$A_n = h\frac{(y(x_n) + y(x_{n-1}))}{2}. \tag{5.2}$$

By expanding the expressions for all the trapezoids and collecting like terms, we find that the integral of the function can be approximated by
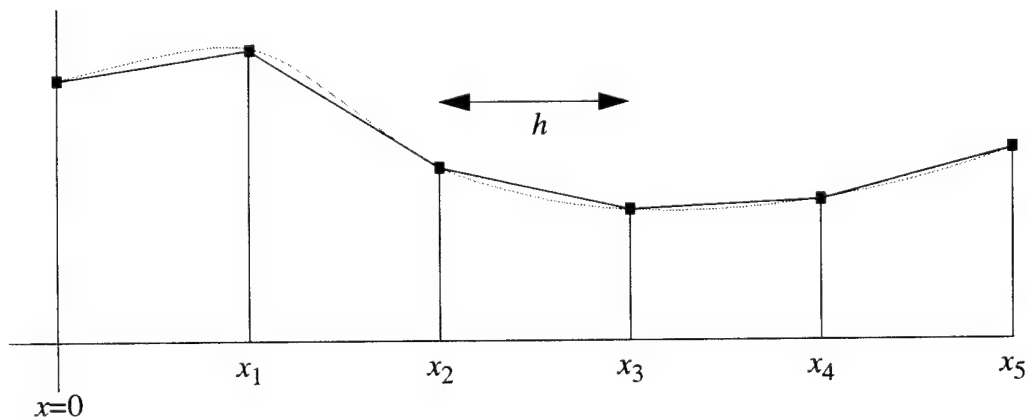
Figure 5.1. Example of trapezoidal integration.

$$\int_0^{x_5} y(x)\,dx \approx h\left[\frac{y(0)}{2} + y(1) + y(2) + y(3) + y(4) + \frac{y(5)}{2}\right]. \tag{5.3}$$

The general trapezoidal integration rule is given by

$$\int_{x_0}^{x_n} y(x)\,dx \approx h\left(\frac{y(x_0)}{2} + y(x_1) + y(x_2) + \dots + y(x_{n-2}) + y(x_{n-1}) + \frac{y(x_n)}{2}\right). \tag{5.4}$$

Note that except for the end conditions, this equates to simply summing the samples of the function to be integrated and multiplying by the interval between samples.

5.2.2. Fourier Theory Considerations

We define the Fourier transform of a continuous-time function $x(t)$ as

$$X(f) = \int_{-\infty}^{\infty} x(t)e^{-j2\pi ft}\,dt, \tag{5.5}$$

where f is frequency. This leads to the expression

$$X(0) = \int_{-\infty}^{\infty} x(t)\,dt. \tag{5.6}$$

In other words, the integral of a function over all time is equal to the "DC" term of its Fourier transform.

If we assume that a given $x(t)$ is bandlimited, i.e., its Fourier transform is identically zero for all $|f| > B$, then using a Fourier series approach [Marks] we can arrive at the relationship

$$\int_{-\infty}^{\infty} x(t)dt = T \sum_{n=-\infty}^{\infty} x(nT), \tag{5.7}$$

where T is the sampling interval and $1/T \geq 2B$ in order to satisfy the Nyquist sampling criterion. Note the similarity to the trapezoidal integration rule, Eq. 4.4. Since a perfectly bandlimited function must exist for all time $-\infty < t < \infty$, the end points do not affect the result. We see then that a properly sampled bandlimited function can be integrated exactly using trapezoidal integration.

Signals sampled below the Nyquist frequency can also be integrated exactly. Figure 5.2 illustrates why. The top picture in Fig. 5.2 shows a properly sampled bandlimited signal with $1/T_1 > 2B$ so that there is no aliasing of the replicated spectra. The bottom picture shows the results of sampling with $B < 1/T_2 < 2B$. The gray areas show where the baseband spectrum is contaminated by the overlapping replicas due to
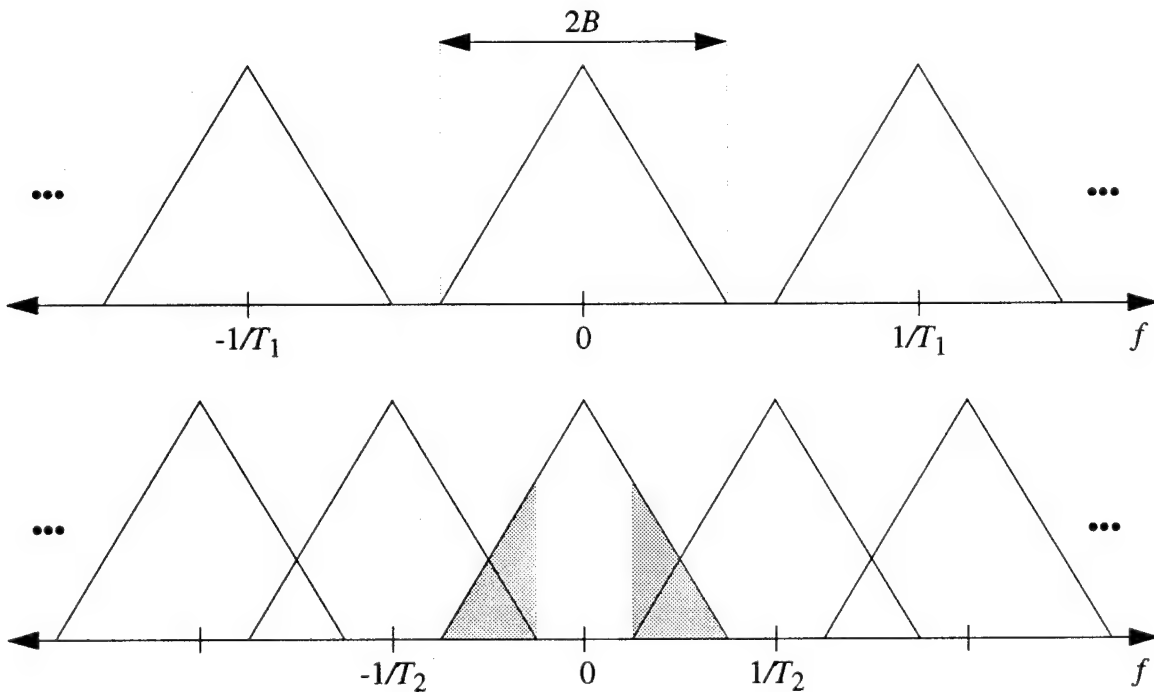

Figure 5.2. Frequency domain: aliasing of sampled signals.

aliasing. Note that the DC value, $X(0)$, is not contaminated. Therefore, exact integration results can be obtained for bandlimited signals by summing the samples, assuming that the sampling interval is such that $B < 1/T < 2B$.

Truly bandlimited signals (which must exist for all time) are mostly mathematical niceties. Many real-world signals, however, are "essentially" bandlimited in that their energy content above a given frequency limit is very small. Since these signals are not truly bandlimited, Eq. 5.7 is not an equality. As the sampling interval decreases (sampling rate increases), however, and the essential bandwidth of the signal is accounted for in the sampling, Eq. 5.7 becomes a better approximation. Using the above ideas we can determine the sampling interval at which a trapezoidal integration will start to fail to provide a close estimate of the true integral.

5.2.3. Trapezoidal Integration Example

For this example we will use the same environmental scenario as Ex. 3F (attenuating sediment layer underlying the water column) so that obliquity factor effects are negligible. In Section 3.4.2 we saw that using a reference transmit array whose transmitters were spaced 1 m apart resulted in a matching coefficient of approximately 0.996 for an extrapolation from (r_{e1}, z_s) = (5 km, 30 m). Figure 5.3 shows the magnitude-squared of the discrete Fourier transforms (DFT's, calculated by zero padding out to 1024 and using an FFT routine, see [Oppenheim and Schafer]) of a) the modeled field $p(5, z_a)$, b) a representative Green's function, specifically that for a receive depth of 74 m $G(25, 74; 5, z_a)$, and c) the product of the modeled field and Green's function. It is important to remember that in the acoustic field extrapolation algorithm an integral must be approximated for each point along the receive array where an extrapolated field value is desired. The Green's function in this case is the result of transmitting from each of the transmitters along the reference array and receiving at depth 74 m at the receive array,
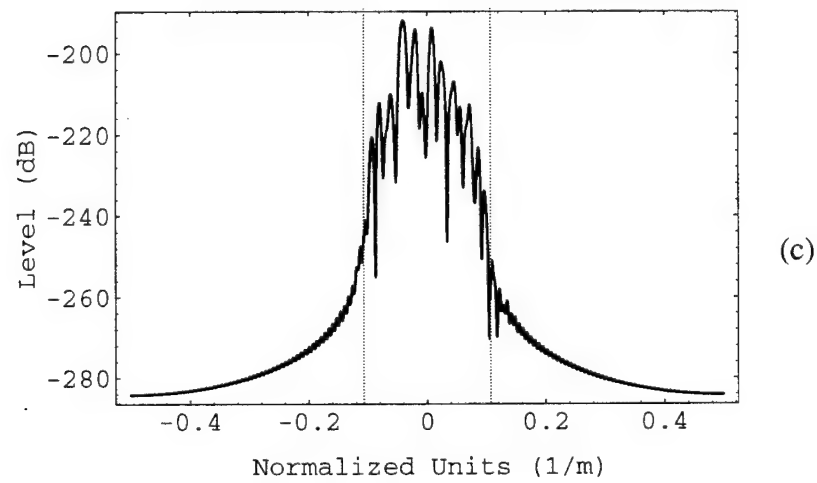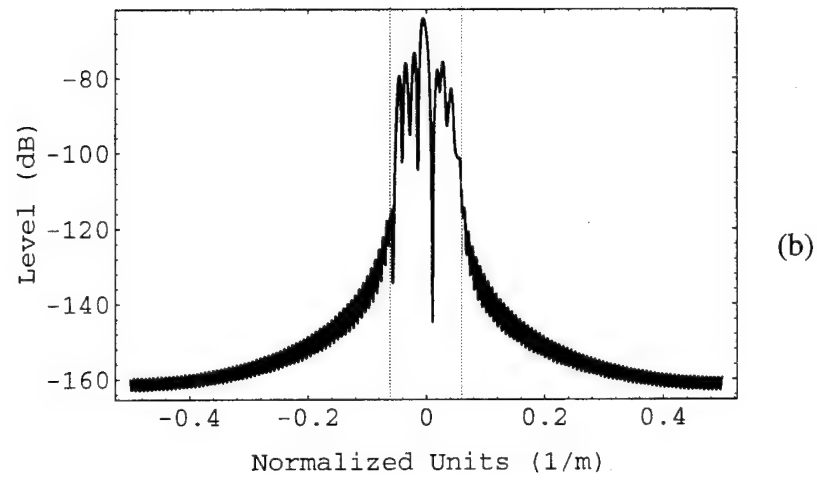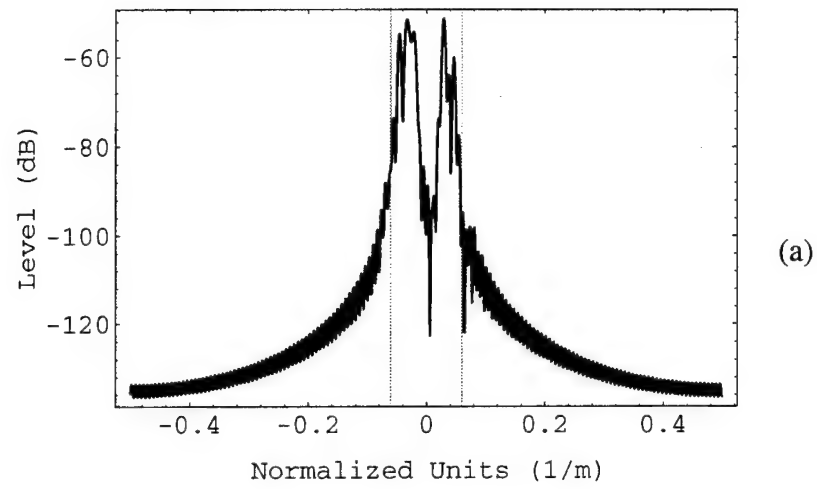
Figure 5.3. DFT's of: a) modeled field, b) Green's function, c) product.

hence the depth variable z_a. Using the principle of acoustic reciprocity (see Section 2.5.8), this can be seen as equivalent to transmitting from the receive location and receiving along the reference transmit array.

Figure 5.3a shows the DFT of the modeled field. The horizontal axis, or what we would think of as the frequency axis (units Hz, or 1/s) for the DFT of a time-domain signal, is in normalized units of 1/m; 0.5 units on this axis refers to one-half the spatial sampling "rate." The gray vertical markers show an "eyeball" estimate of the essential "bandwidth" of the sampled field. Figure 5.3b shows the DFT of the Green's function for the stated receive depth. Note that the essential bandwidth estimate appears very close to that of the modeled field. Keeping in mind the reciprocity relationship for the Green's function and interpretation for the fields based on the sum of weighted mode functions, we find this result intuitively satisfying since both functions are weighted sums of the same mode functions.

Figure 5.3c shows the DFT of the product of the modeled field and the Green's function. The essential bandwidth here is roughly twice that seen in Figs. 5.3a and b. Again, this result is intuitively satisfying since multiplying functions in the spatially sampled domain (equivalent to the temporally sampled domain for functions of time) translates to convolving their representations in the spatial "frequency" domain (often referred to as the modulation property; see [Oppenheim *et al.*]).

We can now predict the effect that increasing the spacing of the elements on the reference array (decreasing the spatial sampling "rate") has on our extrapolation algorithm. In Fig. 5.3c we see that the spectral content is not zero outside the essential bandwidth region, but rather gradually falls off. From the results of Sec. 5.2, we can expect that as the spacing is increased from 1 m, the extrapolation results will degrade as this energy is aliased into $X(0)$. When the outside edges of the "essential" bandwidth region (marked by the bandwidth delimiters in Fig. 5.3c) begin to be aliased into $X(0)$,
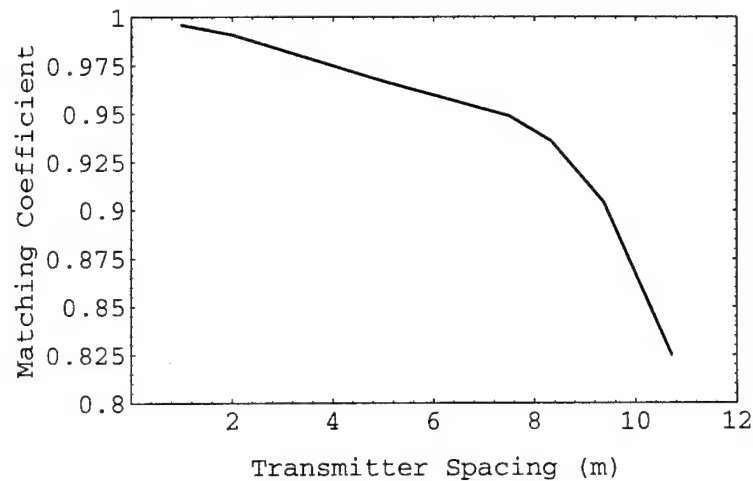
Figure 5.4. Degradation of matching coefficient with increased array spacing.

we should expect a more drastic degradation of the extrapolation results. From Fig. 5.3c, we see that the approximate bandwidth delimiter is placed at roughly 0.11 normalized units. The factor that would cause this portion to begin to be aliased into $X(0)$ is $1/0.11 \cong 9.09$. Therefore, we can expect more serious degradation to occur near spacings of approximately 9.09 x 1m = 9.09m.

Figure 5.4 shows the results of varying the spacing of elements along the reference transmit array for the previously stated scenario. As in previous simulations, the matching coefficient results have been averaged over a grid of source locations. This plot shows the anticipated mild degradation of the results to a certain spacing, followed by a sharp downturn. Note that the predicted location of the sharp downturn, ~9.09 m, does occur in the "knee" of the curve.

This analysis, then, suggests a method by which we could estimate the spacing needed for a reference array in a given environment. Assuming that reasonably reliable modeled fields can be produced (which would be necessary for the success of the extrapolation algorithm in any case), we could produce a set of modeled fields for a representative grid of hypothetical source locations. Noting that spacing of the modeled

field points in depth is not restricted, we could then make an estimate of the essential bandwidth of the modeled fields by discrete Fourier transforming in depth. The grid of source locations should produce a good idea of the maximum essential bandwidth. If no a priori knowledge of the essential bandwidth of the Green's function is available, merely doubling the bandwidth obtained for the modeled fields can serve as a first-order approximation of the product bandwidth. Otherwise, information about the bandwidth of the Green's function can be incorporated into the estimate. Using an analysis similar to that stated above, it can be estimated at what spacing the essential bandwidth portion of the product Fourier transform will begin interfering with the $X(0)$ term and drastically reducing the matching coefficient. As can be seen from Fig. 5.4, decreasing the spacing (adding more transmitters) will gradually aid the performance of the extrapolation algorithm.

5.3. Inner Product Quadrature Formulas for Numerical Integration

Some types of numerical integration methods involve fitting functions with integrals that can be calculated analytically to the sampled values of the function to be integrated. Many of the methods use orthogonal polynomials, such as Legendre or Chebyshev, for the basis functions [Press *et al.*]. Noting for now that we can produce a "customized" basis set of orthonormal functions via a numerical normal mode decomposition, we will now outline the basic theory behind an integration method through which we can take advantage of this fact. In the following section some results from [Gribble] and [McGrath] are summarized.

5.3.1. Theory for Inner Product Quadrature Formulas

The trapezoidal rule is one example of a so-called Regular Quadrature Formula (R.Q.F), i.e.,

$$f(z)\mathrm{d}z \equiv I(f) \sim Q^{(m)}(f) \equiv \sum_{i=0}^{m} a_i f(z, \tag{5.8}$$

where R is a real bounded interval and the a_i's are coefficients that define the particular R.Q.F. For integrands that are inherently products of functions (as is our field extrapolation algorithm), i.e.,

$$\int_R w(x)f(x)g(x)\mathrm{d}x \equiv I(f;g), \tag{5.9}$$

where $w(x)$ is a nonnegative weight function, there exist what are called Inner Product Quadrature Formulas (I.P.Q.F.'s).

In general, these I.P.Q.F.'s take the form

$$I(f;g) \sim Q^{(m,n)}(f;g) \equiv \sum_{i=0}^{m} \sum_{j=0}^{n} f(y_i)a_{ij}g(z_j), \tag{5.10}$$

where the y_i's and z_j's are the nodes at which f and g respectively are evaluated, and the a_{ij}'s are determined by requiring Eq. 5.10 to be exact when f and g are functions that are linear combinations of sets of linearly independent basis functions, i.e.,

$$f \in F^\gamma \equiv \{f_0, \ldots, f_\gamma\}$$

$$g \in G^\delta \equiv \{g_0, \ldots, g_\delta\}. \tag{5.11}$$

Eq. 5.10 can be equivalently expressed in matrix form as

$$Q^{(m,n)}(f;g) \equiv f^T A g. \tag{5.12}$$

Note that f and g are treated individually in that they can be evaluated on separate sets of

nodes (i.e., $\{x_0, ..., x_m\}$ and $\{y_0, ..., y_n\}$ not coincident) or have different linear bases if need be.

To solve for the matrix A, start by defining the matrices

$$F = \{f_i(y_j)\}_{i, j = 0}^{m}$$
$$G = \{g_i(z_j)\}_{i, j = 0}^{n} \tag{5.13}$$

so that each row of the matrices contains the samples of a given basis function evaluated at the nodes assigned to that basis as defined in Eq. 5.10. According to [Gribble] and [McGrath], the algorithm proceeds by solving for each $i = 0, ..., m$,

$$G \begin{pmatrix} \alpha_{0i} \\ ... \\ \alpha_{ni} \end{pmatrix} = \begin{pmatrix} I(f_i;g_0) \\ ... \\ I(f_i;g_n) \end{pmatrix}, \tag{5.14}$$

where $\alpha_{ji} = \sum_{k = 0}^{m} a_{kj} f_i(x_k)$, and obtaining the elements of A as solutions of

$$F \begin{pmatrix} a_{0j} \\ ... \\ a_{mj} \end{pmatrix} = \begin{pmatrix} \alpha_{j0} \\ ... \\ \alpha_{jm} \end{pmatrix} \tag{5.15}$$

for each $j = 0, ..., n$.

Several generalizations and simplifications can be made to this algorithm. First note that, as stated, the matrices F and G are square (i.e., have the same number of nodes as basis functions) to allow use of the standard matrix inverse in solving Eqs. 5.14 and 5.15. The algorithm can be made to work with overdetermined F and G matrices (more nodes than basis functions) through use of the pseudoinverse [Lawson and Hanson]. Let the pseudoinverse of a matrix F be denoted $F^{(-1)}$.

Additionally, the matrix A need not be solved for column by column. For instance, one can first define the matrix

$$S = \{I(f_i, g_j)\}_{i, j = 0}^{M_F, M_G},$$

(5.16)

where M_F and M_G are the number of basis functions in each basis. Also, let the matrix made up of the $\alpha_{i, j}$ values be denoted as Ξ. We can then say that $G\Xi = S^T$ (a matrix formulation of Eq. 5.14 for all $i = 0, ..., m$) and then $\Xi = G^{(-1)} S^T$. Likewise, we can say $FA = \Xi^T$ (a matrix formulation of Eq. 5.15 for all $j = 0, ..., n$), and finally that

$$A = F^{(-1)} \Xi^T = F^{(-1)} S (G^{(-1)})^T.$$

(5.17)

5.3.2. Use of I.P.Q.F.'s for the Extrapolation Algorithm

An I.P.Q.F. can be used to approximate the integral involved in the field extrapolation algorithm. This is accomplished by using the mode functions obtained through a numerically based normal mode decomposition algorithm (such as KRAKEN) as the basis functions described in the previous section (note that since the mode functions form an orthonormal set it can also be shown that they are linearly independent [Naylor and Sell]). In order for the F and G matrices seen above to be square or overdetermined, we see that the requirement for the number of reference transmitters is $n \geq M$, where M is the number of propagating modes in the problem. Examples in the following section will illustrate the improvements in performance obtained using the I.P.Q.F.

By using this integration method, we have moved away from the general formulation explored in Ch. 2 where the modeled field $\hat{p}$ could be generated through any number of acoustic field simulation methods. While this is still the case, since the modal decomposition would need to be calculated in any case as part of the I.P.Q.F., it would

make sense to also use the modal decomposition to form the modeled field. In this form the Huygens' principle-based formulation can be made equivalent to an explicit modal decomposition-based method of field extrapolation which was introduced in [Rouseff *et al.*]. The modal decomposition version of the algorithm is an adaptation of processing methods developed in [Yang (1987)] and [Yang (1990)].

As we did earlier in this dissertation, we will make a simplifying assumption that, for cases where there is a sedimentary bottom layer into which transmit/receive arrays cannot extend, the bottom parameters will be such that any modes that would propagate significant energy in the bottom will be stripped off. In other words, we will restrict ourselves to primarily water-borne energy. This will allow us to assume a constant density of $\rho(z) = 1$ for the water column (a common assumption in many cases), and to rewrite our orthonormality condition for the mode functions as

$$
\int_0^D \psi_m(z)\psi_n(z)dz \equiv \left\{ \begin{array}{l} 1, m = n \\ 0, m \neq n \end{array} \right. ,
\tag{5.18}
$$

where D is the water depth.

5.3.3. Extrapolation Examples Using I.P.Q.F.'s

Example 5A will use the same basic scenario as Ex. 3F in Sec. 3.5, i.e., an attenuating sediment layer underlying the water column. The only difference will be that instead of spacing transmitters along the reference array at $\Delta z = 1$ m, 18 evenly spaced transmitters will be placed along the array (water depth = 150 m, $\Delta z \cong 7.89$ m) in keeping with the information displayed in Fig. 3.11 which implied roughly 18 significantly propagating modes in the problem. Figure 5.5 shows the results of using the trapezoidal integration method in the extrapolation algorithm. The matching coefficient here is approximately 0.956, which shows a decrease from the 1 m spacing case (0.996) in
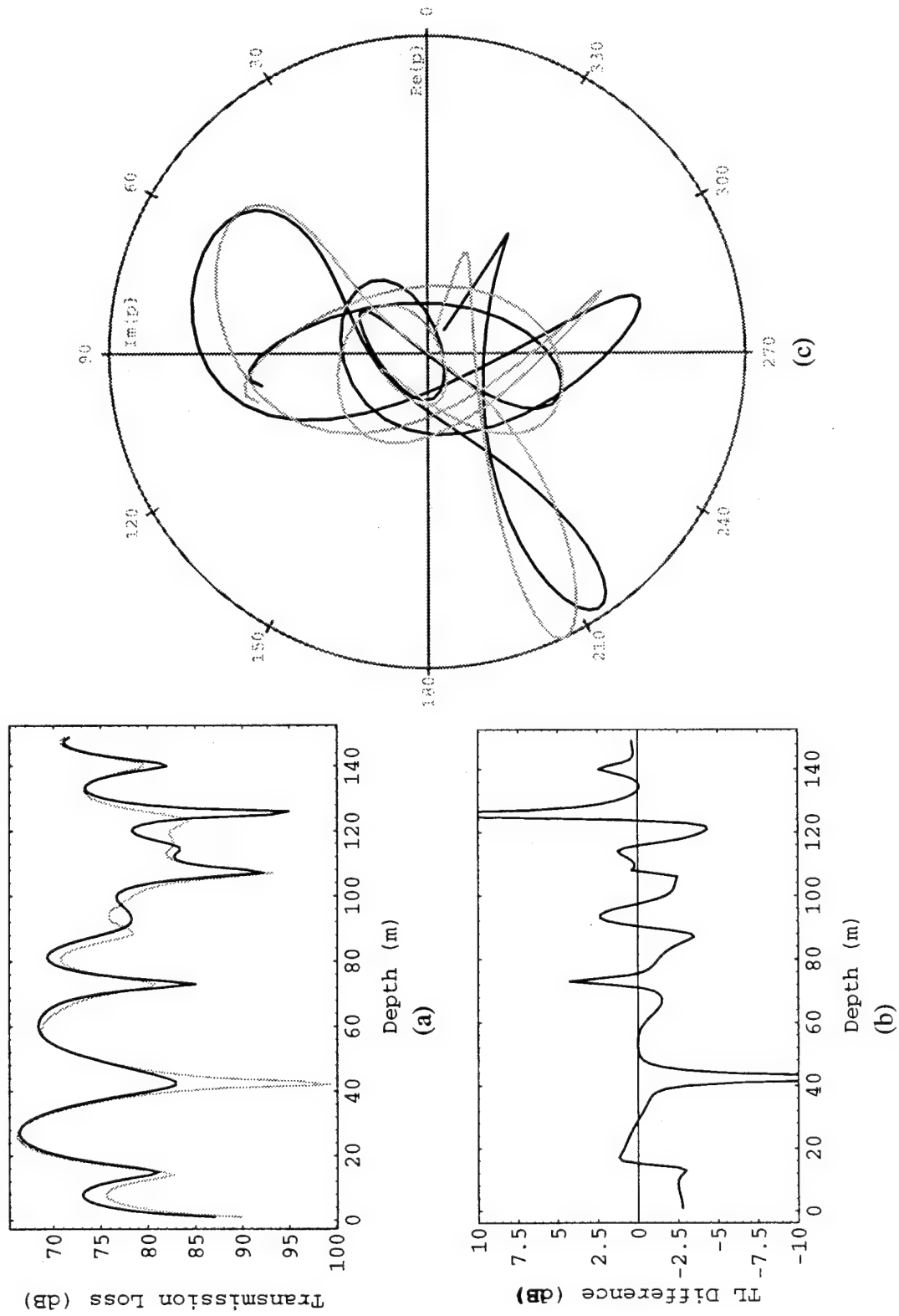
Figure 5.5. Ex. 5A: trapezoidal integration.

Figure 5.6 shows the results of using an I.P.Q.F. for this scenario. The matching coefficient here is approximately 1.0 (the actual value calculated out to six decimal places was 0.999999). As can be seen from the transmission loss comparison and the Argand diagram there is virtually no difference between the extrapolated and ground truth fields. For this I.P.Q.F. the matrix S of Eq. 5.16 is an 18x18 identity matrix due to the orthogonality of the mode functions. Since Eq. 5.12 is merely a better numerical integration method, the obliquity factors still affect the result. Figure 5.6 shows that the obliquity factors (the obliquity characterization number here is approximately 1.0) have practically no effect for this scenario. The slight decrease in matching coefficient seen in Ex. 3C can be attributed to effects due to the trapezoidal integration method employed there.

Example 5B uses the scenario of Ex. 3A, namely a rigid bottom with constant sound speed in the water column (1500 m/s). Since there are 10 propagating modes for this scenario, we will place 10 equally spaced transmitters along the reference transmit array (water depth = 50 m, $\Delta z \cong 4.55$ m). Figure 5.7 shows the results of using trapezoidal integration to do the extrapolation. The matching coefficient here is approximately 0.889. The degradation from Ex. 3A is again due to the aliasing effects due to a lower sampling "rate" that are inherent in the trapezoidal integration method.

Figure 5.8 shows the results using an I.P.Q.F. By using this method, the matching coefficient has been raised to 0.996. This is an improvement over the value of 0.982 obtained in Ex. 3A which used trapezoidal integration and transmitters spaced 1 m apart. We can now say that any degradation in the extrapolated field is due solely to the obliquity factors.

5.4. Obliquity Characterization Number vs. Matching Coefficient Revisited

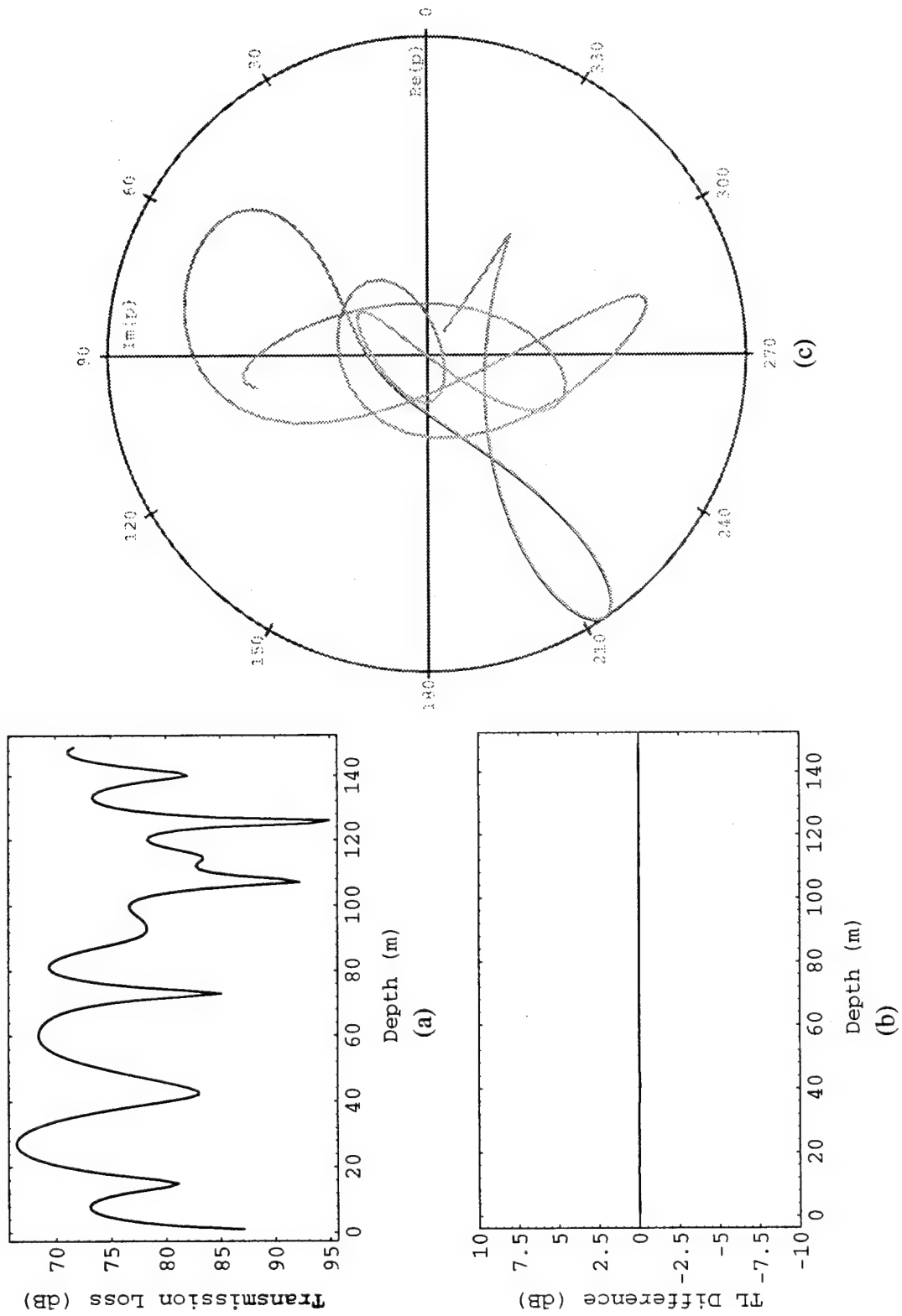In Sec. 3.4 we derived an expression called the obliquity characterization number,
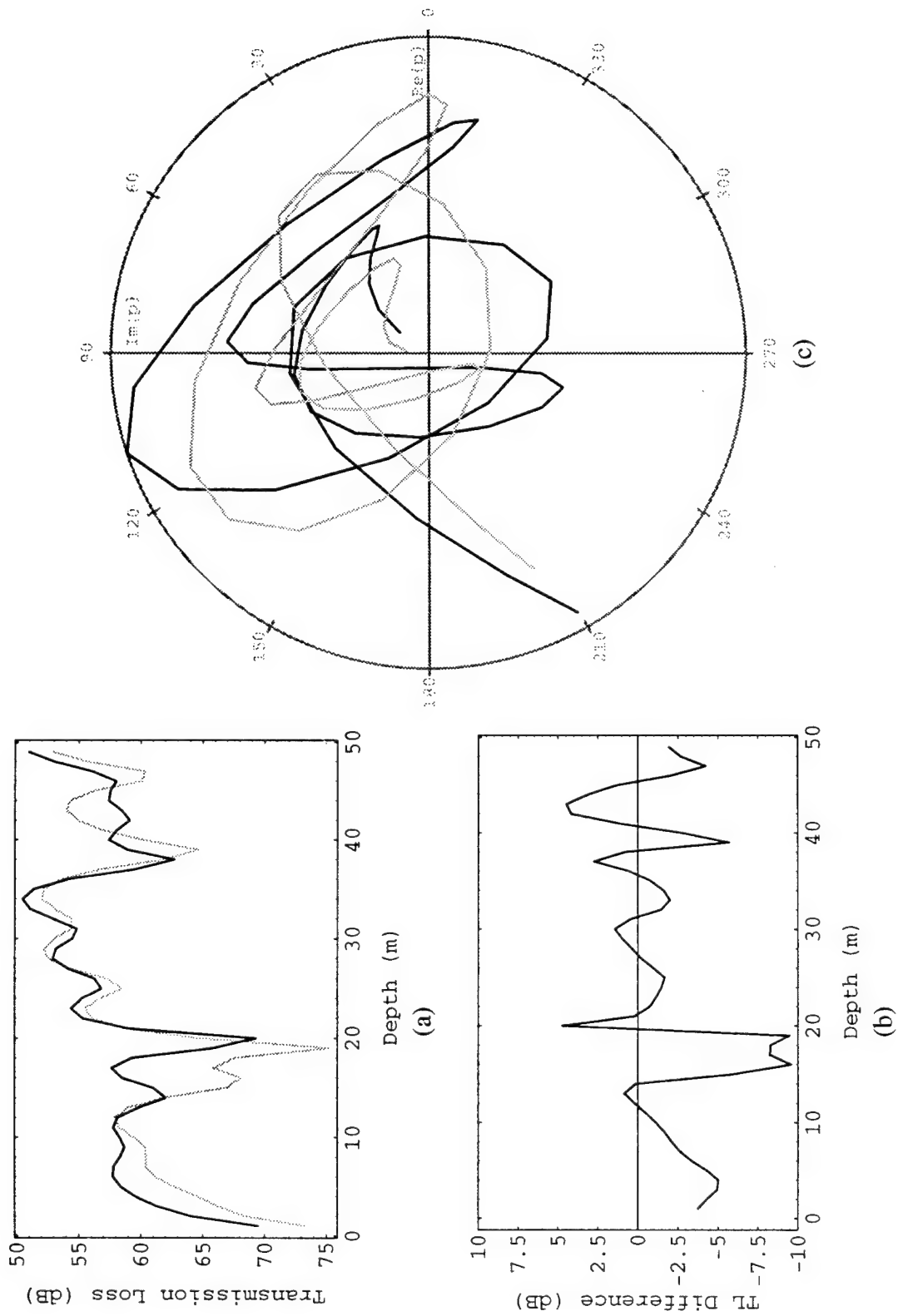
Figure 5.6. Ex. 5A: I.P.Q.F.

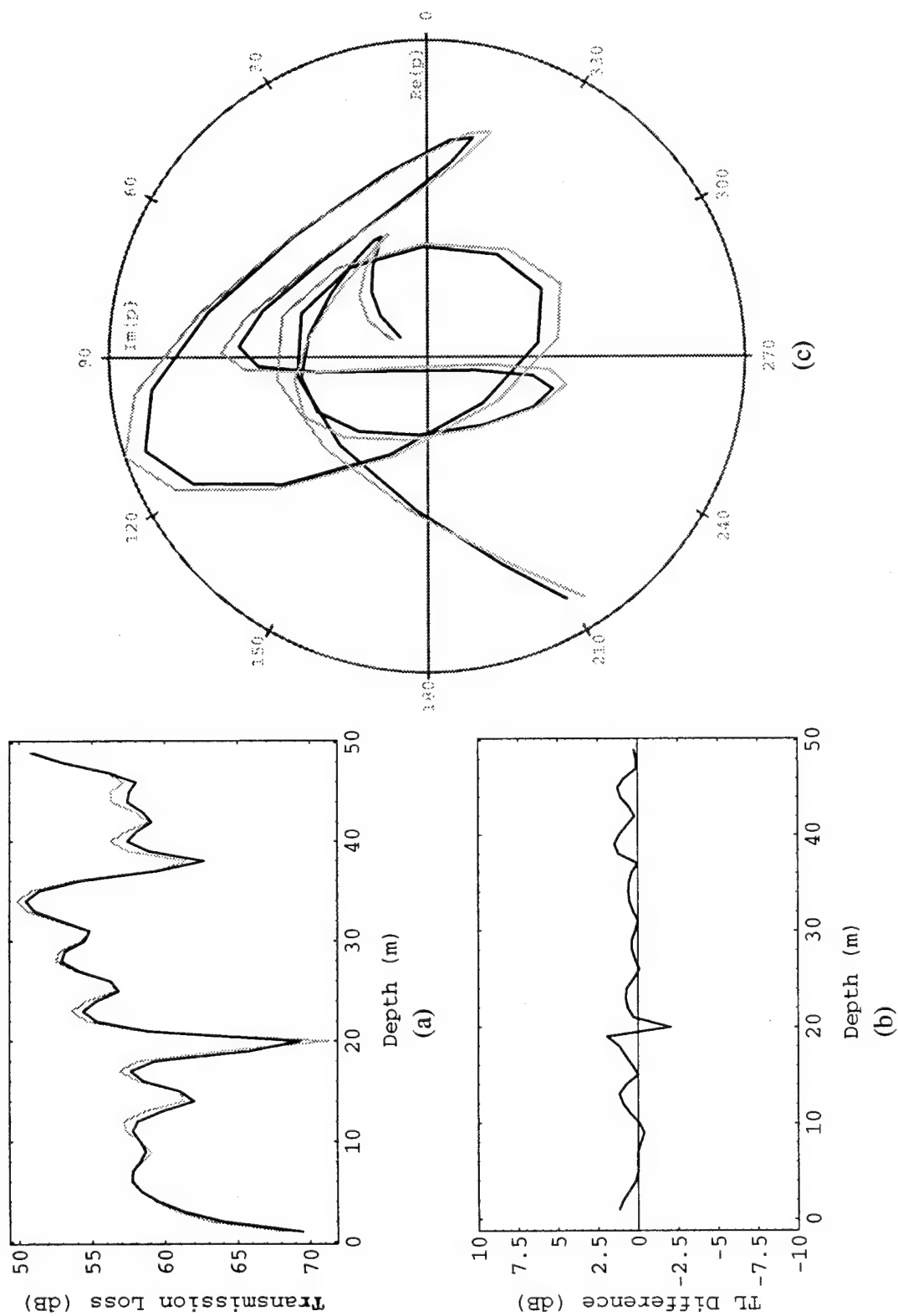*Figure 5.7. Ex. 5B: trapezoidal integration.*

Figure 5.8. Ex. 5B: I.P.Q.F.

Table 5.1. Matching Coefficients vs. Obliquity Characterization Numbers.

Example #	Obliquity Characterization Number (Υ)	Matching Coefficient ($|K|^2$)
5C (3C)	0.999	0.998
5B (3A)	0.997	0.996
5D (3D)	0.994	0.991
5E (3E)	0.983	0.974
5F (3B)	0.965	0.952

Υ_θ, which was intended as an approximation to the matching coefficient that would be seen in a given environmental scenario given approximations of the obliquity factors. We saw there that although there appeared to be a linear relationship between this value and the matching coefficient, there was an offset such that when the obliquity characterization number was 1.0 (no obliquity factor effects), the matching coefficient was somewhat less than 1.0 (~0.988). From the results of Sec. 5.3, we can now see that this was due to aliasing in the sampling of the field values along the reference array. For example, when we use an I.P.Q.F. to evaluate the integral for Ex. 3A (as in Ex. 5B), which avoids the aliasing effects, we achieve a matching coefficient of 0.996 vs. the value of 0.982 obtained by using trapezoidal integration with reference transmitters spaced at 1 m intervals.

Table 5.1 shows the results of using an I.P.Q.F. to evaluate the integrals for the same scenarios that were seen in Sec. 3.4. Figure 5.9 shows a plot of these new values with a least-squares linear fit compared to the trapezoidal integration case (the sediment example has been added for this case since the I.P.Q.F. has negated any effects due to element spacing). The equation for the least squares fit of the new data is
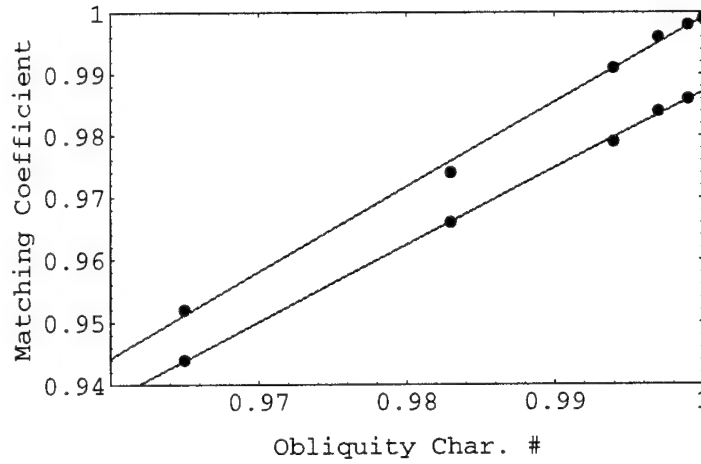
Figure 5.9. Matching Coeff. vs. Obliquity Char. Number and Linear Fit.

element spacing). The equation for the least squares fit of the new data is

$$|K|^2 \cong 1.371 \Upsilon_\theta - 0.371 . \tag{5.19}$$

We can see that the fit does extrapolate to a matching coefficient of 1.0 for an obliquity characterization number or 1.0. The slope has become slightly steeper, although this can most likely be attributed to the clustering of data points near the higher obliquity characterization numbers. In any case, the obliquity characterization does provide a useful approximation to the expected matching coefficient.

5.5. Obliquity Factor Cancellation Using an I.P.Q.F.

Our use of the modal decomposition in evaluating the integral also allows us to perfectly cancel the obliquity factor effects. In Eq. 2.8 we saw how calculating the integral produced an extra $\xi_m^{-1/2}$ in the modal summation and an incorrect multiplier in front of the summation. An attempt to cancel both these effects was made by multiplying the summation by the mode-independent factor $N_a{}'$ (see Eq. 2.10). The reference wavenumber multiplier combined with the extra $\xi_m^{-1/2}$ to produce the modal-dependent obliquity factors. If we modify our I.P.Q.F. by making

$$
S = \begin{bmatrix} \xi_1^{-1/2} & 0 & 0 & 0 \\ 0 & \xi_2^{-1/2} & 0 & 0 \\ 0 & 0 & \ldots & 0 \\ 0 & 0 & 0 & \xi_M^{-1/2} \end{bmatrix}, \tag{5.20}
$$

i.e., correct for the extra $\xi_m^{-1/2}$ factors that occur in the integration by placing them along the diagonal of the S matrix, and subsequently modify the mode-independent multiplier so that

$$
N_a' = \left[\frac{8\pi}{i} \frac{r_a(r_b - r_a)}{r_b} \right]^{1/2}, \tag{5.21}
$$

the effects of the obliquity factors should be cancelled exactly. Note that only the primary extrapolation now need be done since the alternate extrapolation formula was developed in order to lessen the effects of the obliquity factors. Figure 5.10 shows the results of calculating the extrapolation integral using a "deobliquified" I.P.Q.F. As expected, the matching coefficient here is 1.0.

5.6. Comments on Modal Decomposition Methods

Section 5.5 showed how modal decomposition methods can be used to do field extrapolation (see also [Rouseff *et al.*]). There are several interesting questions about these methods that invite future work. One area has to do with how elements are spaced on the array. Although the sampling criterion for the modal decomposition-based methods only deals with the actual number of transmitters/receivers that must populate an array, does this mean that all the elements could be tightly grouped in one small vertical segment of the array? Preliminary numerical studies have shown that this is not the case due to numerical instabilities in calculating the A matrix. This is a subject that deserves detailed
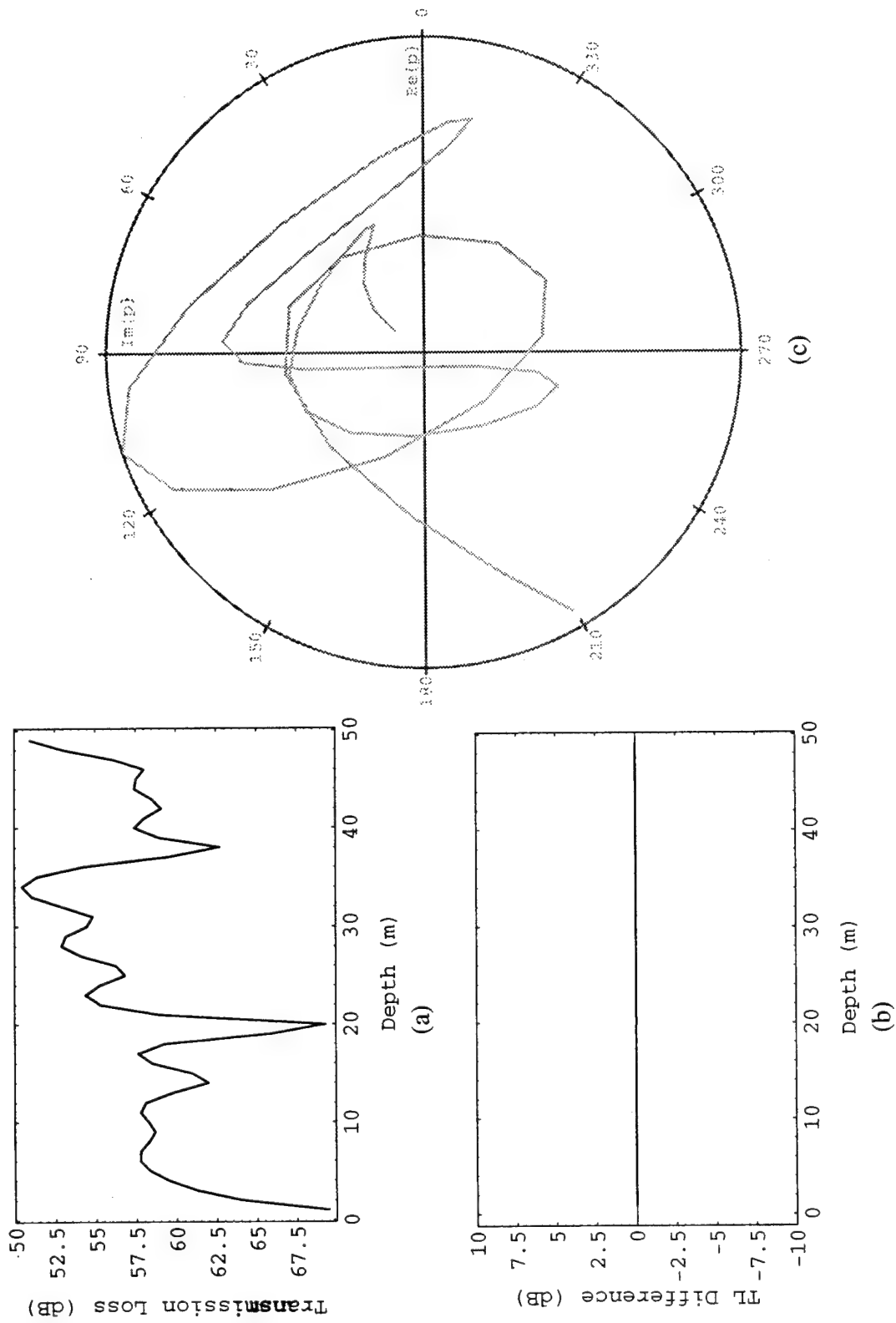
Figure 5.10. Ex. 5B: I.P.Q.F. (deobliquified version).

study.

Another area of future work focuses on modeled field mismatch issues. Much of the work in Ch. 4 can translate directly to the results of Ch. 5. One extra consideration, however, is that while the mode functions that are used as an integration basis are exact for the modeled field, they will not be exact for the Green's function data. As seen in Ch. 4, for environmental scenarios in which high order modes are stripped off, the perturbations in the mode functions tend to be small, so this mode basis mismatch should not contribute much to the errors. Preliminary numerical studies have borne this out. This also is a topic that deserves further study.

5.7. Summary of Chapter 5

Chapter 5 dealt with numerical integration issues pertinent to the acoustic field extrapolation algorithm due to the necessity of having discretely placed transmitters/ receivers along the reference arrays. It was shown how simple summation-type (specifically, trapezoidal) numerical integration techniques can degrade the results for insufficiently dense sampling along the reference arrays. A method was suggested for determining a priori the required spacing for elements on the reference arrays. It was then shown how inner product quadrature formulas can be used, assuming a normal mode expansion of the modeled field and Green's function data, to alleviate this problem. The sampling requirement there was that the reference arrays contain at least as many elements as the number of propagating modes. It was shown how using the mode functions as the integration basis essentially ties together the Huygens' principle-based and modal decomposition-based extrapolation algorithms.

Chapter 6: Conclusion

6.1. Summary of Dissertation

This dissertation has concentrated on analyzing algorithms for extrapolating underwater acoustic fields. These types of algorithms may be necessary for cases where it is desired to predict acoustic fields at some distance from an acoustic source, but the environmental conditions over the entire range that are needed as input to a modeling algorithm are unavailable, or measured data at all locations are also unavailable [Cox *et al.*]. The extrapolation algorithms combine modeled and measured data in order to predict the fields.

Chapter 1 gave some background material in the form of an introduction to normal mode theory and a source localization algorithm (HAP) that utilized medium calibration much as the extrapolation algorithm. Chapter 2 outlined Huygens' principle and the Fresnel-Kirchhoff diffraction formula which then served as models for the underwater field extrapolation algorithm. It was found that by combining modeled fields along a reference array with calibration data taken along the array, useful extrapolation results could be obtained. The combination of the information was essentially an integral over depth of their product. By analyzing the extrapolated and ground truth fields using normal mode theory, it was seen that the extrapolated field contained a modal-dependent "obliquity" factor which became more prominent for more steeply propagating modes. It was shown how an alternate extrapolation formula based on the range derivative of the modeled field could help average out the obliquity factors to first order. It was also analytically shown how calibration data take into effect range dependencies in the medium to produce reliable extrapolated fields.

Chapter 3 contained numerically modeled illustrations of the mathematical relationships shown in Ch. 2. Obliquity factor effects were examined for cases of

moderately steeply, very steeply, and mostly horizontally propagating energy. These examples showed how more steeply propagating energy tended to degrade the extrapolated field estimates through a quantitative goodness measure, the matching coefficient. It was also shown how an estimate of the degradation in matching coefficient could be obtained through estimates of the obliquity factors alone.

Chapter 4 dealt with modeled field mismatch issues, i.e., cases where the assumed environmental parameters used as input to the modeling step in the algorithm did not correctly reflect the actual parameters. Perturbational results were shown relating errors in the sound speed profile of the water column to errors in the horizontal wavenumbers and mode functions. It was shown how these errors translated into errors in the extrapolated fields. Perturbational results were also examined for sediment property errors (sound speed, attenuation, and density). As in the obliquity factor effects, it was shown how estimates of the eigenvalue perturbations alone can lead to an estimate of the degradation in matching coefficient.

Chapter 5 concentrated on the issue of numerically estimating the integral in the extrapolation algorithm. This was necessary due to the fact that elements must be placed at discrete locations along the reference arrays. It was shown how undersampling the modeled field/calibration data product can degrade the extrapolated fields when simple summation-type (trapezoidal) quadrature methods are used, and how to estimate the spacing required for reliable extrapolations. It was shown how inner product quadrature formulas could be used to essentially perform a modal decomposition-based extrapolation formula by using the mode functions of the modeled field as the integration basis. The sampling requirement was that there be at least as many elements on the reference array as there were propagating modes. It was then shown how the I.P.Q.F. could be modified to cancel the obliquity factors exactly.

6.2. Suggestions for Future Work

There are several areas for further research in the topic of field extrapolation algorithms. One has to do with the effects of surface and bottom roughness on the algorithm. Bottom roughness can be difficult to model, but its effects over the calibration distance should be taken into account by the Green's function data, leaving only the effects due to bottom roughness over the extrapolation range. Surface roughness, unlike the majority of bottom roughness scenarios, is time-variable. Therefore, an area of study exists as far as determining how calibration data are affected by the changing sea surface, as well as the effects of coupling between surface and bottom roughness. Along with this time-variable theme is the issue of internal waves, and how they affect the calibration data.

Another area of study has to do with the out-of-plane problem. All the material in this dissertation assumed that the reference arrays, the hypothetical source, and/or the hypothetical receiver were in a common vertical plane. The case where they are not coplanar deserves some attention. The problem wherein the reference arrays are not perfectly vertical provides another topic of continued study.

The case of wideband signals is also an area for further research. This dissertation considered only narrowband cw signals. There may be some advantage or disadvantage to using wideband signals for calibration of the medium.

Finally, there are the issues mentioned in Sec. 5.6 having to do specifically with modal decomposition-based methods, namely the element grouping problem and the integration basis problem for mismatch scenarios.

Bibliography

Al-Kurd, A. A., "Holographic array processing in the ocean," Ph.D. dissertation, University of Washington, Seattle, WA, 1993. Also: same author and title, APL-UW TR 9306, Applied Physics Laboratory, University of Washington, Seattle, 1993.

Baggeroer, A. B., W. A. Kuperman, and P. N. Mikhalevsky, "An overview of matched field methods in ocean acoustics," *IEEE J. Oceanic Eng.*, vol. 18, no. 4, pp. 401-424, 1993.

Boyles, C. A., *Acoustic Waveguides - Applications to Oceanic Science*, New York: John Wiley & Sons, 1984.

Brekhovskikh, L. M. and Y. P. Lysanov, *Fundamentals of Ocean Acoustics*. New York: Springer-Verlag, 1991.

Collins, M. D., "FEPE User's Guide," NORDA Technical Note 365, Naval Research Laboratory, Stennis Space Center, Mississippi, October, 1988. (For the FEPE source code, the author may be contacted by e-mail: COLLINS@v5160.nrl.navy.mil)

Collins, M. D. and E. K. Westwood, "A higher order energy conserving parabolic equation for range dependent ocean depth, sound speed, and density," *J. Acoust. Soc. Am.*, vol. 89, no. 3, pp. 1068-1075, 1991.

Cox, H., H. Lai and M. Hirano, "Reciprocity based channel compensation for wideband communications in a multipath environment," in *Conference Record of the Twenty-Seventh Asilomar Conference on Signals, Systems, and Computers* (Pacific Grove, CA), Nov. 1993, pp. 593-597.

Davis, P. J. and P. Rabinowitz, *Methods of Numerical Integration*. Orlando: Academic Press, Inc., 1984.

Dosso, S. E. and N. R. Chapman, "Measurement and modeling of downslope acoustic propagation loss over a continental slope," *J. Acoust. Soc. Am.*, vol. 81, no. 2, pp. 258-268, 1987.

Dosso, S.E., M. L. Yeremy, J. M. Ozard and N. R. Chapman, "Estimation of ocean-bottom properties by matched-field inversion of acoustic field data," *IEEE J. Oceanic Eng.*, vol. 18, no. 3, pp. 232-239, 1993.

Dowling, D.R., "Acoustic pulse compression using passive phase-conjugate processing," *J. Acoust. Soc. Am.*, vol. 95, no. 3, pp. 1450-8, 1994.

Evans, R. B., "Coupled mode solution for acoustic propagation in a waveguide with stepwise depth variations of a penetrable bottom," *J. Acoust. Soc. Am.*, vol. 74, no. 1, pp. 188-195, 1983.

Fox, W. L. J., D. Rouseff and R. P. Porter, "Underwater acoustic field extrapolation using vertical reference arrays," in *Conference Record of the Twenty-Seventh Asilomar Conference on Signals, Systems, and Computers* (Pacific Grove, CA), Nov. 1993, pp. 154-158.

Gingras, D.F., "Impact of uncertain environmental knowledge on the shallow-water transfer function," SACLANTCEN SM-263, SACLANT Undersea Research Centre, La Spezia, Italy, 1992.

Goncharov, V. V. and A. G. Voronovich, "An experiment on matched-field acoustic tomography with continuous wave signals in the Norway Sea," *J. Acoust. Soc. Am.*, vol. 93, no. 4, pp. 1873-1881, 1993.

Goodman, J. W., *Introduction to Fourier Optics.* San Francisco: McGraw Hill, 1968.

Gribble, J. D., "Interpolatory inner product quadrature formulas," *BIT*, vol. 20, pp. 466-474, 1980.

Halliday, D. and R. Resnick, *Physics.* New York: Wiley, 1978.

Hamilton, E. L., "Geoacoustic modeling of the sea floor," *J. Acoust. Soc. Am.*, vol. 68, no. 5, pp. 1313-1340, 1980.

Hamson, R. M. and R. M. Heitmeyer, "Environmental and system effects on source localization in shallow water by the matched-field processing of a vertical array," *J. Acoust. Soc. Am.*, vol. 86, no. 5, pp. 1950-1959, 1989.

Jensen, F. B., W. A. Kuperman, M. B. Porter, and H. Schmidt, *Computational Ocean Acoustics.* New York: American Institute of Physics, 1994.

Kinsler, L. E., A. R. Frey, A. B. Coppens, and J. V. Sanders, *Fundamentals of Acoustics.* New York: John Wiley and Sons, 1982, 3rd ed.

Lawson, C. L. and R. J. Hanson, *Solving Least Squares Problems.* Englewood Cliffs, NJ: Prentice-Hall, 1974.

Lindsay, C. E. and N. R. Chapman, "Matched field inversion for geoacoustic model parameters using adaptive simulated annealing," *IEEE J. Oceanic Eng.*, vol. 18, no. 3, pp. 224-231, 1993.

Marks, R. J. II, *Introduction to Shannon Sampling and Interpolation Theory.* New York: Springer-Verlag, 1991.

McGrath, J. F., "Gaussian product-type quadratures," *Appl. Math. and Comp.*, vol. 5, pp. 265-280, 1979.

Mourad, P. D., D. Rouseff, R. P. Porter, and A. Al-Kurd, "Source localization using a reference wave to correct for oceanic variability," *J. Acoust. Soc. Am.*, vol. 92, no. 2, pp. 1031-1039, 1992.

Naylor, A. W. and G. R. Sell, *Linear Operator Theory in Engineering and Science.* New York: Springer-Verlag, 1982.

Oppenheim, A. V. and R. W. Schafer, *Discrete-Time Signal Processing.* Englewood Cliffs, New Jersey: Prentice Hall, 1989.

Oppenheim, A. V., A. S. Willsky and I. T. Young, *Signals and Systems.* Englewood Cliffs, New Jersey: Prentice Hall, 1983.

Papoulis, A., *Probability, Random Variables, and Stochastic Processes.* New York: McGraw-Hill, 1984.

Porter, M. B., "The KRAKEN Normal Mode Program," Unpublished technical report, SACLANT Undersea Research Centre, 11 Nov. 1992. (The source code for KRAKEN is available via anonymous FTP from alba.njit.edu)

Porter, R. P., "Three-Dimensional Imaging Methods in Acoustics and Electromagnetics," Unpublished lecture notes for EE 578, Dept. of Electrical Engineering, University of Washington, Seattle, 1994.

Porter, M. B. and E. L. Reiss, "A numerical method for ocean acoustic normal modes," *J. Acoust. Soc. Am.*, vol. 76, no. 1, pp. 244-252, 1984.

Porter, R. P., P. D. Mourad and A. Al-Kurd, "Wave-front reconstruction in variable, multimode waveguides," *J. Opt. Soc. Am. A*, vol. 9, no. 9, pp. 1984-1990, 1992.

Porter, R. P., D. Rouseff, W. L. J. Fox and M. Siderius, "Acoustic calibration in shallow water: Theory, simulations, and a preliminary site study," APL-UW TM 31-93, Applied Physics Laboratory, University of Washington, Seattle, 1993.

Press, W. H., B. P. Flannery, S. A. Teukolsky, and W. T. Vetterling, *Numerical Recipes in C.* New York: Cambridge University Press, 1988.

Rajan, S. D., J. F. Lynch and G. V. Frisk, "Perturbative inversion methods for obtaining bottom geoacoustic parameters in shallow water," *J. Acoust. Soc. Am.*, vol. 82, no. 3, pp. 998-1017, 1987.

Rouseff, D., "Ocean acoustic holography: Using a reference source to remove oceanic variability," Unpublished technical report, Applied Physics Laboratory, University of Washington, Seattle, 1989.

Rouseff, D., (Untitled), Unpublished technical note, Applied Physics Laboratory, University of Washington, Seattle, February 8, 1993.

Rouseff, D., (Untitled), Unpublished technical note, Applied Physics Laboratory, University of Washington, Seattle, April 29, 1993.

Rouseff, D., M. Siderius, W. L. J. Fox and R. P. Porter, "Acoustic calibration in shallow water using sparse data," submitted and accepted for publication in *J. Acoust. Soc. Am.*, August, 1994.

Schiff, L. I., *Quantum Mechanics*. New York: McGraw-Hill, 1968.

Uscinski, B. J., *The Elements of Wave Propagation in Random Media*. New York: McGraw-Hill, 1977.

Wen, T., W. J. Felton, J. C. Luby, W. L. J. Fox and K. L. Kientz, "Environmental Measurements in the Beaufort Sea, Spring 1988," APL-UW TR 8822, Applied Physics Laboratory, University of Washington, Seattle, WA, March 1989.

Yang, T. C., "A method of range and depth estimation by modal decomposition," *J. Acoust. Soc. Am.*, vol. 82, no. 5, pp. 1736-1745, 1987.

Yang, T. C., "Effectiveness of mode filtering: a comparison of matched-field and matched-mode processing," *J. Acoust. Soc. Am.*, vol. 87, no. 5, pp. 2072-2084, 1990.

Yariv, A., *An Introduction to Theory and Applications of Quantum Mechanics*. New York: John Wiley and Sons, Inc., 1982.

Vita

Warren Leonard John Fox was born March 30, 1966, in Seattle, Washington. He grew up in Everett, Washington, with his father John, mother Karen, brother Colin, and sisters Sarah and Anne. He graduated from Cascade High School in Everett, Washington, in June of 1984. He was co-valedictorian of his graduating class, a National Merit Scholar, and the 1984 Northwest District high jump champion. In June of 1988 he graduated cum laude with his Bachelor of Science in Electrical Engineering degree from the University of Washington in Seattle, Washington. Upon graduation, he joined the professional staff of the Applied Physics Laboratory, University of Washington, as an electrical engineer. In September of 1989 he was granted an APL-UW Fellowship to support his graduate work. He earned his Master of Science in Electrical Engineering from the UW in December of 1990, where his thesis topic was the use of a new time-frequency representation for range-Doppler applications. He continued on the APL-UW Fellowship during his Ph.D. studies. His research interests include: signal processing, detection/classification/localization applications, and ocean acoustic applications. He is a member of the Signal Processing and Oceanic Engineering Societies of the Institute of Electrical and Electronic Engineers (I.E.E.E.).

Selected Publications:

Fox, W. L. J., "Application of a Cone-Shaped Kernel Time-Frequency Representation to Sonar and Radar Range-Doppler Processing," Master's thesis, University of Washington, Seattle, WA, Dec. 1990.

Fox, W. L. J., D. Rouseff and R. P. Porter, "Underwater acoustic field extrapolation using vertical reference arrays," in *Conference Record of the Twenty-Seventh Asilomar Conference on Signals, Systems, and Computers* (Pacific Grove, CA), Nov. 1993, pp. 154-158.

REPORT DOCUMENTATION PAGE

Public reporting burden for this collection of information is estimated to average 1 hour per response, including the time for reviewing instructions, searching existing data sources, gathering and maintaining the data needed, and reviewing the collection of information. Send comments regarding this burden estimate or any other aspect of this collection of information, including suggestions for reducing this burden, to Washington Headquarters Services, Directorate for Information Operations and Reports, 1215 Jefferson Davis Highway, Suite 1204, Arlington, VA 22202-4302, and to the Office of Information and Regulatory Affairs, Office of Management and Budget, Washington, DC 20503.

1. AGENCY USE ONLY *(Leave blank)*	2. REPORT DATE March 1995	3. REPORT TYPE AND DATES COVERED Technical

4. TITLE AND SUBTITLE

Underwater Acoustic Field Extrapolation: Theory and Sensitivity Analysis

5. FUNDING NUMBERS

6. AUTHOR(S)

Warren L. J. Fox

7. PERFORMING ORGANIZATION NAME(S) AND ADDRESS(ES)

Applied Physics Laboratory
University of Washington
1013 NE 40th Street
Seattle, WA 98105-6698

8. PERFORMING ORGANIZATION REPORT NUMBER

APL-UW TR 9501

9. SPONSORING / MONITORING AGENCY NAME(S) AND ADDRESS(ES)

APL-UW Independent Research &
    Development Program
1013 NE 40th Street
Seattle, WA 98105-6698

10. SPONSORING / MONITORING AGENCY REPORT NUMBER

11. SUPPLEMENTARY NOTES

12a. DISTRIBUTION / AVAILABILITY STATEMENT

Distribution Unlimited

12b. DISTRIBUTION CODE

13. ABSTRACT *(Maximum 200 words)*

In some underwater acoustic applications, it is desirable to predict what an acoustic field will be at some distance away from a source. Numerical modeling based on environmental parameters (e.g., sound speed, bathymetry, sediment properties) is one possibility, but the amount of environmental information necessary for accurate long-range modeling is often beyond what is realistically measurable. Actual acoustic measurements are another possibility, but our knowledge of the fields is then limited to the points in the ocean where the sources and receivers are located. We present a hybrid method for predicting acoustic fields that takes limited acoustic measurements and extrapolates them over short ranges using modeled fields. The measured and modeled fields are combined in an integral formulation via a specialization of Huygens' principle. The basic theoretical formulation is stated and analyzed using the theory of normal modes. The formulation leads directly to modal-dependent (grazing angle dependent) "obliquity" factors, which are canceled to first order by averaging with a range derivative-based extrapolation. Sensitivity of the algorithm to the higher order components of the obliquity factors is studied. As with other model-based algorithms, environmental mismatch can degrade the results. The algorithm's sensitivity to mismatch in water column sound speed and sediment sound speed, attenuation, and density are studied via a perturbational approach. Since the algorithm explicitly contains an integral and the measured field is collected at discrete locations, numerical quadrature techniques are studied. It is shown how undersampling can degrade the quality of the extrapolated fields, and how the spatial sampling required for reliable extrapolation can be obtained. A modal decomposition-based integration method is then shown, where the number of reference elements required is equal to the number of modes that contribute significantly to the fields. A modified version of this formulation can exactly cancel the obliquity factors.

14. SUBJECT TERMS

Underwater Acoustics, Acoustic Modeling, Normal Mode Theory, Huygens' Principle, Obliquity Factors, Environmental Mismatch, Perturbation Theory, Inner Product Quadrature Formulas

15. NUMBER OF PAGES

149

16. PRICE CODE

17. SECURITY CLASSIFICATION OF REPORT Unclassified	18. SECURITY CLASSIFICATION OF THIS PAGE Unclassified	19. SECURITY CLASSIFICATION OF ABSTRACT Unclassified	20. LIMITATION OF ABSTRACT SAR